2014

Development of an algorithm of bidirectional surface strain measurements from soft elastomeric capacitors

Jingzhe Wu
Iowa State University

Development of an algorithm of bidirectional surface strain measurements from soft elastomeric capacitors

by

Jingzhe Wu

A thesis submitted to the graduate faculty

in partial fulfillment of the requirements for the degree of

MASTER OF SCIENCE

Major: Civil Engineering (Structural Engineering)

Program of Study Committee:
Simon Laflamme, Major Professor
Jiehua 'Jay' Shen
Halil Ceylan

Iowa State University

Ames, Iowa

2014

TABLE OF CONTENTS

LIST OF FIGURES

LIST OF TABLES

ACKNOWLEDGEMENTS

I would like to send my sincere thank to my major professor, Dr. Simon Laflamme, for his excellent guidance and thoughtful support throughout my research process as well as for my career development. He always encouraged me with his positive attitude and cool personality during tough times in the present research and gave me valuable support and advice for my professional life. I would also like to thank my committee members, Dr. Jiehua 'Jay' Shen and Dr. Halil Ceylan, for their guidance throughout my research and being part of my advisory committee.

In addition, I would like to thank my husband, for his advice, support, understanding, respect and love, especially during my hard times in both research and life. I am grateful to my family for supporting all the decisions I have made and always being there for me unconditionally. I would also like to offer my appreciation to my colleagues, Chunhui Song and Daniel Safier, for their efforts in this project and building such an enjoyable working environment. Much appreciation to Hussam Saleem and Liang Cao, for helping me with my questions; and Sari Kharroub, for helping me modify this thesis into a better shape. I would like to extend my thanks to my dear friends, Qiaochu Zhu and Miao Yu for being there with me through ups and downs. Finally, thanks to all my friends for their encouragement and companionship.

ABSTRACT

Once a structure comes into service, the most important concern is its ability to keep providing steady and safe service. Assessment of structural health is a tool that can be used to ensure such. However, most of the available evaluation strategies in structural health monitoring are labor intensive such as visual inspection, which is highly economically inefficient, especially for large scale structures. As a result, structural health monitoring (SHM) and smart sensor techniques are of great interest that have brought the attention of scientists recently.

As an economic surface sensor for large scale structural surface, a soft elastomeric capacitor (SEC) was proposed in previous studies. However, the previous application of the SEC network was only able to monitor uniaxial strain filed due to the implicit directional strain measurement. To extend the applicability of the SEC sensor network into real-time biaxial strain field monitoring, an algorithm has been developed in this thesis based on a strain mapping approach using least square estimator. With the algorithm formulation based upon the classical plate theory, the biaxial sensing ability of the SEC sensor network with the proposed algorithm has been verified on both a rectangular cantilever plate under three types of load cases and an irregular laminated cantilever plate under simulated wind pressure. The proposed algorithm showed a computing speed around 0.1 s in a specific application which enables real-time monitoring and illustrated stability under noise level up to 5%. It can be concluded that the proposed algorithm possess the potential to be applied for wind turbine monitoring.

CHAPTER 1
INTRODUCTION

1.1 Background

The deterioration status of structures in service has been always one of the most important information for stability, serviceability and safety concern for civil, mechanical and aerospace systems. Particularly for large-scale civil infrastructures, traditional labor-intensive actions, such as visual inspection, are economically inefficient and ineffective when the damage is subtle. Also, they can only obtain structural degradation condition at a low frequency. Therefore, the attention on studying and applying structural health monitoring (SHM) techniques for damage detection becomes important [1].

A fundamental challenge in SHM is to capture local damage in spite of the wide range of geometries and time scales [2]. In the past three decades, most SHM systems focused on identifying the existence of structural defects on a more global scale through structural dynamic characteristics, while localizing damages and assessing the severity through non-destructive evaluation (NDE) [1, 2]. However, NDE methods are generally uneconomical and, therefore, can only be applied locally and temporarily. Although some other SHM techniques have achieved adequate precision in localizing damage based on static monitoring systems, their application on large-scale surfaces is still costly due to the increase in the number of sensors [3].

1.2 Sensing Technology in Static SHM system

Static-based sensing methods have a wide range of applications in SHM systems for damage detection and localization. Various types of sensor have been developed and applied.

They are generally embedded into the monitored object or installed onto the surface. Those sensors are discussed following as embedded sensors, surface-bonded sensors and soft elastomeric capacitors.

1.2.1 Embedded sensors

As one of the most popular embedded sensors, fiber optic sensor (FOS) possesses more advantages including flexibility, suitability for embedment and immunity to electromagnetic interference [4] than traditional sensors, such as resistive strain gauges. Piezoelectric polymers are also commonly used for embedded sensors including piezoceramic (PZT) and polyvinylidene fluoride (PVDF) which are beneficial for their electromechanical coupling mechanism [5], as well as for their low cost material and simple fabrication [6]. Unfortunately, the embedment of these sensors is an inevitable expensive process and that is accompanied with a decrease in constructability and difficulties in the repair and replacement of the sensor after installation. In addition, problems would occur on the functional aspect. On one hand, the embedment brings a big challenge for the mechanical and chemical durability of the sensor itself. For instance, Habel et al. looked into the chemical threats to three polymer coatings for FOSs in the high-alkaline environment in concrete and found that the softening of the coating still occurred after 15 days of embedment in concrete despite the fact that the fluorine-thermoplastic showed better durability than acrylate and polyimide [7, 8]. On the other hand, the embedment introduces discontinuity in the geometry and material properties of the monitored element which could possibly lead to a loss in the capacity of the structure.

1.2.2 Surface-bonded sensors

Sensors mounted onto the surface of the structure may avoid possible material defects caused by embedment. Both FOSs and PZT sensors can also be bonded on structural surface. However, bonding reliability tends to be a common challenge for surface-mounted sensors. Li et al. stated the strain transmission loss from substrate through bonding layer to the fiber bragg grating (FBG) becomes considerable when the substrate is thin or its material has low modulus [9]. They have also proposed a correction formula for this phenomenon. Similarly, Lin et al. pointed out the weakness of the bonding layer in durability and acoustic impedance matching of piezoelectric wafer active sensors (PWAS) which potentially can lead to a loss in accuracy of damage detection [10]. They solved the problem by developing an in-situ fabrication method to remove the need for a bonding layer.

Sensors installed on structural surface can only provide localized information at the monitored point. To capture enough information for damage detection and localization of large structural surface, the amount of sensors needed could rapidly grow and be followed by economic concerns. Low-cost piezoelectric polymers material has also been widely used for surface bonded sensing devices.

1.2.3 Soft elastomeric capacitors

To reduce the cost and improve the applicability of a sensing system on large-scale structures, the attempt could be to either increase the efficiency of the sensor network or lower the price and to improve the applicability of the applied sensors. As a promising solution, a soft capacitive sensor (Fig. 1.1) made from soft-stretchable dielectric polymer and based on the direct capacitance-strain relationship has been proposed as a strain gauge with advantages including economic efficiency, easiness for installation on various surface

conditions, customizable shape to fit any surface, simplicity in data processing and high durability [3, 11, 12]. This capacitance-based sensor, termed soft elastomeric capacitor or sensing patch, was assembled in a matrix form to build a bio-inspired sensing system termed sensing skin [12]. The SEC demonstrated its capability to detect and localize cracks on both large-scale concrete and steel beams [12].

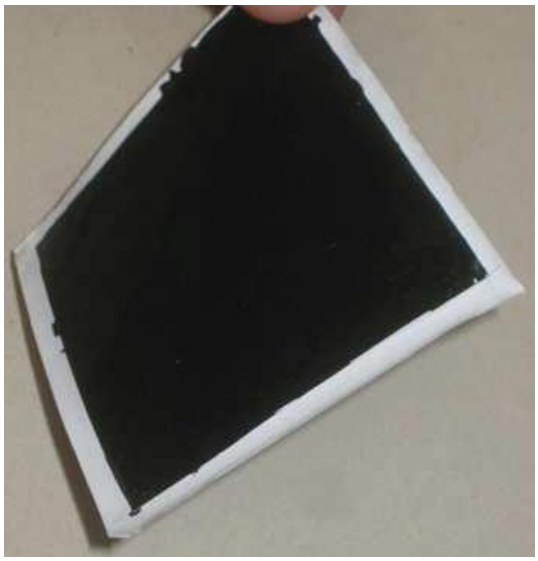

Figure 1.1: Soft Elastomeric Capacitor [12]

Although the SEC and sensing skin exhibited promising damage detection and localization abilities, unlike other strain sensor such as FBG and traditional resistance train gauge, it measures the strain with implicit information on its direction due to its sensing mechanism. A schematic representation is presented in Fig. 1.2. The sensing principle of SEC can be expressed by Eq. 1.1 (where C is the capacitance value, $A = w \cdot l$ is the sensor area, $h$is the thickness of the dielectric of SEC, $e_0 = 8.854\ pF/m$ is the vacuum permittivity and e_r is the polymer relative permittivity) [3, 11, 12]:

$$\mathrm{C} = e_0 e_r \frac{A}{h} \tag{1.1}$$

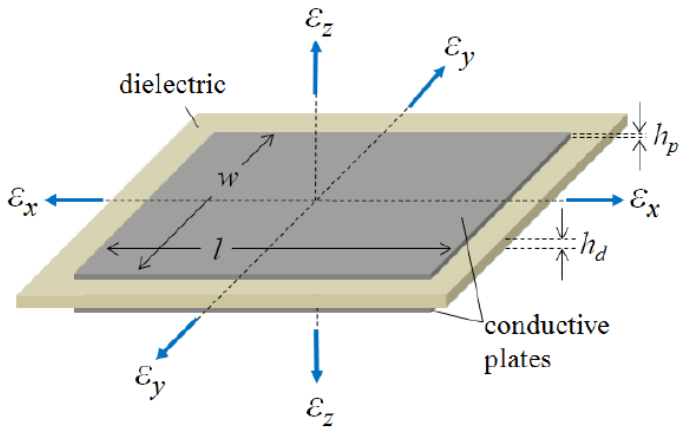

Figure 1.2: Schematic representation of the SEC [13]

By representing the small change of capacitance in a differential form with respect to the SEC geometry, the following equation can be obtained:

$$\Delta C = \left(\frac{\Delta l}{l} + \frac{\Delta w}{w} + \frac{\Delta h}{h}\right) C \tag{1.2}$$

Further, Eq. 1.2 can be rewritten with three directional strains (ε_x, ε_y and ε_z) involved:

$$\frac{\Delta C}{C} = \varepsilon_x + \varepsilon_y - \varepsilon_z \tag{1.3}$$

Based on the Hook's Law and the assumption that the SEC subjected to no external force in the vertical z direction, the equation of plane stress is (where ν is the Poisson's ratio of the polymer):

$$\varepsilon_z = -\frac{\nu}{1-\nu}(\varepsilon_x + \varepsilon_y) \tag{1.4}$$

Therefore, by substituting Eq. 1.4 into Eq. 1.3, the following equation can be gained:

$$\frac{\Delta C}{C} = \lambda(\varepsilon_x + \varepsilon_y) \tag{1.5}$$

Where λ denoted as the gauge factor ($\lambda \approx 2$ for the current SEC [13]):

$$\lambda = \frac{1}{1-\nu} \tag{1.6}$$

When measuring the change in the capacitance corresponding to the local deformation of the monitored surface, the SEC collects implicit directional strain data in terms of the addition of the two biaxial strains.

1.3 Problem Statement

In previous research, the SEC has performed well on both static and dynamic monitoring of beam structures under pure bending condition without explicit directional information. It was, however, able to only measure strain values to adequate accuracy with the assumption for unidirectional strain field [13, 14]. The information of the direction of the local strain is indispensable to determine multidirectional strain-stress states, local and global deformation and material state, etc., for structural condition assessment and health prognosis. For example, Liu et al. used real time directional strain information from strain gauges and strain gauge rosettes to assess the damage state and estimate the residual useful life of composite specimens in uniaxial and biaxial loading fatigue test with a proposed condition-based prognosis model [15]. In general, the directional strain data is commonly used for structural analysis involved with multi-axial strain fields. Therefore, to expand the application of the SEC from structural surface in uniaxial strain field to structural surface subjected to more complex deformation state, an algorithm to decompose the implicit strain measurement from the SEC into biaxial strain values is needed. Such algorithm is expected to perform in real-time considering the economic benefits related to operation and maintenance that can be achieved with a timely damage detection [16, 17].

1.4 Objective

The primary objective of this thesis is to develop an algorithm to extract the bidirectional strain data from the implicit strain measurement of the SEC in order to improve the applicability of the SEC.

1.5 Methodology

To decompose the biaxial strain measurements from the SEC signal for plate and shell structures, such as a wind turbine blade, strain functions are developed and fitted using a least square estimator (LSE) based on the Kirchhoff plate theory for a thin plate structure. The method requires the enforcement of the strain boundary condition for the biaxial strain decomposition and the displacement and rotation boundary condition for the deflection shape reconstruction.

1.6 Scope

Multiple mathematical formulations for bidirectional strain decomposition are developed and simulated. Initial investigations are conducted on cantilever plate structures under different loading conditions. The performance of the developed algorithms with different formulation are assessed and compared.

Further, several variables including the order of the mathematical formulation, number of applied SECs, load cases, geometry and noise that may influence the performance of the proposed algorithms are studied to determine the optimal formulation for the algorithm. All the algorithm tests and evaluations are based on numerical simulation for the convenience of large sensor amount selection and the constraints in experimental resource.

1.7 Organization of Thesis

The thesis is organized as follows. Chapter 2 reviews signal processing algorithms for strain state and deformation monitoring with sensor networks and strain map related formulations for plate and shell structures. In addition, the problem of decomposing the implicit strain measurement of the SEC is discussed, and two potential formulations for a cantilever test plate are developed and verified.

Chapter 3 evaluates the two formulations by investigating the estimation accuracy of both formulations under the effect of different influencing factors, including the accuracy of boundary conditions, the level of order or expansion of the functions and the noise level in the SEC signal, in order to determine an optimal algorithm for thin plate structural surface.

Chapter 4 further looks into the application of the developed algorithm under more realistic and complex loading conditions, on more irregular geometry and with orthotropic materials and laminated plate section for a preliminary study on the applicability on wind turbine blades. A dual wind pressure time series is simulated on the laminated cantilever plate with irregular surface.

Chapter 5 summarizes the research work, draws conclusions, and indicates limitations. Future investigations improving the strain decomposition algorithm of the SEC are discussed.

CHAPTER 2

ALGORITHM DEVELOPMENT AND VERIFICATION

2.1 Algorithm for Strain and Deformation Monitoring with Sensor Network

The purpose of the SEC sensor network is to provide a real-time strain state and deformation monitoring for large-scale structural surface. However, unlike the widely used strain gauge technique for local points measurement and the full-field optical methods [18], the SEC does not provide explicit strain state directly. Therefore, a real-time algorithm to extract the explicit strain state is necessary for the strain state and deformation monitoring.

A large amount of research has been conducted for strain state and deformation monitoring through the development of sensor network algorithm. Some of them focused on two-dimensional digital image correlation (2D DIC) to measure the deformation and then estimate the full-field strain based on the directly provided full-field displacements [19]. Others looked at the strain-deformation mapping with grid method [20, 21]. Those monitoring was performed for the cases under experimental conditions and with mature sensing techniques that provide explicit information of the direction of the measurements. However, the mapping technique used between the in-plane displacements and the in-plane strains can be still be of interest for developing a suitable mapping algorithm that may draw the direction information out of the SEC signal in a network configuration.

The wind turbine blade that the SEC sensor network is expected to be applied can be categorized as plate and shell structure. For such structural type, Tessler and Spangler developed an inverse finite element method (iFEM) based on the first-order shear-deformation plate theory and a least-squares variational principle to reconstruct three-

dimensional deformation from measured surface strains [22-24]. The iFEM contains a mapping between the measured surface strain state and the 3-D displacements which could be a potential base for the extraction of the biaxial strain hidden in the SEC signal. Initial attempt in this study tried the iFEM approach with classical plate theory by ignoring the transverse shear deformation for thin plate and shell structures. Although the continuity of displacements on element boundaries was enforced to provide a compensation for the loss of the directional information, such loss is still not able to be recovered. Thus, the resulting loss in the rank of the strain-displacement relation matrix disables the inverse process in iFEM. However, the least-squares estimation they used still could be a feasible option for fitting the strain map into the SEC signals.

2.2 Strain Map Formulation for Plate and Shell Structures

For the construction of the strain map of plate and shell structures, a typical way is to develop the shape function and then derive the strain map function based on plate theory. This requires assumptions on the shape functions. From a mathematical point of view, Lancaster and Salkauskas developed a symmetric polynomial form for the least-squares surface-fitting algorithm [25] and Jones et al. used the polynomial form for the shape function bonded with classical plate theory and the least-squares surface-fitting algorithm for the strain-fitting and shape determination of cantilever plate [26]. Bay et al. also used a polynomial shape function for the strain mapping with an extended 3D DIC from 2D DIC technique [27].

Other researchers developed the shape function with a more mechanical base. Rajalingham et al. developed the shape function for a rectangular plate based on the plate characteristic functions by minimizing the energy integral for the plate vibration equation and

used this shape function to find the plate frequencies using the Rayleigh-Ritz method [28]. Their formula, however, is highly nonlinear and contains complex number inside which makes it unusable for a least-squares surface fitting. Instead of deriving the shape function based on energy minimizing, Tian et al. and Zhong et al. developed the shape function based on the governing equation for the bending of a rectangular plate using the double finite integral transform method [29, 30]. Their method avoided using any predetermined deformation functions which makes it a more rational model for plate bending problems and could be extended to different loading and boundary conditions. Also, the derived shape function has a suitable structure for least-squares estimation (will be explained in details in section 2.3.2).

Based on previous literatures, both the polynomial formulation and the double finite integral transform (denoted as a biharmonic formulation) were selected as the shape function (displacement function) for decomposing the biaxial strain from the SEC signal in the strain mapping process with least-squares surface fitting technique. The detailed method will be introduced in the following section.

2.3 Biaxial Strain Decomposition Algorithm based on LSE

Based on the sensing mechanism of the SEC (Eq. 1.5), the measured signal can be processed using the following equation (where S_{SEC} is the output signal of the SEC):

$$S_{SEC} = \frac{\Delta C}{\lambda C} = \varepsilon_x + \varepsilon_y \tag{2.1}$$

Thus, the desired algorithm needs to be able to decompose the two biaxial strains ε_x and ε_y based on the sensing signal S_{SEC} of the SEC. To achieve this objective, a strain map can be fitted from the signals using LSE. Since the type of structure considered here is thin

plate and shell structures, such as wind turbine blade, the classic Kirchhoff plate theory was considered. In order to involve the dependence of the two biaxial strains according to the Kirchhoff plate theory, the equations of ε_x and ε_x for LSE based surface fitting algorithm can be derived from an assumed displacement function $w(x, y)$ based on the following relationship (where z represents the transverse distance from the surface to the centroid of the thin plate section):

$$\varepsilon_x = -z\frac{\partial^2 w}{\partial x^2} \tag{2.2}$$

$$\varepsilon_y = -z\frac{\partial^2 w}{\partial y^2} \tag{2.3}$$

The displacement function $w(x, y)$ needs to be assumed for the LSE surface fitting algorithm and two types of assumptions will be discussed in the following sections. In general, $w(x, y)$ will be a function of x and y coordinates which stands for the sensor locations which can be represented in a matrix form for the full sensor network as Eq. 2.4 (where $\boldsymbol{H}$ is a constant matrix determined by the locations of the SECs in the sensor network and $\boldsymbol{A}$ represents the parameter vector that needs to be solved with the LSE).

$$\boldsymbol{W} = \boldsymbol{HA} \tag{2.4}$$

From Eq. 2.1 – 2.4 ($\boldsymbol{S}$ stands for the SEC signals at all the sensor nodes in the sensor network):

$$\boldsymbol{\varepsilon_x} = -z\frac{\partial^2 \boldsymbol{W}}{\partial x^2} = \boldsymbol{H_x A_x} \tag{2.5}$$

$$\boldsymbol{\varepsilon_y} = -z\frac{\partial^2 \boldsymbol{W}}{\partial y^2} = \boldsymbol{H_y A_y} \tag{2.6}$$

$$\boldsymbol{S} = \boldsymbol{\varepsilon_x} + \boldsymbol{\varepsilon_y} = \boldsymbol{H_s A_s} \tag{2.7}$$

Note that: $\boldsymbol{A} = [\boldsymbol{A_0}|\boldsymbol{A_s}]$; $\boldsymbol{H_s} = [\boldsymbol{H_x}|\boldsymbol{H_y}]$; $\boldsymbol{A_x} \subseteq \boldsymbol{A_s}$, $\boldsymbol{A_y} \subseteq \boldsymbol{A_s}$, $\boldsymbol{A_x} \cap \boldsymbol{A_y} \neq \emptyset$; $\boldsymbol{H_s} \subseteq \boldsymbol{H}$, $\boldsymbol{H_x} \subseteq \boldsymbol{H_s}$, $\boldsymbol{H_y} \subseteq \boldsymbol{H_s}$, $\boldsymbol{H_x} \cap \boldsymbol{H_y} \neq \emptyset$.

Based on Eq. 2.7, since $\boldsymbol{H_s}$ matrix is a constant matrix determined by the sensor locations of the sensor network, the parameter matrix $\boldsymbol{A_s}$ which covers all the parameters in $\boldsymbol{A_x}$ and $\boldsymbol{A_y}$ can be solved using a least-square estimator:

$$\widehat{\boldsymbol{A_s}} = (\boldsymbol{H_s^T H_s})^{-1} \boldsymbol{H_s^T S} \tag{2.8}$$

Because of the dependence of the vectors in the $\boldsymbol{H_s}$ matrix due to $\boldsymbol{H_x} \cap \boldsymbol{H_y} \neq \emptyset$, $\boldsymbol{H_s}$is multi-collinear and thus $\boldsymbol{H_s^T H_s}$ is singular matrix which is not invertible unless the boundary conditions is introduced into it. Therefore, the strain boundary condition can be enforced to the $\boldsymbol{H_s}$ matrix by altering rows with the boundary sensor nodes based the strain boundary conditions before applying Eq. 2.8. The strain boundary conditions may be different from case to case. In this thesis, the boundary condition of a cantilever plate will be considered for the purpose to study the potential of the proposed algorithm to work on a wind turbine blade. Based on the direct strain boundary condition and the strain-stress relationship of thin plate showing below:

$$\sigma_x = \frac{E}{1-\nu^2}\left(\varepsilon_x + \nu\varepsilon_y\right) \tag{2.9}$$

$$\sigma_y = \frac{E}{1-\nu^2}\left(\varepsilon_y + \nu\varepsilon_x\right) \tag{2.10}$$

Take a rectangular cantilever rectangular thin plate in the Cartesian coordinate system with one edge ($x = 0$) fixed as an example. The strain boundary conditions can be listed as follows: (1) for the fixed edge, $\varepsilon_y = 0$; (2) for the two edges with one end on the fixed side and the other end on the free side, $\varepsilon_y = -\nu\varepsilon_x$ because of $\sigma_y = 0$; (3) for the totally free edge, $\varepsilon_x = -\nu\varepsilon_y$ because of $\sigma_x = 0$; (4) consider the bending stress singularity [31, 32], the

boundary condition for the fixed corners is taken as an average of the boundary conditions of the two adjacent edges in terms of $\varepsilon_y = -\frac{\nu}{2}\varepsilon_x$; (5) similarly, the boundary condition for the free corners is implemented in the form of $\varepsilon_y = -\frac{\nu+1/\nu}{2}\varepsilon_x$.

The biaxial strain can be estimated as follows:

$$\widehat{\boldsymbol{\varepsilon_x}} = \boldsymbol{H_x}\widehat{\boldsymbol{A_x}} \tag{2.11}$$

$$\widehat{\boldsymbol{\varepsilon_y}} = \boldsymbol{H_y}\widehat{\boldsymbol{A_y}} \tag{2.12}$$

Afterward, $\boldsymbol{A_0}$ can be solved with the displacement boundary conditions, such that the resulting $\widehat{\boldsymbol{A}} = [\widehat{\boldsymbol{A_0}}, \widehat{\boldsymbol{A_s}}]$ can be used to reconstruct the displacement of the structural surface with the following equation (note that the sensor location related matrix $\boldsymbol{H}$ can be replaced with that determined by any arbitrary locations for solving the displacement at any interested locations):

$$\widehat{\boldsymbol{W}} = \boldsymbol{H}\widehat{\boldsymbol{A}} \tag{2.13}$$

Detailed process will be discussed in the following section for two different assumed formulas for the displacement function $w(x, y)$.

2.3.1 Polynomial formulation

As a potential choice for the displacement function, a polynomial formula can be assumed for the least-squares strain-fitting algorithm [26]. A polynomial to the order of n can be assumed for the transverse deflection of the cantilever plate:

$$\mathrm{w(x,y)} = \sum_{i=0,j=0}^{n} a_{i,j} x^i y^j \tag{2.14}$$

Where $a_{0,0}, \ldots, a_{n,n}$ are parameters that need to be solved, such that they constitute the parameter vector $\boldsymbol{A}$ in Eq. 2.4:

$$\boldsymbol{A} = [a_{0,0}, \dots, a_{i,j}, \dots, a_{n,n}]^T \tag{2.15}$$

Similarly, the $\boldsymbol{H}$ matrix is in the following form for the assumed polynomial displacement function and for a sensor network with the number of SECs to be p:

$$\boldsymbol{H} = \begin{bmatrix} 1 & x_1 & y_1 & x_1^2 & x_1y_1 & y_1^2 & \cdots & x_1^{n-1}y_1^{n-1} & x_1^n y_1^{n-1} & x_1^{n-1}y_1^n & x_1^n y_1^n \\ \vdots & \vdots & \vdots & \vdots & \vdots & \vdots & \vdots & \vdots & \vdots & \vdots & \vdots \\ 1 & x_p & y_p & x_p^2 & x_p y_p & y_p^2 & \cdots & x_p^{n-1}y_p^{n-1} & x_p^n y_p^{n-1} & x_p^{n-1}y_p^n & x_p^n y_p^n \end{bmatrix} \tag{2.16}$$

The formula of biaxial strain (ε_x and ε_y) and the corresponding matrices $\boldsymbol{H_x}$, $\boldsymbol{H_y}$ and vectors $\boldsymbol{A_x}$, $\boldsymbol{A_y}$ can then be obtained as discussed in the previous section using Eqs. 2.2 and 2.3, which are then combined to form the matrix $\boldsymbol{H_s}$ and the vector $\boldsymbol{A_s}$. After enforcing the strain boundary conditions in $\boldsymbol{H_s}$, the biaxial strain can be extracted from the SEC signal using Eqs. 2.8, 2.11 – 2.12. Finally, the displacement can be solved with displacement and rotation boundary conditions as described in the previous section using Eq. 2.13.

2.3.2 Biharmonic formulation

Another equation based on integral transform method was also investigated as a potential function for the LSE based biaxial strain decomposition algorithm. For a cantilever rectangular thin plate, the transverse deflection can be defined as a double finite integral transform (Eq. 2.5) and then be represented as its inverse transform in Eq. 2.6, where $\alpha_m = m\pi/a$, $\beta_n = n\pi/b$, a and b is the length and width of the rectangular plate [29].

$$W_{mn} = \int_0^a \int_0^b W(x,y)\sin\frac{\alpha_m}{2}x\cos\beta_n y dxdy \ \ (m = 1,3,\dots; n = 0,1,2\dots) \tag{2.17}$$

$$\mathrm{W(x,y)} = \frac{2}{ab}\sum_{m=1,3,\dots}^{\infty} W_{m0}\sin\frac{\alpha_m}{2}x + \frac{4}{ab}\sum_{m=1,3,\dots}^{\infty}\sum_{n=0,1,2\dots}^{\infty} W_{mn}\sin\frac{\alpha_m}{2}x\cos\beta_n y \tag{2.18}$$

In this case, the parameters $W_{mn}(\mathrm{m} = 1,3,\dots;\ \mathrm{n} = 0,1,2,\dots)$ constitute the parameter vector $\boldsymbol{A}$ in Eq. 2.4:

$$\boldsymbol{A} = [W_{1,0}, W_{3,0}, \dots, W_{m,n}]^T \ (\mathrm{m} = 1, 3, \dots; \ \mathrm{n} = 0, 1, 2, \dots) \tag{2.19}$$

And the $\boldsymbol{H}$ matrix is in a different form from the polynomial formula for a sensor network with p SECs ($\mathrm{m} = 1, 3, \dots; \ \mathrm{n} = 0, 1, 2, \dots$):

$$\boldsymbol{H} = \begin{bmatrix} sin\frac{\alpha_1}{2}x_1 & \cdots & sin\frac{\alpha_m}{2}x_1 & sin\frac{\alpha_1}{2}x_1 cos\beta_0 x_1 & \cdots & sin\frac{\alpha_m}{2}x_1 cos\beta_n y_1 \\ \vdots & \vdots & \vdots & \vdots & \vdots & \vdots \\ sin\frac{\alpha_1}{2}x_p & \cdots & sin\frac{\alpha_m}{2}x_p & sin\frac{\alpha_1}{2}x_p cos\beta_0 y_p & \dots & sin\frac{\alpha_m}{2}x_p cos\beta_n y_p \end{bmatrix} \tag{2.20}$$

With Eq. 2.19 and Eq. 2.20, the biaxial strain can be extracted from the SEC signal and the deflection shape can be reconstructed using the LSE process with Eqs. 2.2 – 2.13. For the boundary condition enforcement, it can be seen that Eq. 2.18 satisfies the boundary condition for transverse deflection of the cantilever plate, but not the rotation and strain boundary condition at the fixed support. Tian et al. enforced those boundary conditions by involving the governing equation for different behaviors including plate bending and free vibration [29, 30]; however, such approach requires changes in final formulation under different targeted behaviors and involves loading information in the formula which limits the applicability and provokes longer computation time. Since the objective of this research only focused on the strain and it is possible to apply boundary condition by altering the rows in the $\boldsymbol{H_s}$ matrix as discussed in the previous section, the strain boundary condition can be enforced separately in the LSE algorithm instead of the shape function itself.

Further, this biharmonic function consisting of periodic equations represents m and n mode shapes in x and y directions. Although Tian et al. used up to 100 terms for the expansion of Eq. 22 to achieve adequate accuracy for the analytical solution of a bending plate, fewer terms were used in this research.

2.4 Design of the Test Plate and Numerical Simulation for Algorithm Verification

To verify the capability of the LSE based algorithm to extract biaxial strain from the SEC signal, both algorithms were simulated on a structural surface. Since a biaxial strain field is needed and the algorithm is expected to be applied on large structural surface such as the surface of a wind turbine blade, a thin cantilever plate was used for the first simulation.

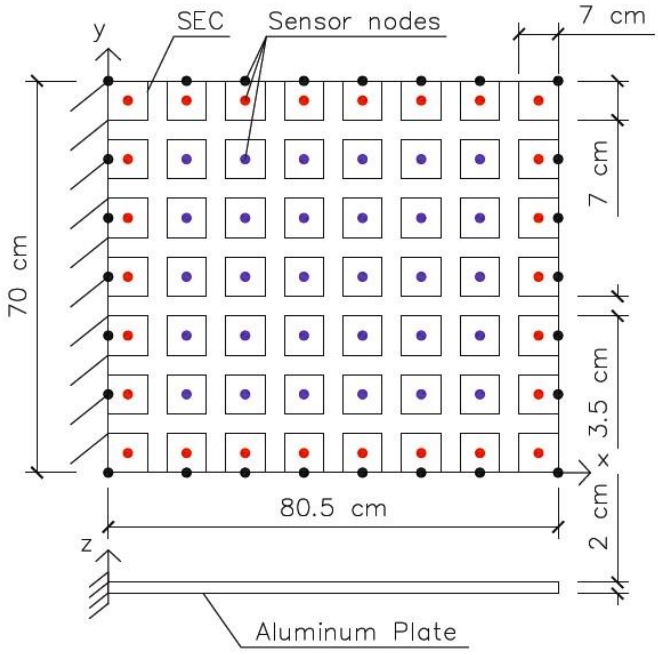

Figure 2.1: Test plate and matrix SEC (7 × 7 cm each) configuration

Based on the SEC fabrication dimension available for application (7 × 7 cm) [33] and the thin plate theory, the cantilever plate geometry (80.5 × 70 × 2 cm) and SEC arrangement (a matrix form) was created in a Cartesian coordinate (Fig. 2.1). Since a proper strain boundary condition (BC) is necessary for the algorithm as discussed previously, the outer SECs were located with sides on the boundary to make the outer sensor nodes as close to the boundary as possible, which are showed as red nodes in Fig.2.1. The center of each SEC is taken as sensor node marked as solid nodes (blue and red nodes). However, the strain BC

would be more accurate if sensors were directly locates on the boundaries. The SEC signal at the exact boundary nodes (black nodes in Fig. 2.1) was used to provide ideal strain boundaries for the initial algorithm verification.

Table 2.1: Load case information

Load case	Load type	Applied Location	Magnitude (KN)
(a)	Pressure	Full plate top surface	$10\sin(\frac{\pi}{4}t)$
(b)	Force	Center-tip	$2\sin(\frac{\pi}{4}t)$
(c)	Force	Corner	$1.5\sin(\frac{\pi}{4}t)$

Where *t* stands for time in seconds.

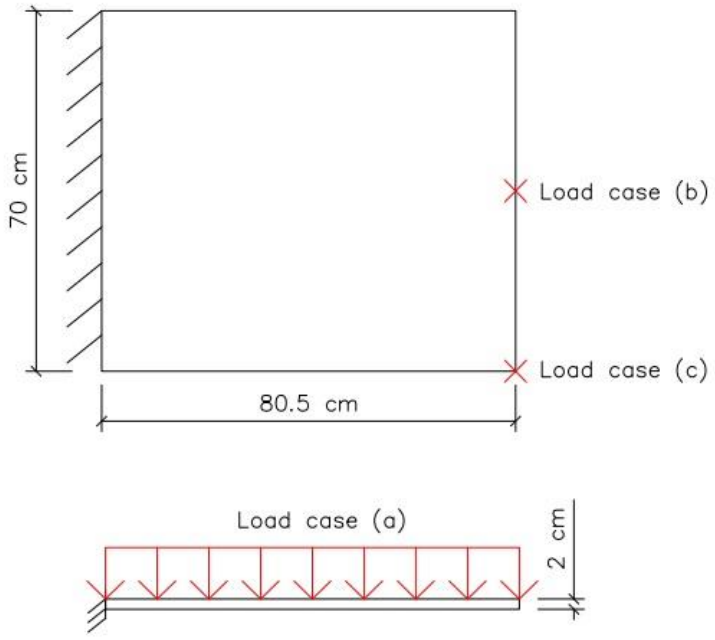

Figure 2.2: Load cases on the cantilever test plate

The numerical simulations of the test plate and SEC arrangement under different load cases were performed with ANSYS 14.5. Isotropic material (aluminum) was chosen for the initial verification of the proposed algorithm. Four-nodes shell element with both bending

and membrane behavior was used for the finite element analysis. One of the shorter side of the plate is fixed and three types of time dependent load case was applied on the cantilever plate to consider both pure bending condition and the effect of stress concentration and torsion as shown in Table 2.1 and Fig. 2.2, including a pressure on full plate (load case (a)), a concentrated load at the center of the free side (center-tip) of the cantilever plate (load case (b)) and a concentrated load at one corner of the free side of the cantilever plate load case (c)). The time duration of the load was 10 s and the load was ramped with time step 0.2s to ensure adequate smoothness. The maximum deflection of the cantilever plate under each load case is as follows: (a) 1.0361cm; (b) 1.0226cm; (c) 0.9928 cm. The biaxial surface strain at each sensor node under the three load cases was simulated and used to construct the SEC time series signal for each load case based on the SEC signal to strain equation (Eq. 2.1) mentioned previously. For the initial algorithm test, there is no noise added to the constructed analytical signal. Noise will be introduced to the analytical signal in Chapter 3 to investigate the influence of noise in the proposed algorithm.

2.5 Verification of Algorithm

Using the three sets of time series of the SEC signal constructed in the test plate simulation as the input to the algorithm, verification tests under three types of loading condition were conducted for the LSE algorithm with both polynomial and biharmonic formulation. To initially simulate the algorithm with more accurate BCs, the proposed algorithm with the strain BC applied on the ideal boundary sensor nodes (black nodes in Fig. 2.1) were tested for both the polynomial and the biharmonic formulation. For the reason that the results of the boundary sensor nodes were obtained by the BC instead of the algorithm, only the estimation error of the inner sensor nodes (blue nodes in Fig. 2.1) was assessed.

2.5.1 Verification of the LSE algorithm with polynomial formulation

The verification test was conducted for the LSE algorithm with polynomial formulation under pure bending, concentrated load and bending-torsion combined loading condition, with the ideal BC. The performances of the algorithm were compared between load cases through the comparison between the estimated and analytical biaxial strain. To rule out the cancelation between positive and negative errors which may lead to inaccurate error evaluation, the errors were considered in a root mean squared error (RMSE) as well as a mean absolute percentage error (MAPE).

With the enforcement of the strain BC on the ideal boundary sensor nodes, the biaxial strain data was decomposed by the LSE-polynomial algorithm from the constructed SEC signal under the three simulated load cases. The results from the algorithm estimation were compared with the analytical biaxial strain value from the simulation in Fig 2.3 to Fig 2.10.

By looking at the RMSE of all the non-boundary sensor nodes together with the load magnitude versus time (Figs. 2.3 – 2.4), it can be seen that the residual error grows as the load increases. However, the MAPE (Figs. 2.5 – 2.6) seems to be approximately consistent in all three load cases in spite of the magnitude of the applied load, except for the time point with load close to zero. It is probably because of the low value in analytical strain leading to a jump in the percentage error between estimated and analytical strain. Nonetheless, for the increasing jump in error, the maximum is under 5% for the biaxial strain in all three load cases (Figs. 2.5 – 2.6) which is acceptable for a very low strain field without the chance of damage.

Overall, the MAPE time series appears to suggest that the performance of the proposed LSE-polynomial algorithm is stable under conditions including bending, stress

concentration and torsion. Moreover, based on Figs. 2.3 – 2.6, both the RMSE and MAPE turn to be relatively higher in load case 2 compared with the other load cases, which may due to the effect of stress concentration. Within the three load cases, the LSE-polynomial exhibited the highest accuracy under pure bending loading condition (load case (a)). Although the accuracy of the estimation is relatively lower when there are influence from stress concentration and torsion, the maximum MAPE in all load cases (around 9.25% for strain x and 22.5% for strain y) is still small (Fig. 2.3 – 2.6) as a global error on all the non-boundary sensor nodes.

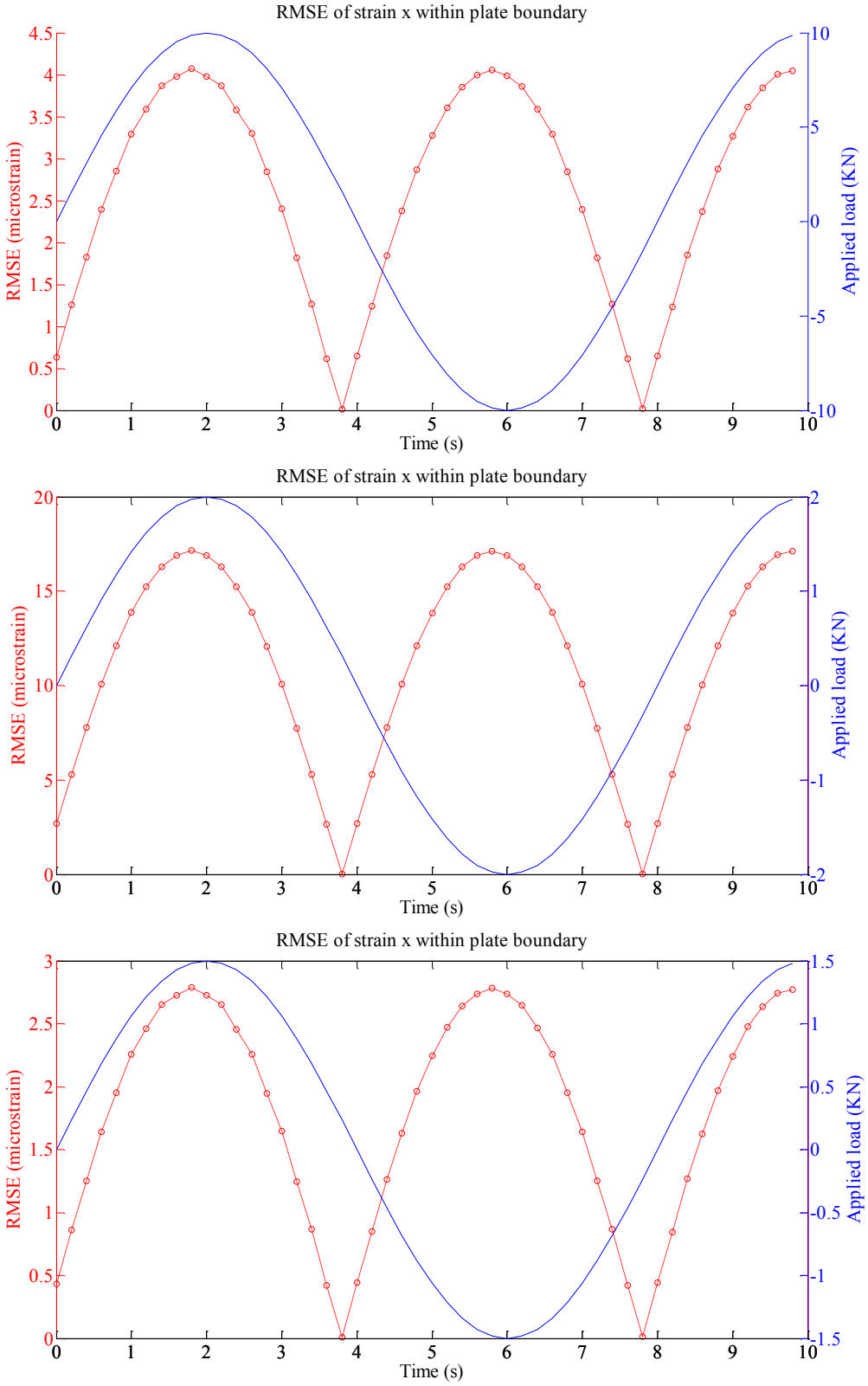

Figure 2.3: Time series of RMSE of strain x at all the non-boundary sensor nodes estimated with LSE-polynomial algorithm (ideal BC enforcement) under load case (a) (top), (b) (middle) and (c) (bottom)

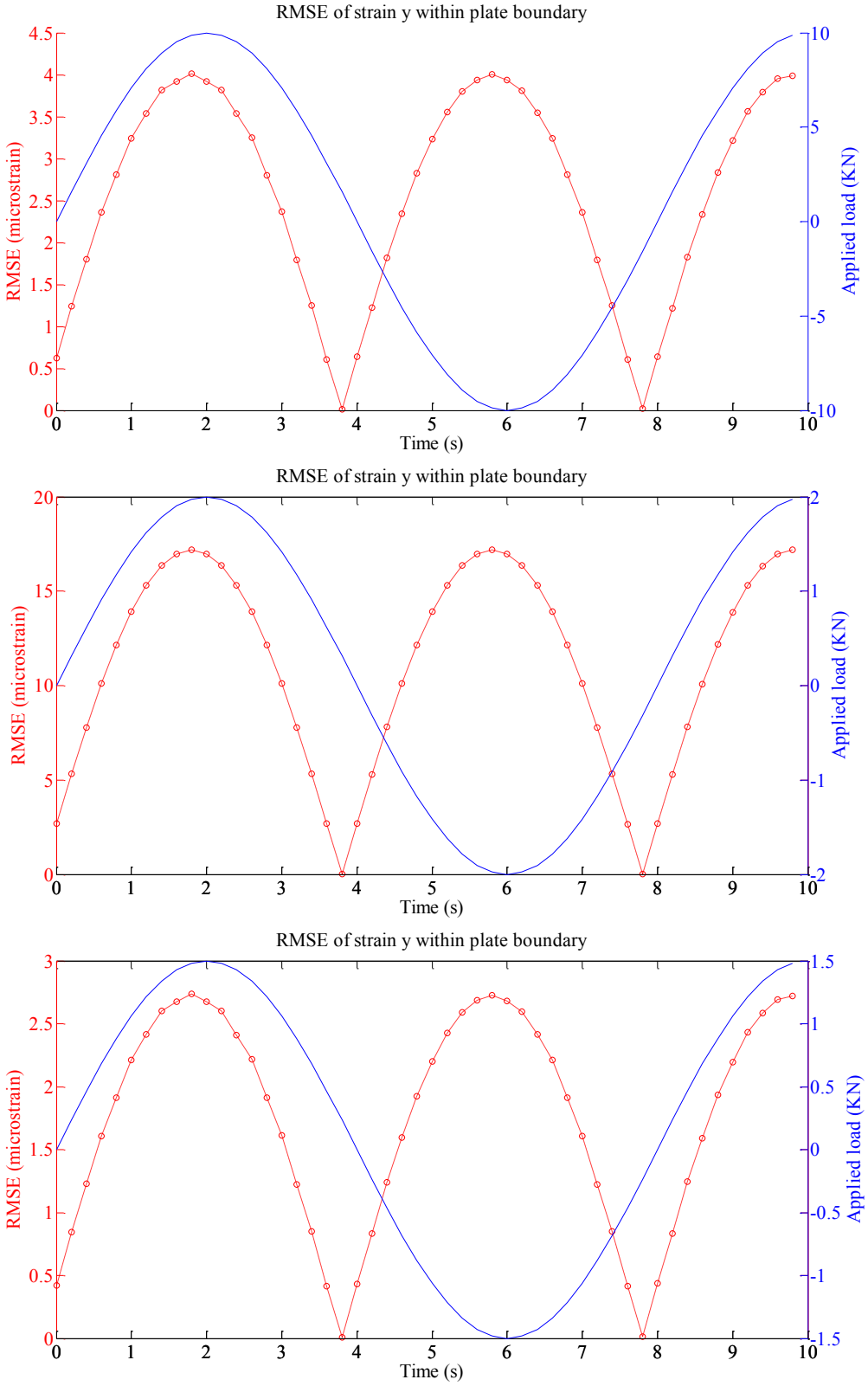

Figure 2.4: Time series of RMSE of strain y at all the non-boundary sensor nodes estimated with LSE-polynomial algorithm (ideal BC enforcement) under load case (a) (top), (b) (middle) and (c) (bottom)

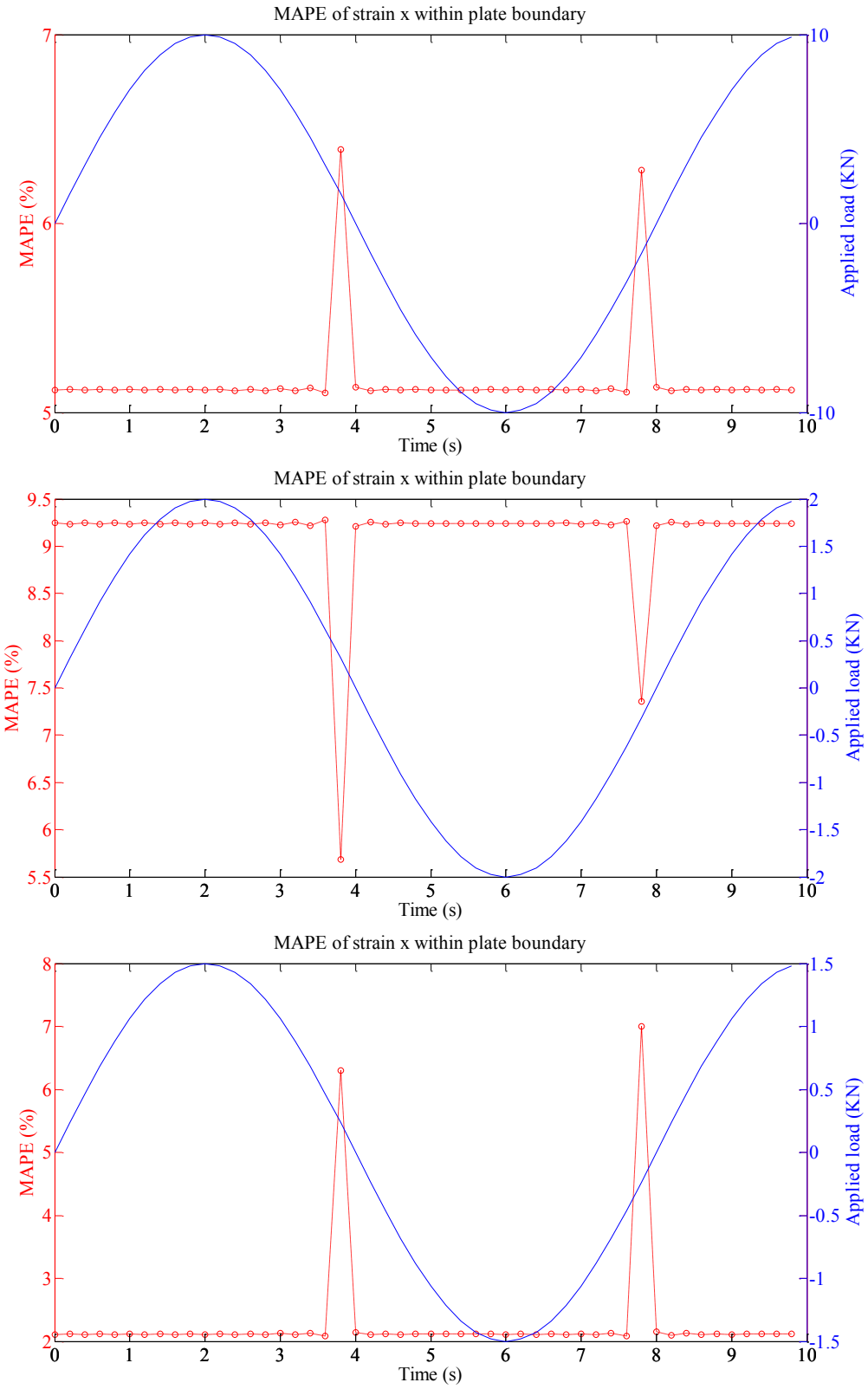

Figure 2.5: Time series of MAPE of strain x at all the non-boundary sensor nodes estimated with LSE-polynomial algorithm (ideal BC enforcement) under load case (a) (top), (b) (middle) and (c) (bottom)

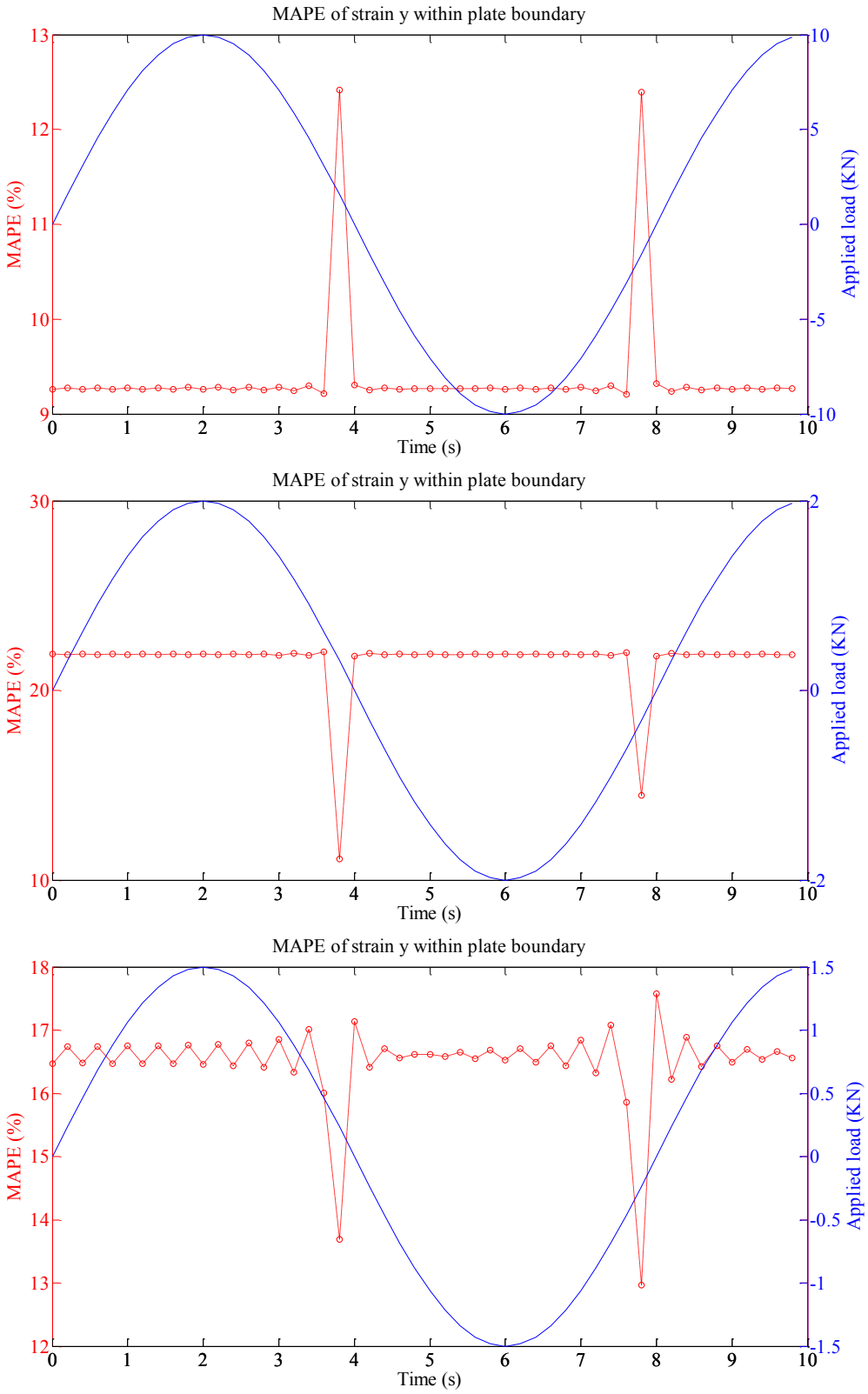

Figure 2.6: Time series of MAPE of strain y at all the non-boundary sensor nodes estimated with LSE-polynomial algorithm (ideal BC enforcement) under load case (a) (top), (b) (middle) and (c) (bottom)

The local error also needs to be evaluated. By considering the percentage error for each non-boundary sensor nodes on an average base over the full time duration of the applied load (10 s), the MAPE contour plots of the estimation of strain x and strain y within the plate boundary are given in Fig. 2.7 and Fig. 2.8. Based on the MAPE contour plots for load cases (a) – (c), it is clear that the highest error is concentrated on the free corners and the relatively higher error is distributed around where the stress concentration generated by the point load (Fig. 2.7 – 2.8). The reason for the highest error at free corners is probably because of the loss of accuracy of the assumption due to corner singularities. Since the BC is not continuous at the plate corners as mentioned before, the averaged corner BC is possibly less accurate. Especially for the free corner, the BC varies much more from the fix-free side to the free side; such conflict may be sharper and influenced more by other factors such as the length and width ratio. Thus, tough the free corner BC was not applied in the algorithm process; the afterward enforced-back BC may still be inaccurate. However, most of the plate surface has a MAPE around 5% for strain x estimation and around 10% for strain y estimation for all three load cases. Such result showed that the LSE-polynomial algorithm performed well on the major surface (even including the area near fixed side where is in relatively higher strain field and damage is more likely to occur at) of the cantilever plate under bending, stress concentration and torsion condition. Moreover, the less accurate estimation area focuses on the free corners where has less chance of damage because of much lower strain values compare to the other parts of the cantilever plate.

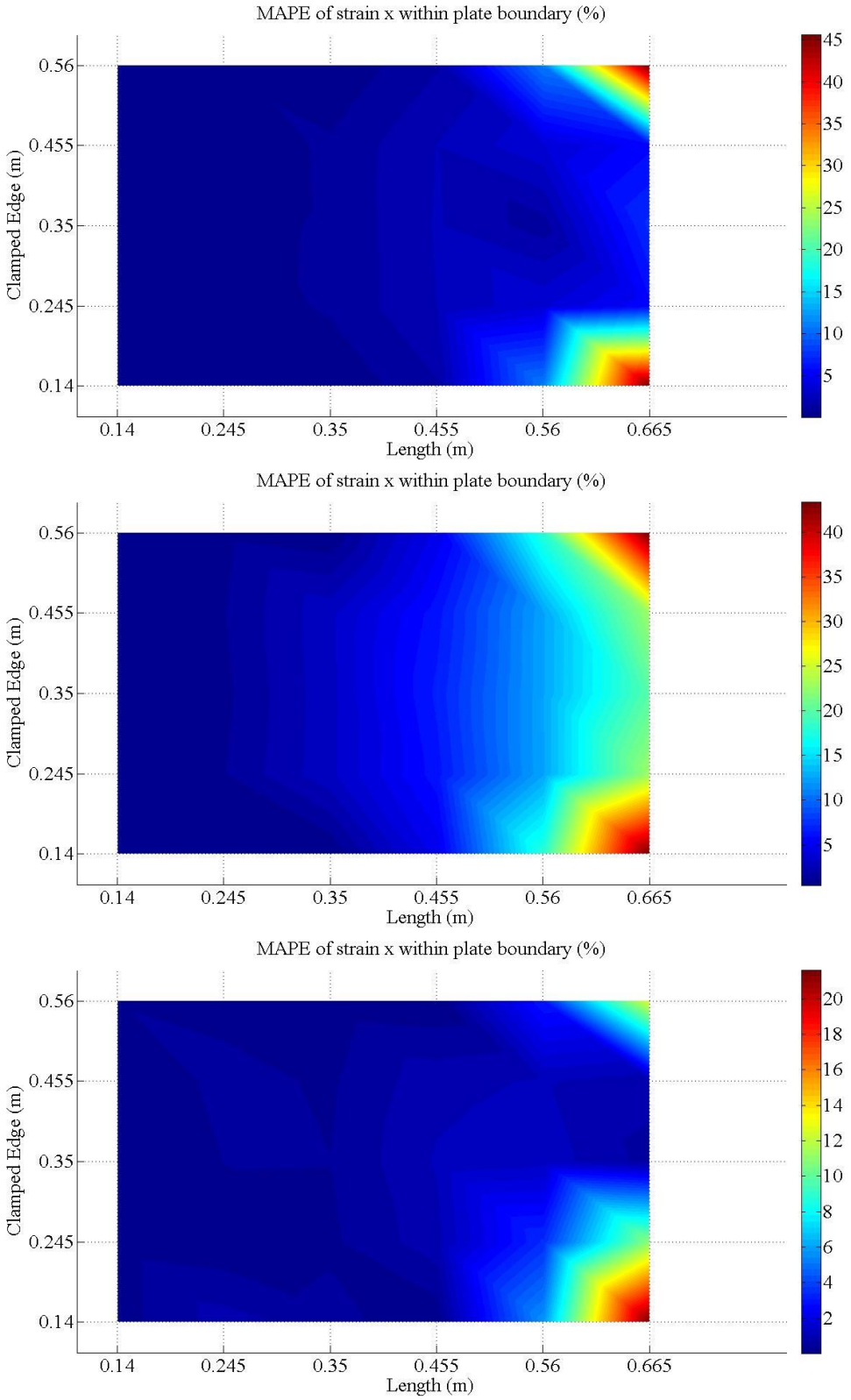

Figure 2.7: MAPE contour plot of strain x within plate boundary estimated with LSE-polynomial algorithm (ideal BC enforcement) under load case (a) (top), (b) (middle) and (c) (bottom)

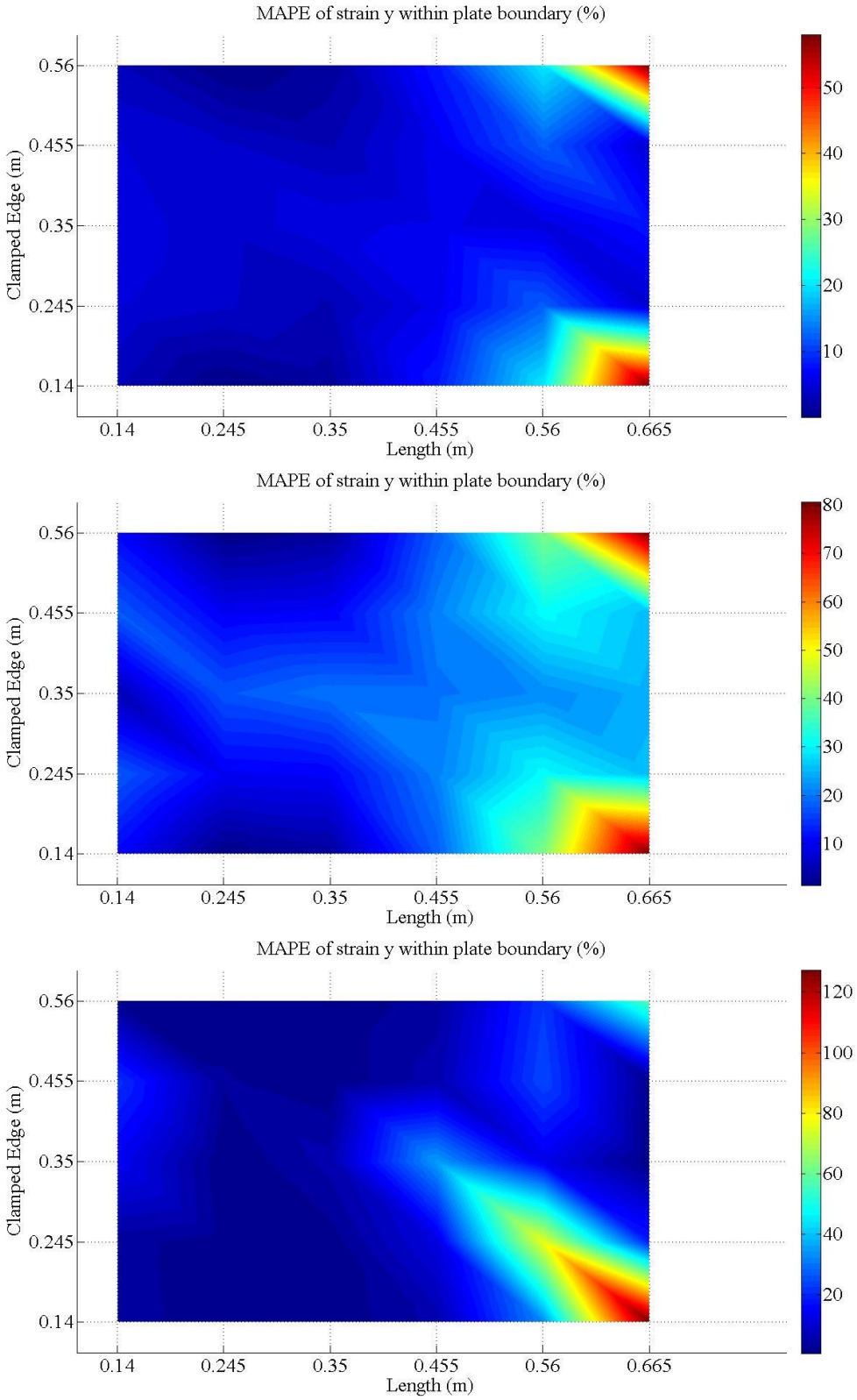

Figure 2.8: MAPE contour plot of strain y within plate boundary estimated with LSE-polynomial algorithm (ideal BC enforcement) under load case (a) (top), (b) (middle) and (c) (bottom)

Overall, a direct comparison between the estimation results and the analytical strain values was performed at the time point (6 s) with the highest load magnitude on the full plate including the boundary sensor nodes. The biaxial strain extracted by the LSE-polynomial algorithm from the SEC signal compared with the analytical biaxial strain from the simulation are plotted in Figs. 2.9 – 2.10 for each load case in terms of 3-D maps. Figs. 2.9 – 2.10 also confirm that the LSE-polynomial algorithm performs well for the biaxial strain extraction from SEC signals on the cantilever plate under all three load cases and the bad performance only occurs at corners where are less important for damage detection.

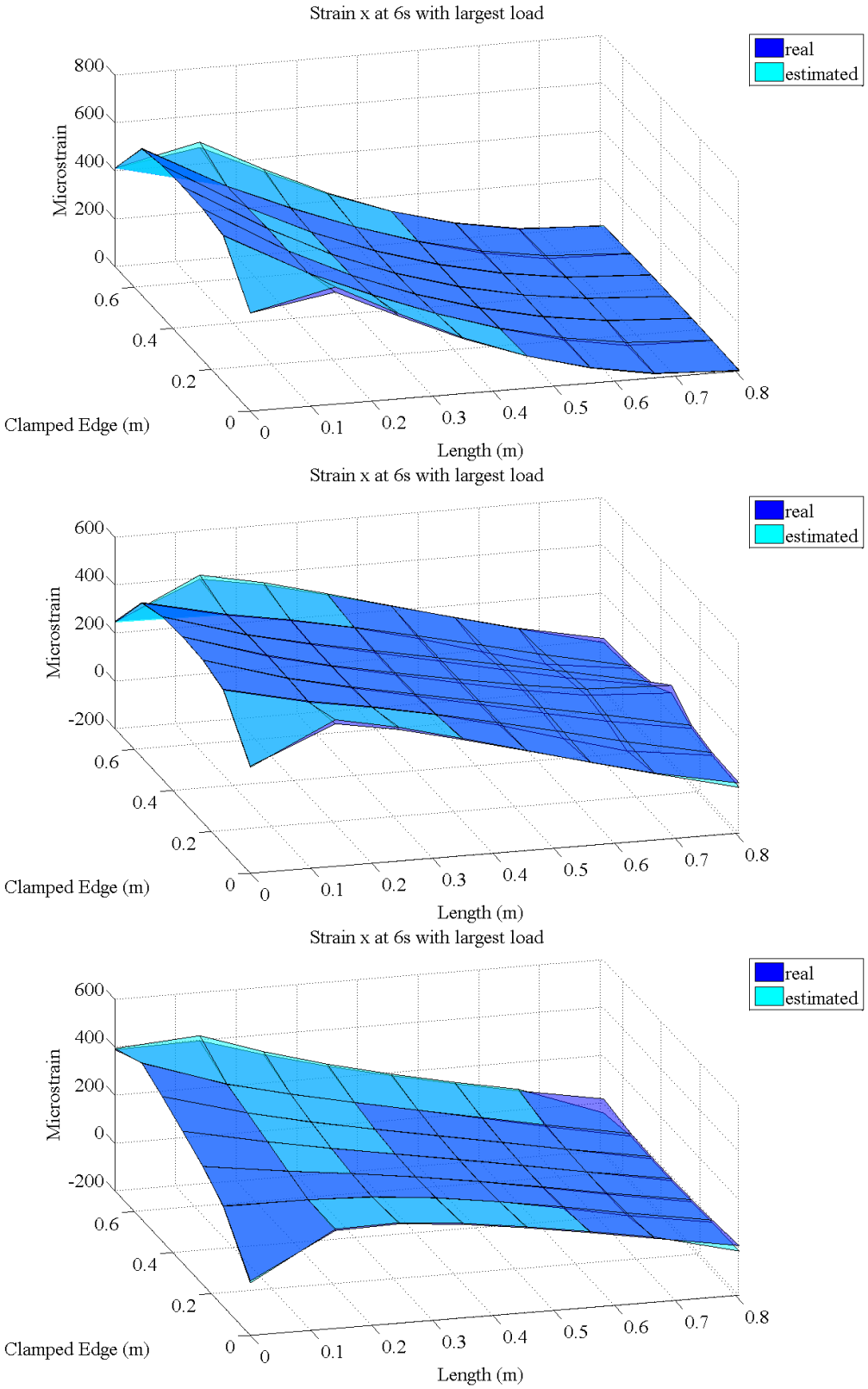

Figure 2.9: 3-D map (analytical and estimated) of strain x estimated with LSE-polynomial algorithm (ideal BC enforcement) at 6 s under load case (a) (top), (b) (middle) and (c) (bottom)

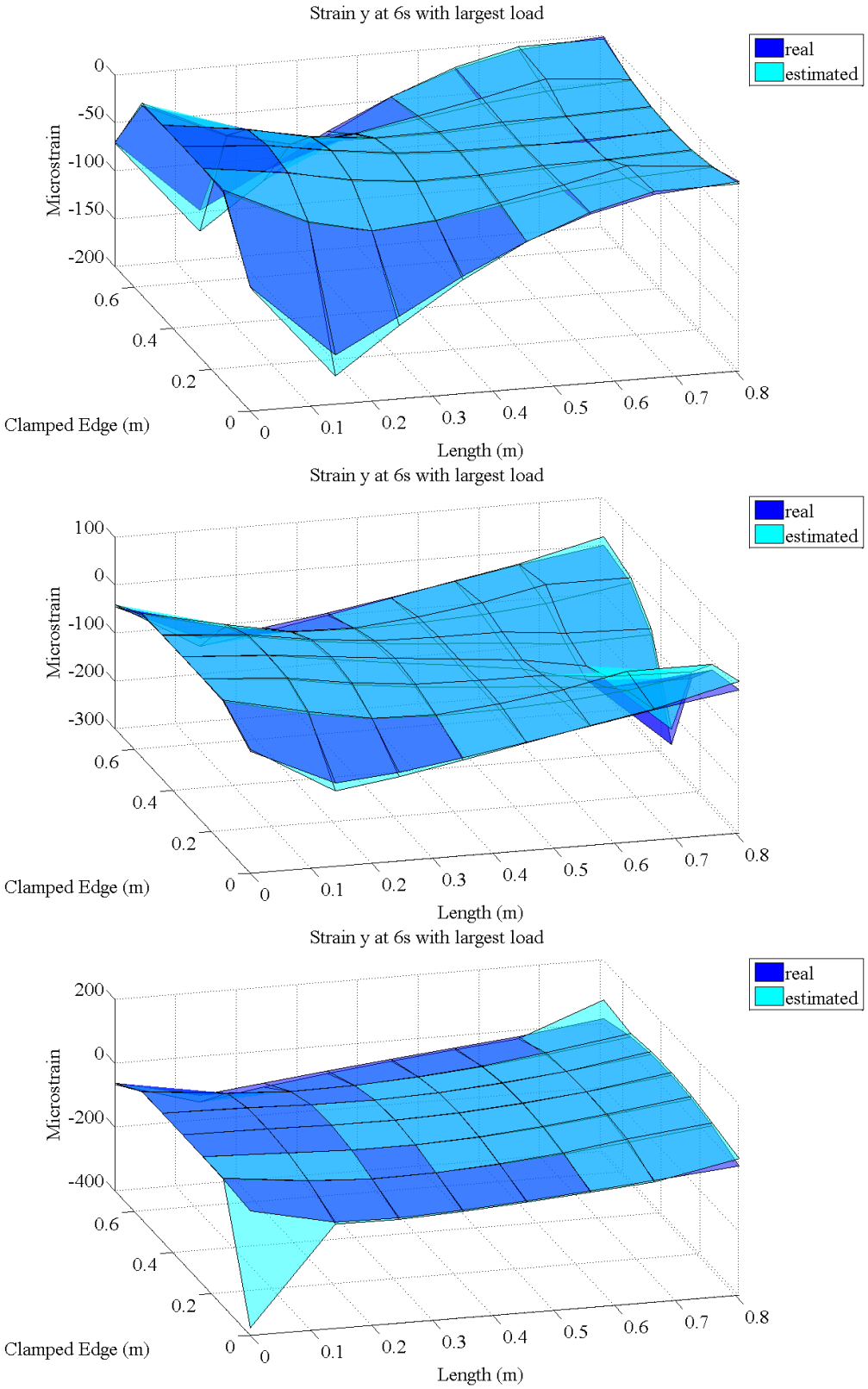

Figure 2.10: 3-D map (analytical and estimated) of strain y estimated with LSE-polynomial algorithm (ideal BC enforcement) at 6 s under load case (a) (top), (b) (middle) and (c) (bottom)

2.5.2 Verification of the LSE algorithm with biharmonic formulation

Similarly, the LSE algorithm with biharmonic formulation was verified under the three simulated load cases with the ideal BC. Results under the three load cases were discussed for each BC enforcement condition. For simplicity, only the global and local MAPE versus time and sensor node coordinate respectively were evaluated. With the strain BC on the ideal boundary sensor nodes, the error of the biaxial strain extraction by the LSE-biharmonic algorithm is given in terms of MAPE over time and over the surface within the plate boundary in Figs. 2.11 – 2.16.

By comparing the MAPE at all the non-boundary sensor nodes from LSE-biharmonic formulation with that from LSE-polynomial formulation over time (Figs. 2.11 – 2.12 and Figs. 2.5 – 2.6), it can be seen that the LSE-biharmonic formulation exhibites similar behavior as the LSE-polynomial formulation at the zero load time point and performed stably elsewhere. But the global MAPE over time of the LSE-biharmonic formulation is overall higher than the LSE-polynomial formulation, especially for the strain with relatively smaller value (strain y) and when torsion comes in.

Likewise, the local MAPE of the LSE-biharmonic formulation over the plate surface inside the plate boundary also turns out to be higher than the LSE-polynomial formulation in general based on Fig. 2.13 – 2.14 and Fig. 2.7 – 2.8, especially under bending-torsion combined loading condition (load case (c)). In addition, the distribution of the highest local MAPE of the LSE-biharmonic formulation on the plate surface looks less concentrated than that of the LSE-polynomial formulation (Fig. 2.13 – 2.14 compared with Fig. 2.7 – 2.8): Instead of focusing on the free corners, the highest MAPE of the LSE-biharmonic formulation concentrates on the area with strain values close to zero (the free side for strain x

and the fixed side for strain y); although the MAPE seems to be higher at the location with stress concentration for both formulations, the negative effect of stress concentration on the distribution of MAPE seems to be bigger for the biharmonic formulation. The reason for such difference is probably the insufficient mode shapes considered in the biharmonic formulation to adequately represent the total deflection shape.

To summarize, although the performance of the LSE-biharmonic formulation is slightly worse than the LSE- polynomial formulation overall, it can still provide good accuracy on biaxial strain estimation for a major part of the plate surface with current mode shapes considered, especially under symmetric loading cases (load case (a) and (b)) (Figs. 2.13 – 2.16), and may perform better when raise the number of the mode shapes included in the formulation. Further potential improvement of the LSE-biharmonic formulation will be discussed in the following chapter 3.

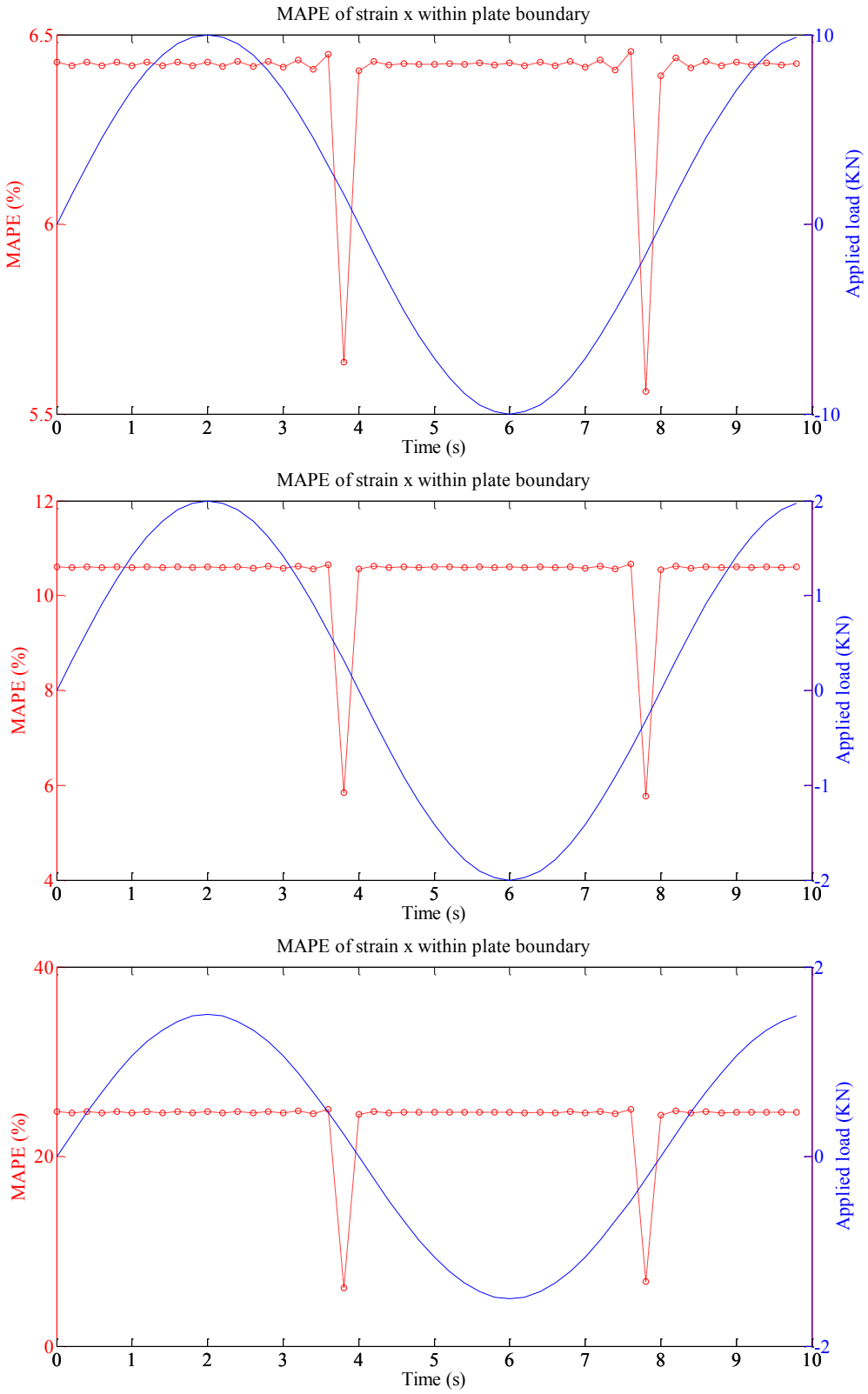

Figure 2.11: Time series of MAPE of strain x at all the non-boundary sensor nodes estimated with LSE-biharmonic algorithm (ideal BC enforcement) under load case (a) (top), (b) (middle) and (c) (bottom)

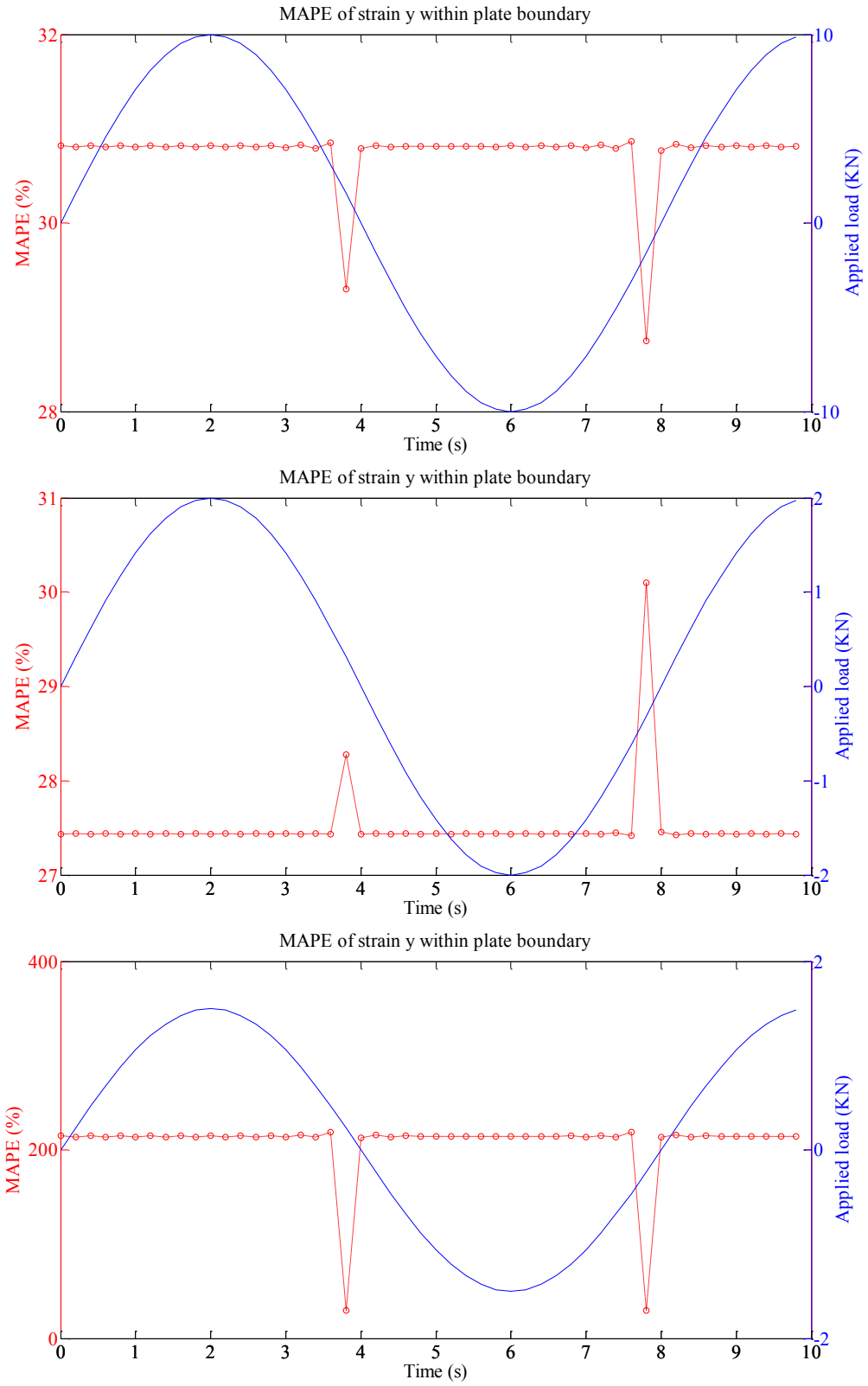

Figure 2.12: Time series of MAPE of strain y at all the non-boundary sensor nodes estimated with LSE-biharmonic algorithm (ideal BC enforcement) under load case (a) (top), (b) (middle) and (c) (bottom)

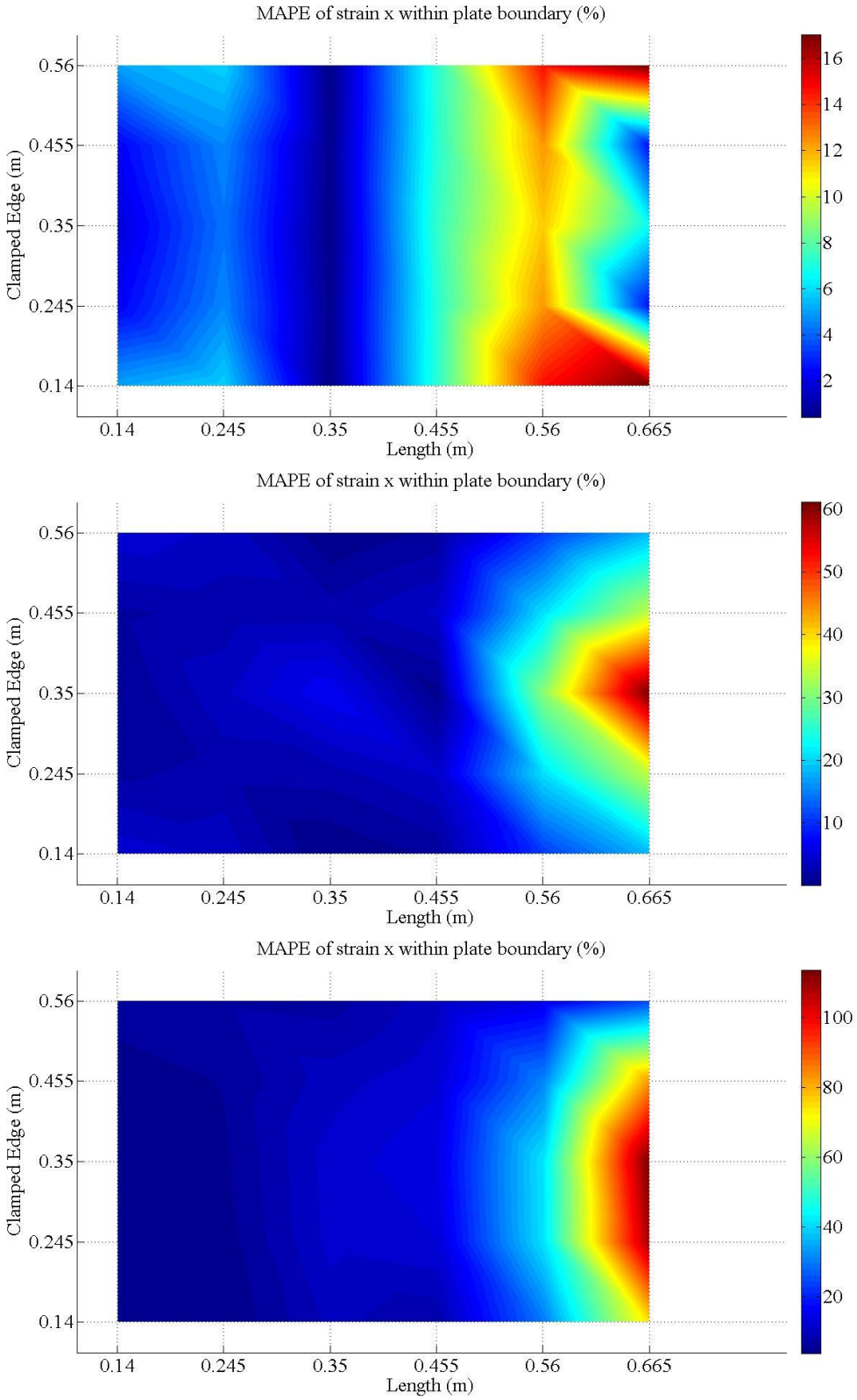

Figure 2.13: MAPE contour plot of strain x within plate boundary estimated with LSE-biharmonic algorithm (ideal BC enforcement) under load case (a) (top), (b) (middle) and (c) (bottom)

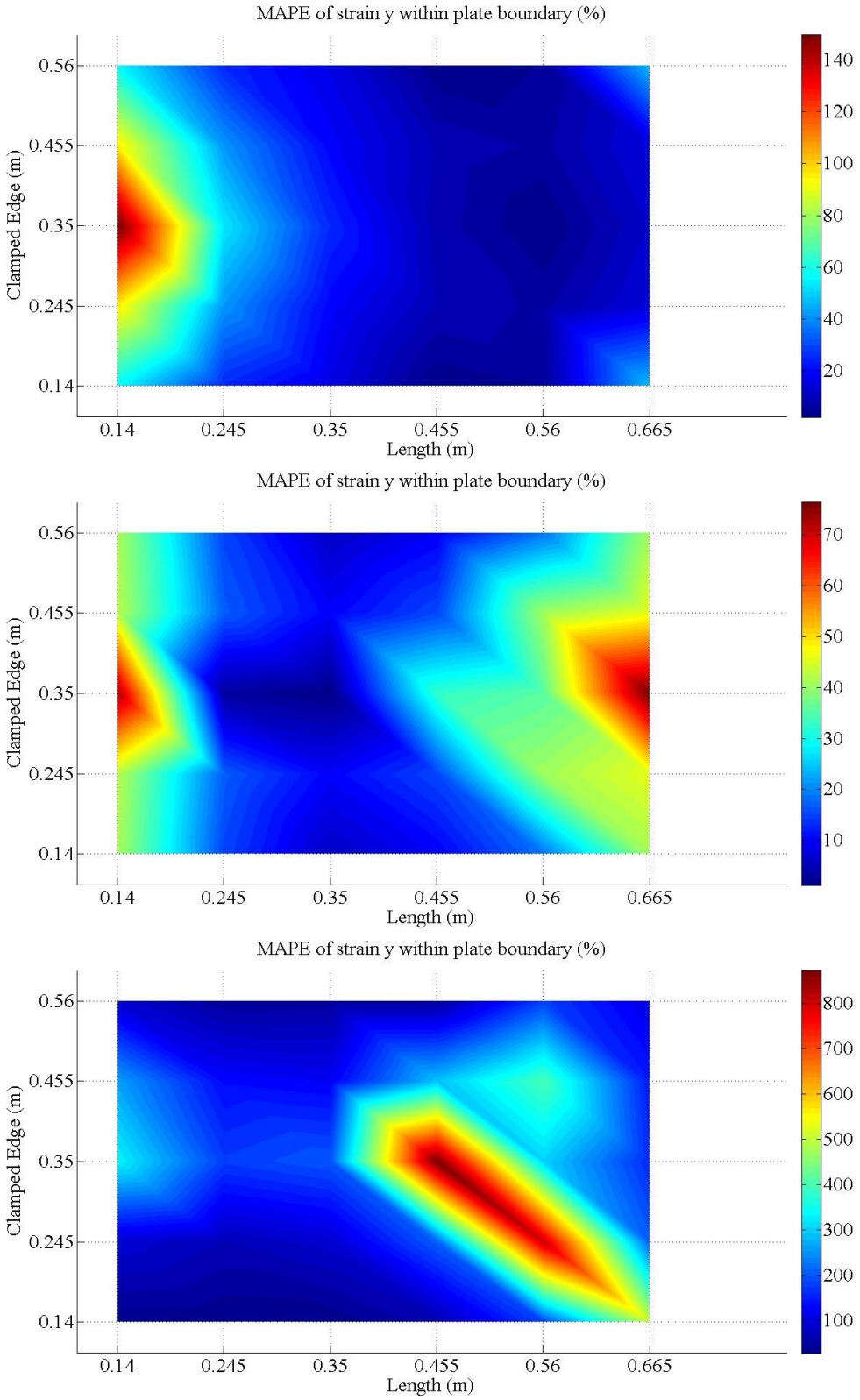

Figure 2.14: MAPE contour plot of strain y within plate boundary estimated with LSE-biharmonic algorithm (ideal BC enforcement) under load case (a) (top), (b) (middle) and (c) (bottom)

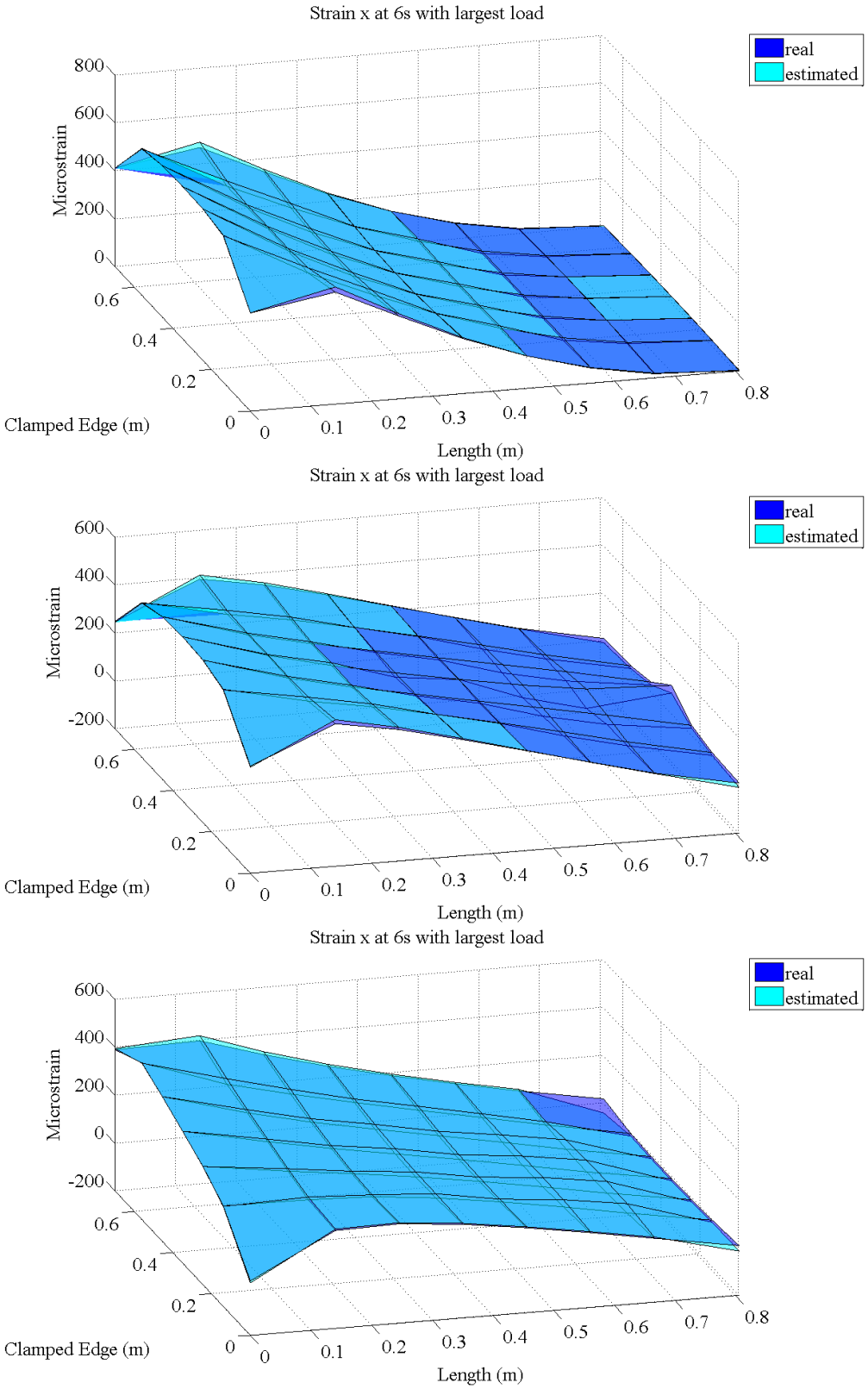

Figure 2.15: 3-D map (analytical and estimated) of strain x estimated with LSE-biharmonic algorithm (ideal BC enforcement) at 6 s under load case (a) (top), (b) (middle) and (c) (bottom)

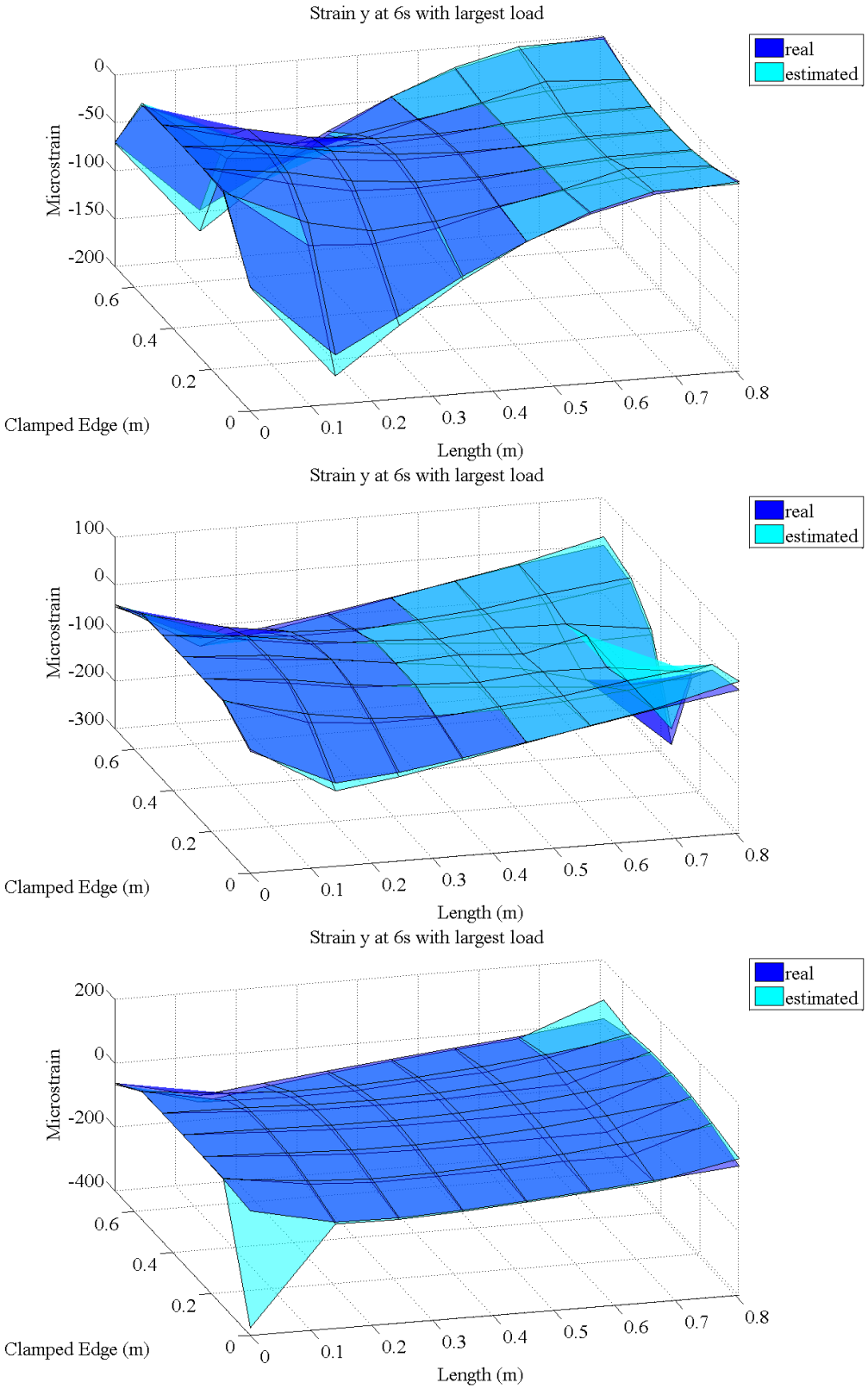

Figure 2.16: 3-D map (analytical and estimated) of strain y estimated with LSE-biharmonic algorithm (ideal BC enforcement) at 6 s under load case (a) (top), (b) (middle) and (c) (bottom)

CHAPTER 3

EVALUATION OF ALGORITHM FORMULAS UNDER DIFFERENT INFLUENCING FACTORS

3.1 Evaluation of Algorithm Formulations under the Influence of Boundary Condition Enforcement

The proposed LSE algorithm with both polynomial and biharmonic formulations have been verified under three load cases in Chapter 2 with ideal BC enforcement. However, the ideal BC enforcement is not able to be fulfilled in practice. The SECs can only be installed with their sides touching the boundary to locate the boundary sensor nodes as close as possible to the boundary. Therefore, the boundary conditions can only be applied on the outer sensor nodes (red nodes in Fig. 2.1) as a modeled BC enforcement instead. The effect of such shift in the location of the BC enforcement is investigated for both the LSE-polynomial and LSE-biharmonic formulation.

3.1.1 Effect of the modeled BC enforcement on the LSE-polynomial algorithm

The influence on the performance of the algorithm from the compromise on BC enforcement is evaluated with analytical and estimated strain contour plots qualitatively and overall MAPE and standard deviation (SD) of percentage error (PE) quantitatively for simpler and clearer comparison. The biaxial strain extraction results with ideal and modeled BC enforcement are compared for the LSE-polynomial algorithm under the simulated three load cases in Figs. 3.1 – 3.6 (the strain contour plot is smaller for the modeled BC enforcement because of the loss of information on the exact boundary sensor nodes (black nodes in Fig. 2.1)). The results are evaluated between analytical strain contour plot from

simulation and the estimated strain contour plot from algorithm at the time with the largest applied load for all load cases (6 s). There are only slight changes in the estimated strain contour plots when the BC enforcement changes from ideal to modeled and they all match the analytical strain contour plot well (except for the corner result under load case (c) which is the bending-torsion combined loading condition).

Table 3.1: Performance of the LSE-polynomial algorithm under differente BC enforcements

Load case	Evaluation item	Strain estimation direction	Ideal BC enforcement	Modeled BC enforcement
(a)	MAPE (%)	x	5.17	5.72
		y	9.39	31.07
	SD of PE (%)	x	11.47	4.53
		y	14.78	26.65
(b)	MAPE (%)	x	9.13	5.84
		y	21.54	18.36
	SD of PE (%)	x	11.64	8.62
		y	18.82	22.08
(c)	MAPE (%)	x	2.30	5.45
		y	16.48	56.83
	SD of PE (%)	x	5.14	6.32
		y	31.20	53.69

Further, Table 3.1 compares the MAPE and SD of PE of all the estimation results of all the non-boundary sensor nodes over the test time duration. In all the three load cases, the MAPE of the estimation of strain x did not vary much from the estimation under ideal BC enforcement and that under modeled BC enforcement. On the contrary, the change of the MAPE of the estimation of strain y is relatively higher; especially for load case (c) (the growth of MAPE is about 40%). On one hand, the cause may be the higher sensitivity in percentage error for smaller values (strain y) compared to larger values (strain x). On the

other hand, this maybe caused by the rapidly varying strain field versus location due to the unsymmetrical loading in load case (c), which makes the imperfection of the BC enforcement becomes more noticeable. Such trend is also shown in the SD of PE. As a result, although the MAPE of strain y estimation is much higher when the BC enforcement is imperfect, the corresponding higher SD for PE and similar strain field estimation shows in Fig. 3.1 – 3.6 indicate that the higher MAPE is probably raised by the relatively worse estimation for the area close to the free corners, which is the less important part in damage detection and leave the performance of the estimation of a major part of the plate surface to be with much higher accuracy. Therefore, it can be drawn that the LSE-polynomial algorithm is able to work with adequate accuracy with imperfection in the BC enforcement (the modeled BC enforcement).

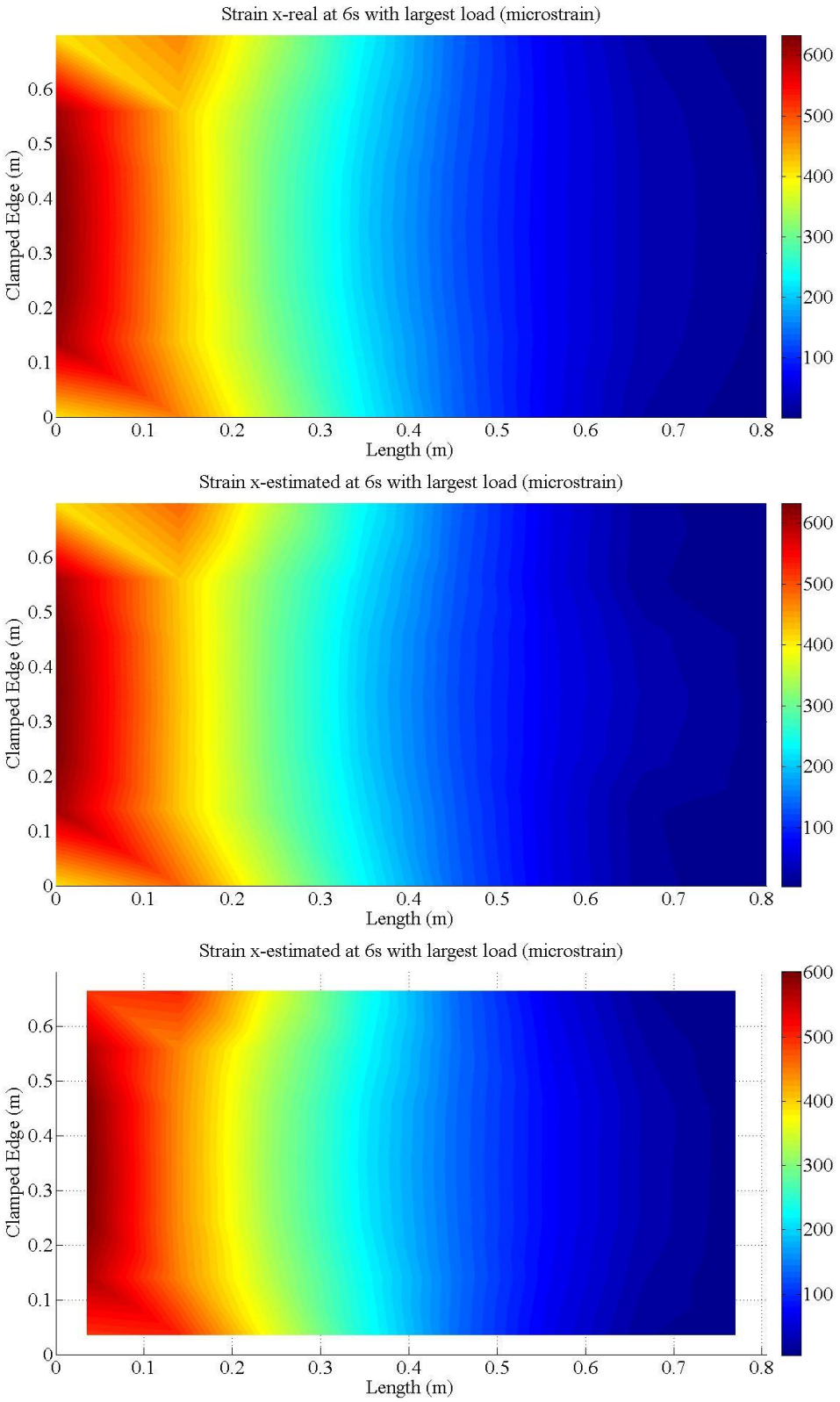

Figure 3.1: Contour plot of strain x estimated with LSE-polynomial algorithm under load case (a) at 6 s (top: analytical, middle: estimation with ideal BC enforcement, bottom: estimation with modeled BC enforcement)

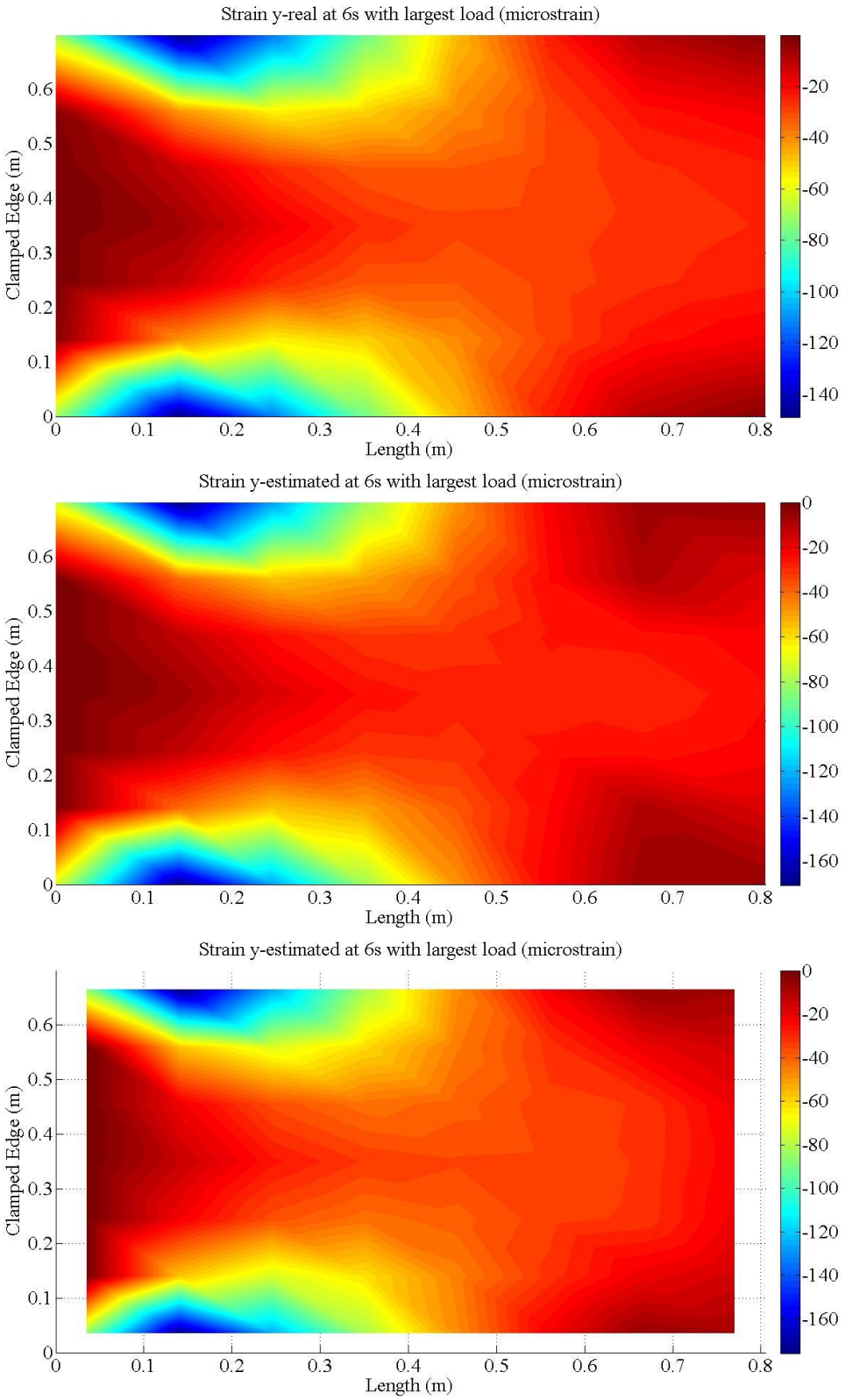

Figure 3.2: Contour plot of strain y estimated with LSE-polynomial algorithm under load case (a) at 6 s (top: analytical, middle: estimation with ideal BC enforcement, bottom: estimation with modeled BC enforcement)

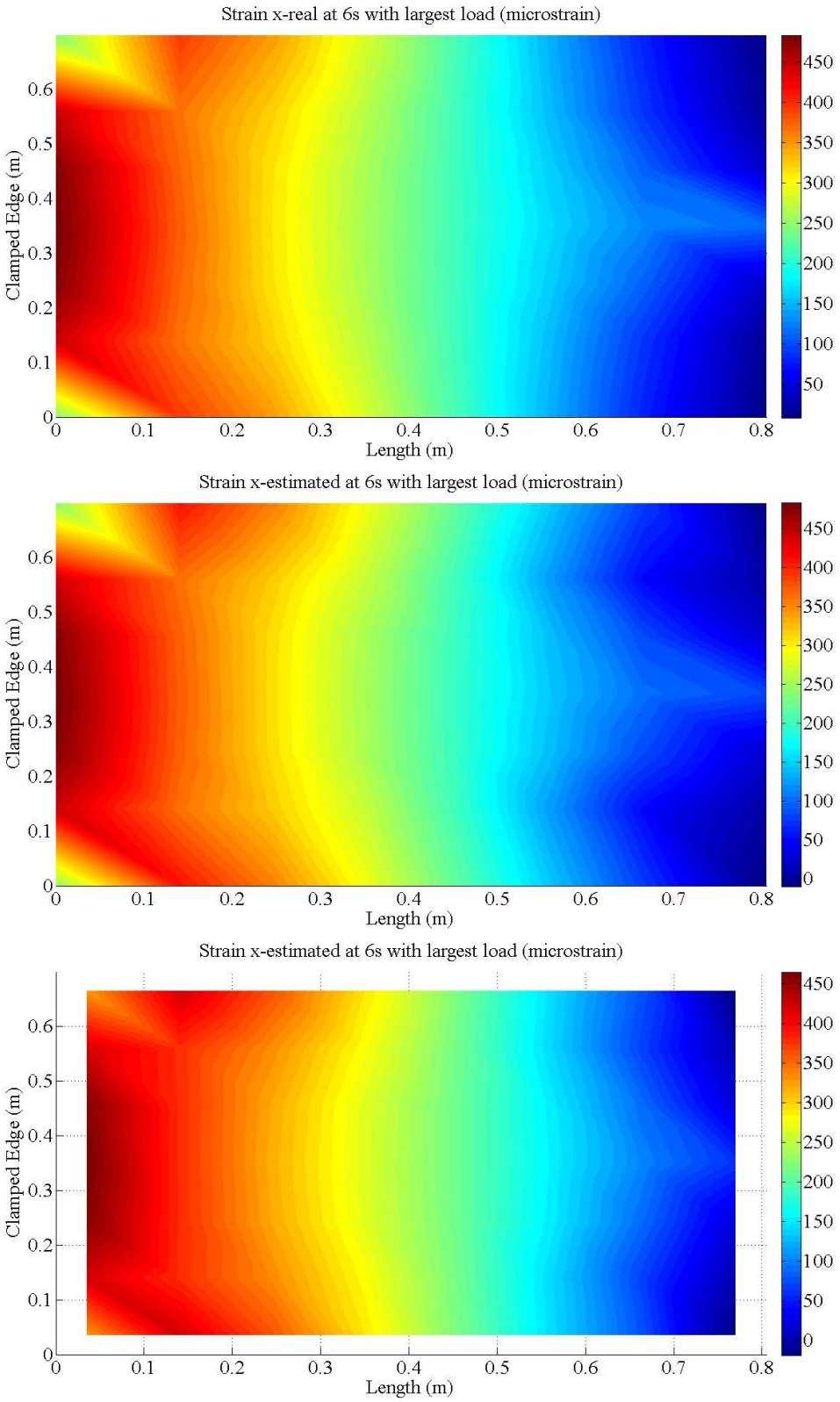

Figure 3.3: Contour plot of strain x estimated with LSE-polynomial algorithm under load case (b) at 6 s (top: analytical, middle: estimation with ideal BC enforcement, bottom: estimation with modeled BC enforcement)

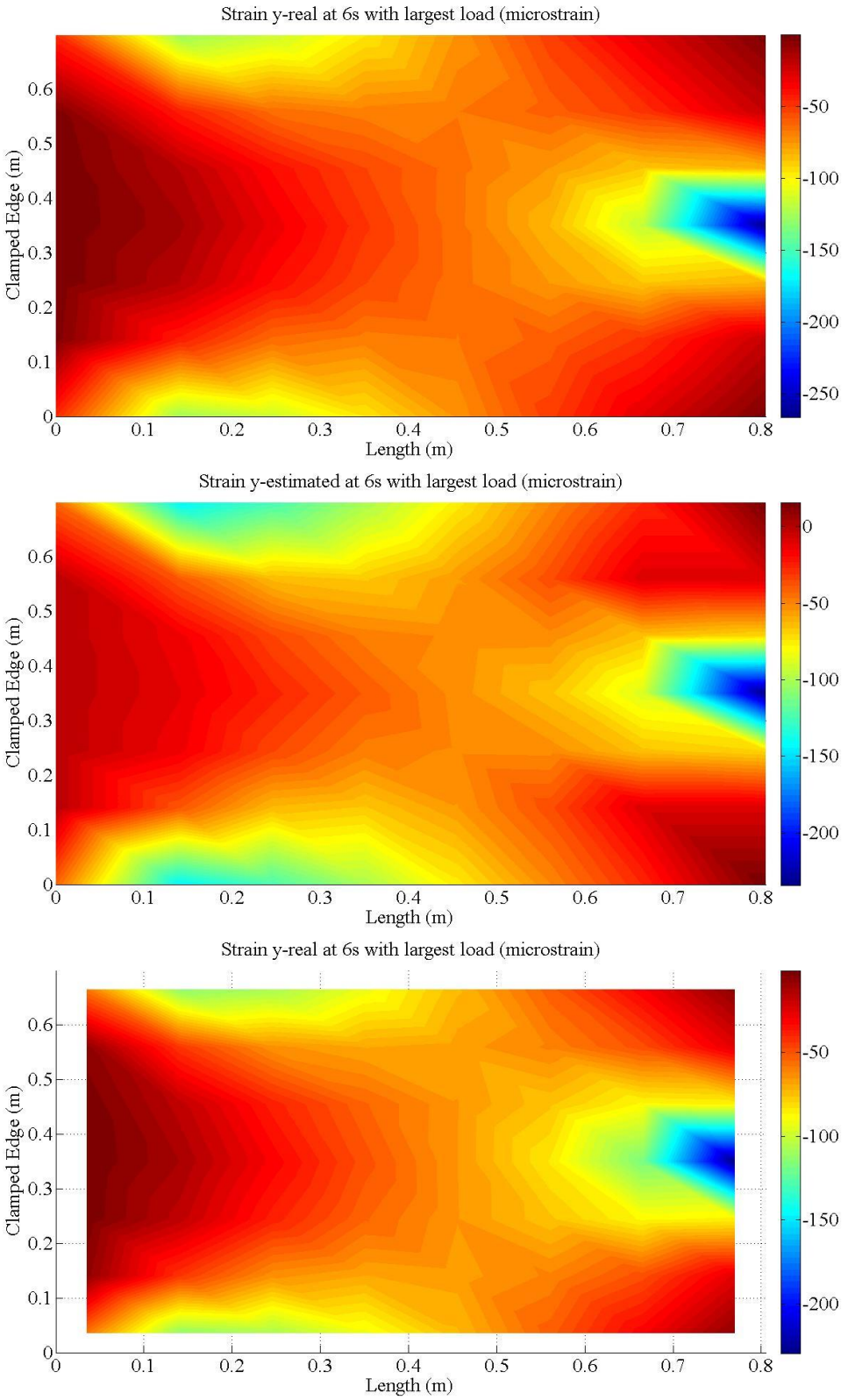

Figure 3.4: Contour plot of strain y estimated with LSE-polynomial algorithm under load case (b) at 6 s (top: analytical, middle: estimation with ideal BC enforcement, bottom: estimation with modeled BC enforcement)

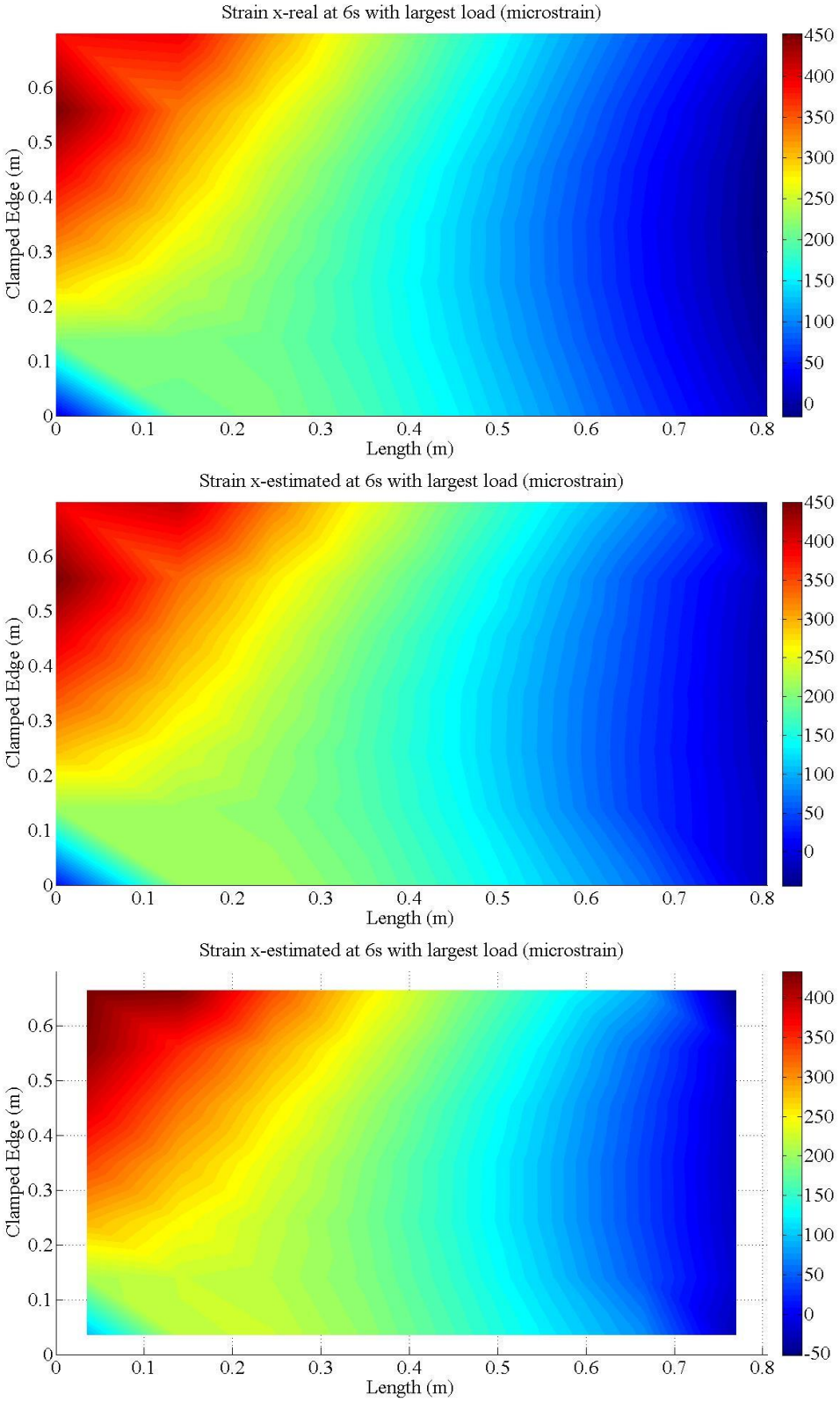

Figure 3.5: Contour plot of strain x estimated with LSE-polynomial algorithm under load case (c) at 6 s (top: analytical, middle: estimation with ideal BC enforcement, bottom: estimation with modeled BC enforcement)

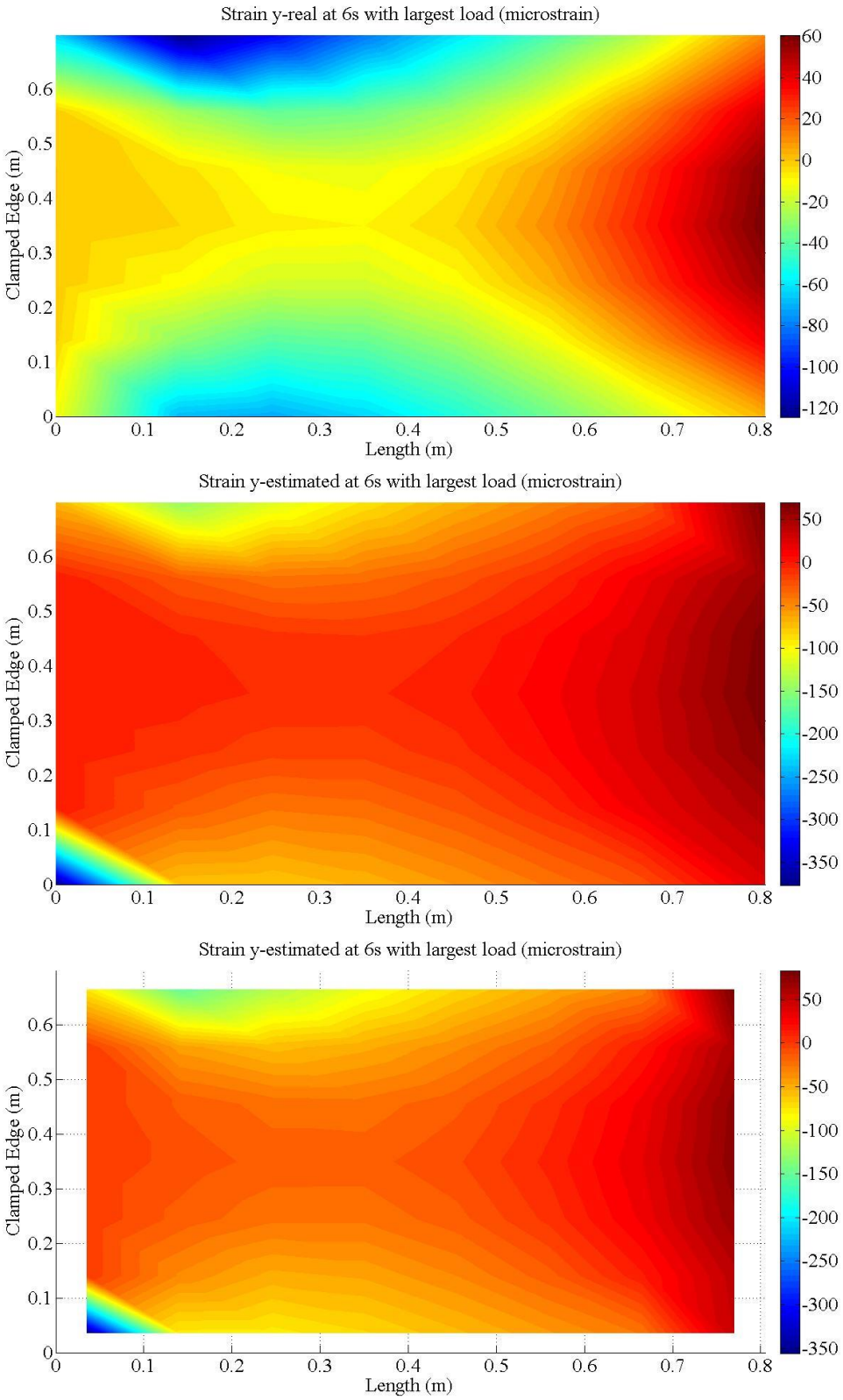

Figure 3.6: Contour plot of strain y estimated with LSE-polynomial algorithm under load case (c) at 6 s (top: analytical, middle: estimation with ideal BC enforcement, bottom: estimation with modeled BC enforcement)

3.1.2 Effect of the modeled BC enforcement on the LSE-biharmonic algorithm

The LSE-biharmonic formulation already showed the capability to decompose the SEC signal into biaxial strain with the ideal BC enforcement in the previous chapter by investigating its global MAPE over time and local MAPE on the plate surface within the plate boundary. This section will look into how the defect introduced to the algorithm by the shift from the ideal BC enforcement to the modeled BC enforcement will affect the performance of the LSE-biharmonic formulation through direct comparison on strain field contour plot when the load reaches the largest magnitude and the total MAPE and SD of PE of the results for different BC enforcement condition under all load cases. Figs. 3.7 – 3.12 clearly suggests that the performance of the LSE-biharmonic algorithm becomes obviously poorer with modeled BC enforcement instead of ideal BC enforcement, but it is still able to capture the variation of biaxial strain field on the plate surface. The biharmonic formula is based on the superposition of periodic mode shape functions. As a result, the improper shift in BC may lead to difficulties in matching period and phase angle after superposition with limited expansion of the finite integral transform representing limited mode shapes. This explains the severe decline in estimation accuracy of the LSE-biharmonic formulation compared when the BC is not applied on the exact location, which is not the case for LSE-polynomial formulation (Figs. 3.1 – 3.6). The possibility to resolve this problem with the LSE-biharmonic formulation by extend the expansion of the finite integral transform to include more mode shapes will be investigated in the following section.

Additionally, the estimation quality turns to drop more for strain y than for strain x and under load case (c) than under the other two load cases when the BC enforcement shifts from ideal to modeled condition. This can also be explained by the higher sensitivity in

percentage error for smaller values and the abrupt change in strain field on the geometry base respectively as discussed before. By comparing Table 3.2 with Table 3.1, it is also confirmed that the LSE-biharmonic formulation with current expansion is more sensitive to the imperfection in BC enforcement compared with the LSE-polynomial formulation with current order.

Table 3.2: Performance of the LSE-biharmonic algorithm under differente BC enforcements

Load case	Evaluation item	Strain estimation direction	Ideal BC enforcement	Modeled BC enforcement
(a)	MAPE (%)	x	6.39	66.38
		y	30.74	214.92
	SD of PE (%)	x	8.10	80.70
		y	40.54	136.14
(b)	MAPE (%)	x	10.41	22.47
		y	27.51	87.54
	SD of PE (%)	x	15.43	24.18
		y	33.55	82.79
(c)	MAPE (%)	x	23.94	49.25
		y	207.19	433.43
	SD of PE (%)	x	31.32	53.18
		y	294.30	555.14

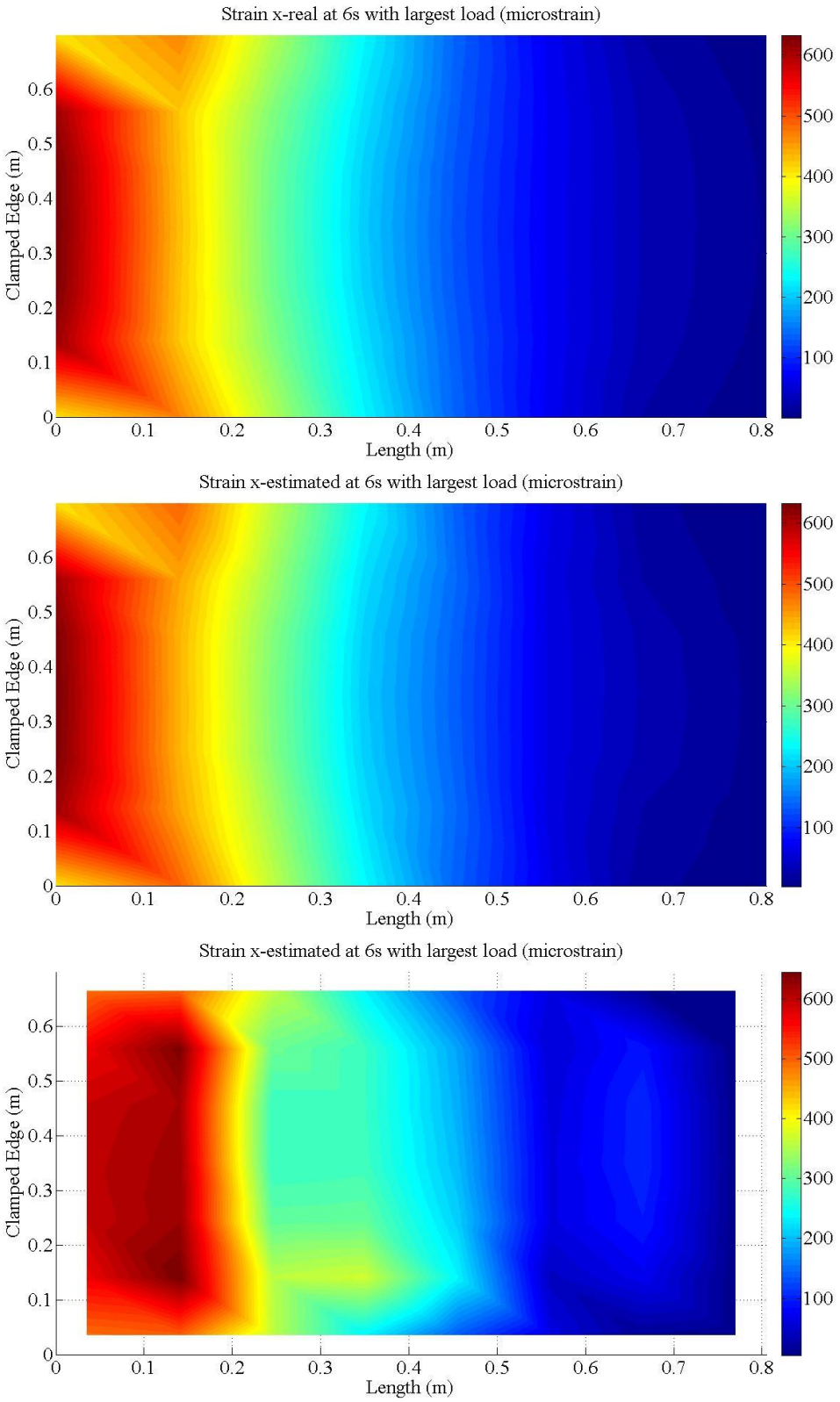

Figure 3.7: Contour plot of strain x estimated with LSE-biharmonic algorithm under load case (a) at 6 s (top: analytical, middle: estimation with ideal BC enforcement, bottom: estimation with modeled BC enforcement)

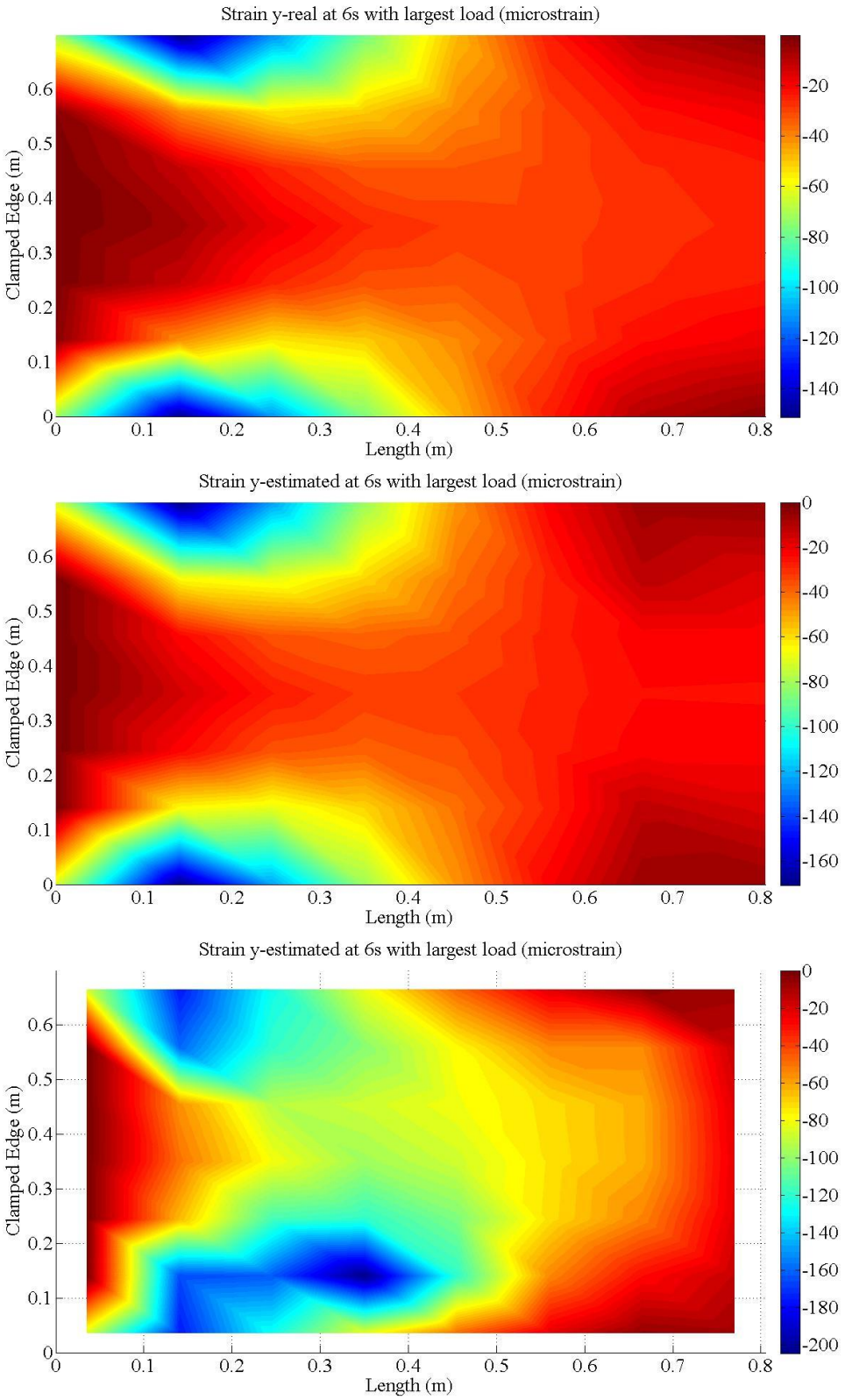

Figure 3.8: Contour plot of strain y estimated with LSE-biharmonic algorithm under load case (a) at 6 s (top: analytical, middle: estimation with ideal BC enforcement, bottom: estimation with modeled BC enforcement)

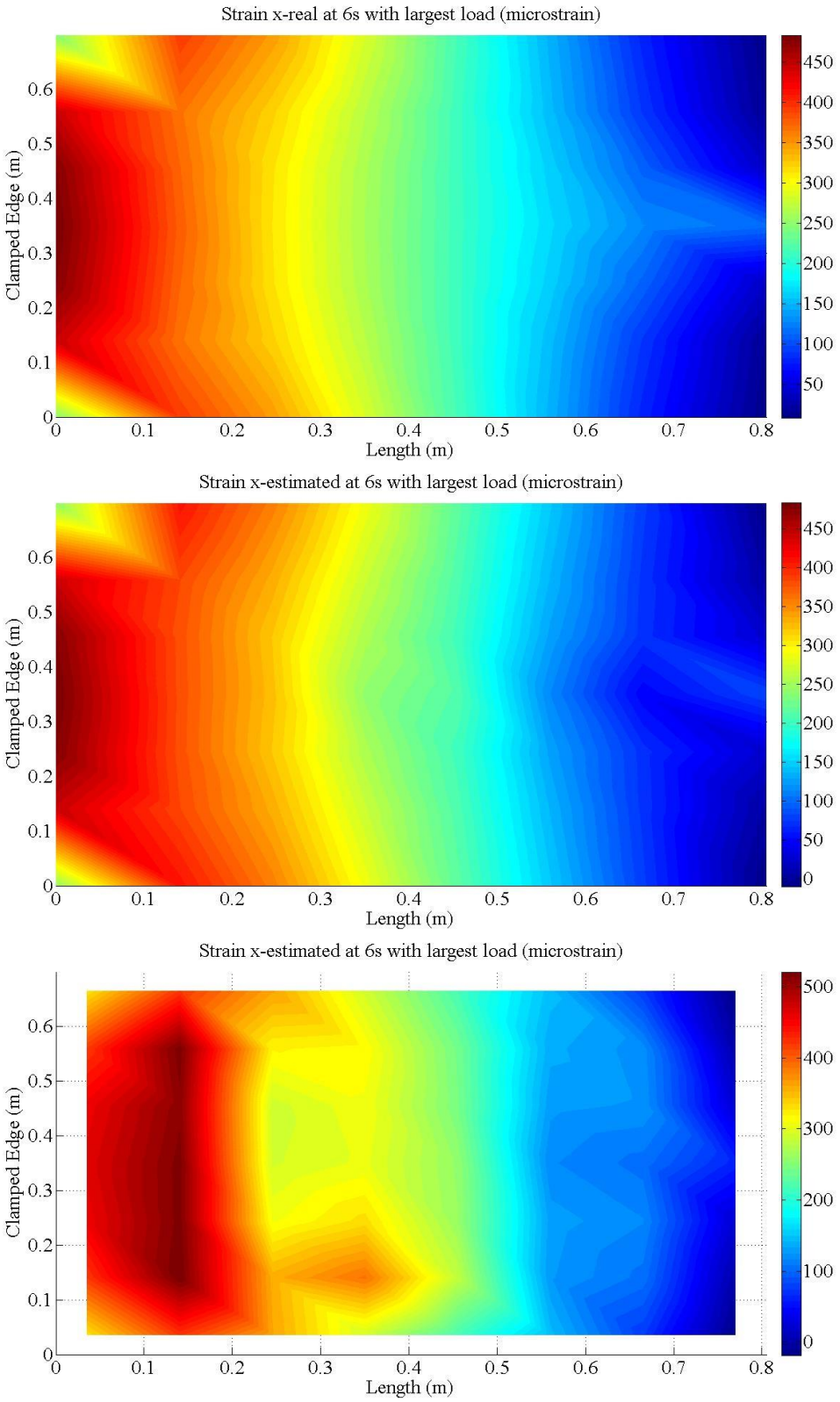

Figure 3.9: Contour plot of strain x estimated with LSE-biharmonic algorithm under load case (b) at 6 s (top: analytical, middle: estimation with ideal BC enforcement, bottom: estimation with modeled BC enforcement)

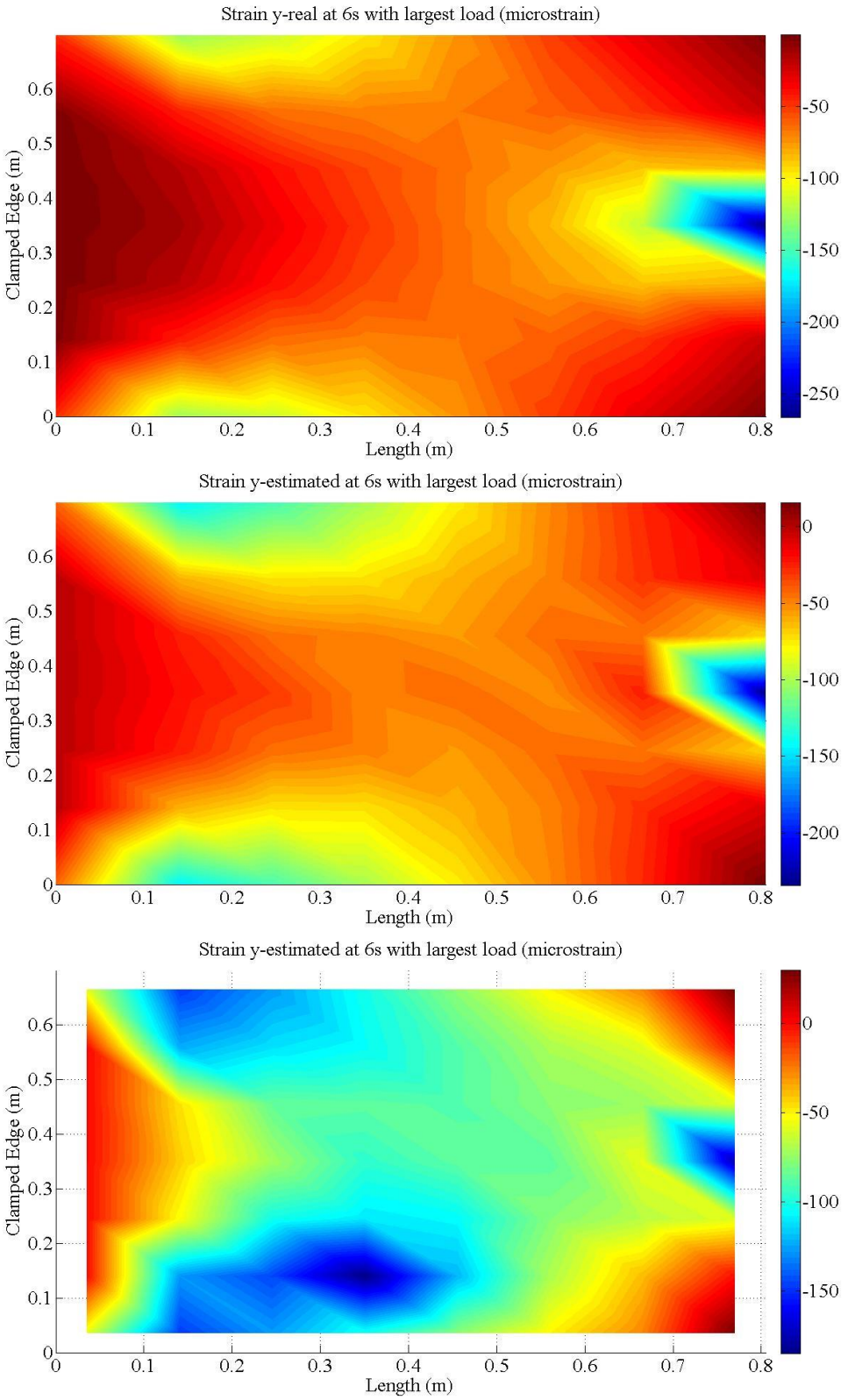

Figure 3.10: Contour plot of strain y estimated with LSE-biharmonic algorithm under load case (b) at 6 s (top: analytical, middle: estimation with ideal BC enforcement, bottom: estimation with modeled BC enforcement)

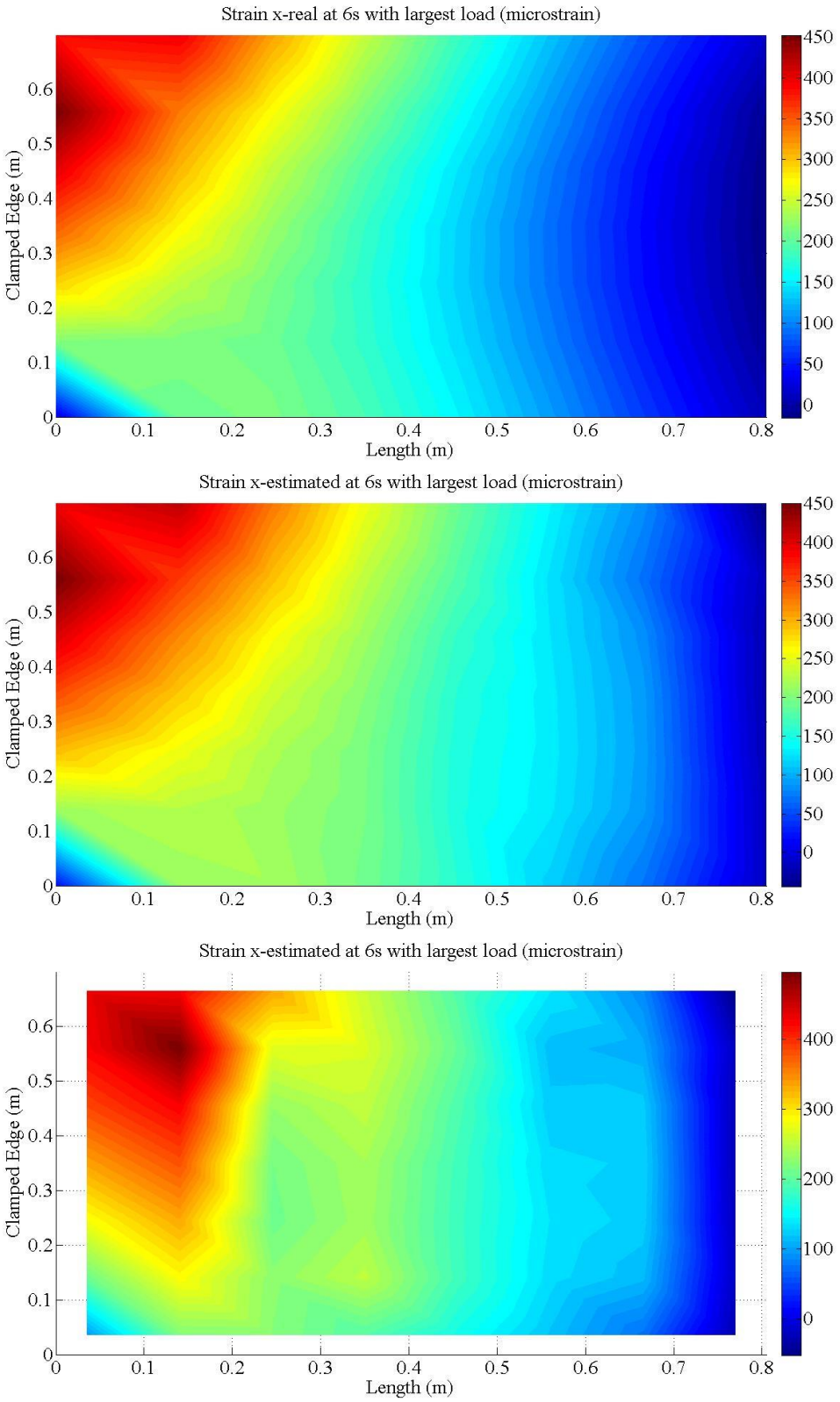

Figure 3.11: Contour plot of strain x estimated with LSE-biharmonic algorithm under load case (c) at 6 s (top: analytical, middle: estimation with ideal BC enforcement, bottom: estimation with modeled BC enforcement)

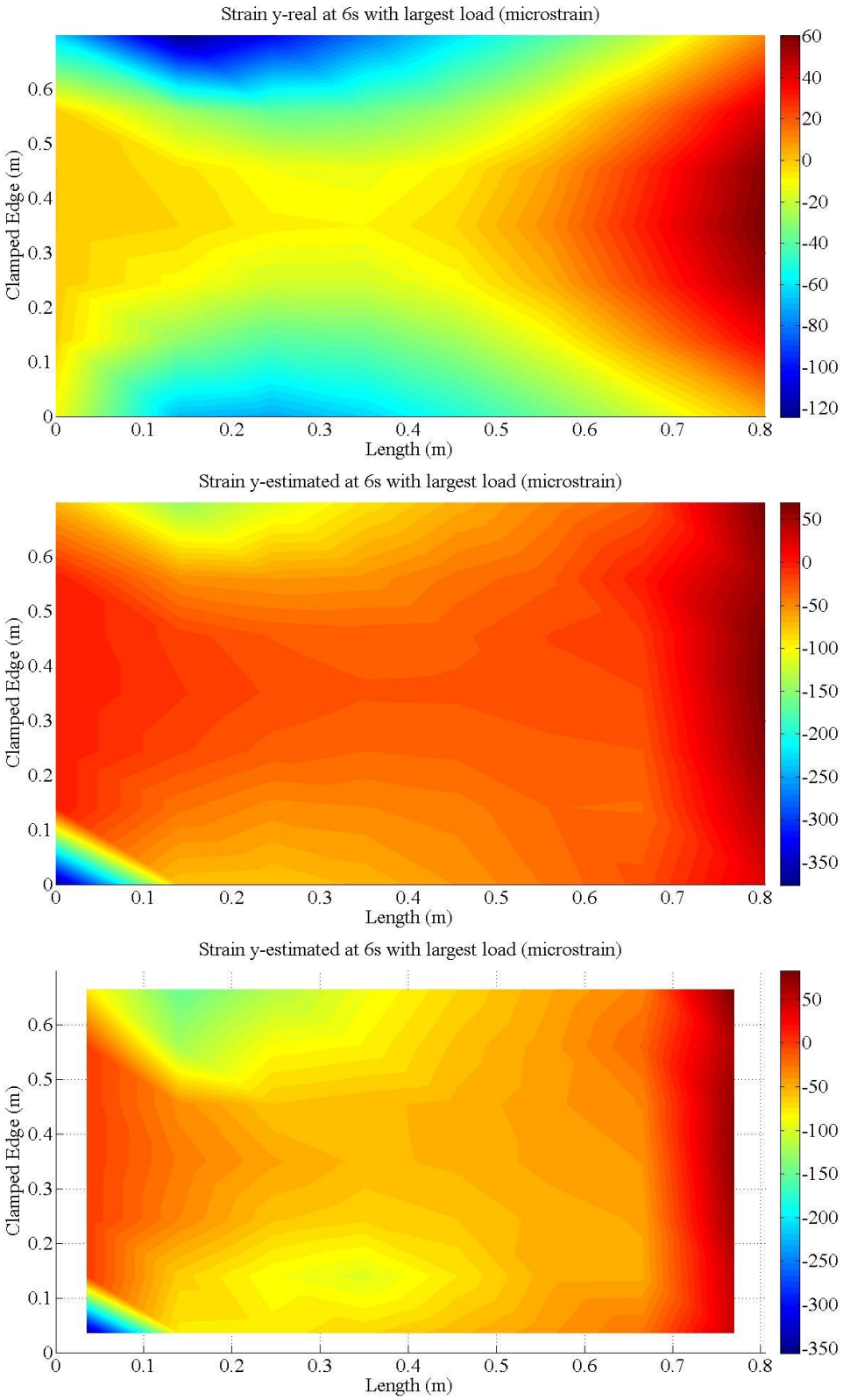

Figure 3.12: Contour plot of strain y estimated with LSE-biharmonic algorithm under load case (c) at 6 s (top: analytical, middle: estimation with ideal BC enforcement, bottom: estimation with modeled BC enforcement)

3.2 Evaluation of Algorithm Formulations under the Influence of Order/Expansion of Function

The previous section talked about the performance of both algorithm formulas with the modeled BC enforcement and proposed the possibility to improve the estimation accuracy with modeled boundary sensor nodes by increasing the order for the polynomial formulation and extending the expansion for the biharmonic formulation. Such possibility will be studied in this section. In chapter 2, Both the polynomial and the biharmonic formulation are in their highest possible order or longest possible expansion with the SEC amount shown in Fig. 2.1. Since the SEC is highly customizable in size and geometry, the number of the sensor nodes are increased and rearranged in a finer mesh by changing the current available SEC size (7 × 7 cm each) into a smaller size (5 × 5 cm each) (Fig. 3.13).

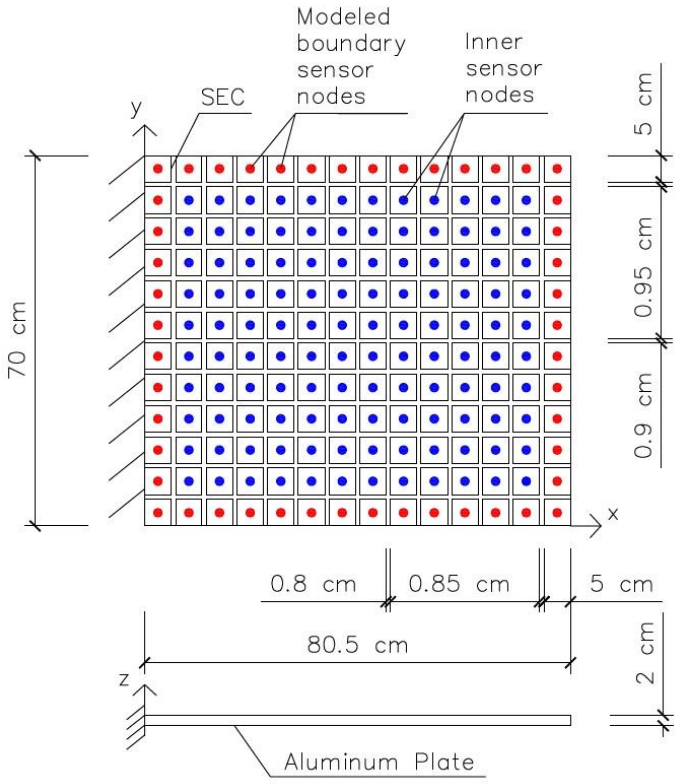

Figure 3.13: Test plate and finer matrix SEC configuration

The comparison was conducted between lower and higher order functions for the polynomial formulation and shorter and longer expansion for the biharmonic formulation, all under the same sensor amount shown in Fig. 3.13. The LSE-polynomial formula was investigated from quadratic to the highest possible order. Likewise, the expansion of the LSE-biharmonic formula was tested from 3 terms for both direction (considering the first three mode shapes in each direction) to the most reachable number of terms. The results can be compared with Figs. 3.14 – 16 and Table 3.3 – 3.4. With the increased sensor amount shown in Fig. 3.13, the LSE-biharmonic formulation was able to be expanded to 11 terms for m and n (Eq. 2.6) while the LSE-polynomial formulation was still only able to have the order of 6 as that with the less sensor amount before (Fig. 2.1). It is probably because of the geometry related α_m and β_n in the biharmonic formula (Eq. 2.6) reduce the dependence of the vectors in the $\boldsymbol{H_s}$ matrix (Eq. 2.5) due to repeated x and y values from the matrix SEC arrangement. However, the performance of polynomial formulation is much better than the biharmonic one based on the overall MAPE of all non-boundary sensor nodes at all the time points under all three load cases shown in Fig. 3.14. The accuracy of the polynomial formulation is increased sharply from quadratic to the 4th order and relatively constant afterward, but it is still showing the higher accuracy with the higher order. Conversely, the biharmonic formulation did not show a clear decrease in the overall MAPE when the expansion has become longer but had a sudden jump of overall MAPE in the y direction of all load cases when expanded to 10 terms in both direction. Therefore, the polynomial formulation showed a more stable behavior.

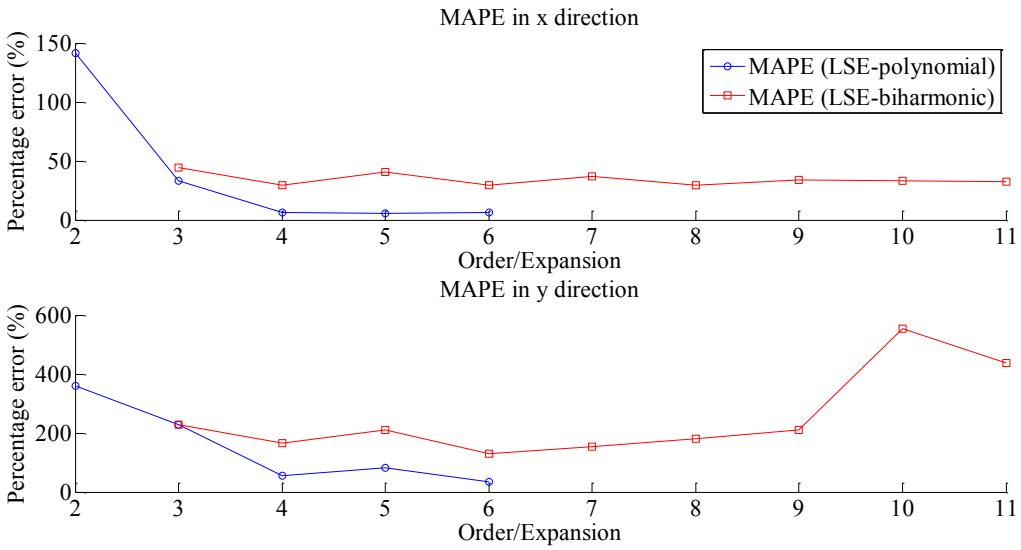

Figure 3.14: MAPE variation in biaxial directions versus order of LSE-polynomial and expansion of LSE-biharmonic formulation

For the biharmonic formulation, although the MAPE actually reduced obviously in the symmetric load cases (a) and (b) when the expansion became longer (Table 3.4, where expansion i means expand both m and n in Eq. 2.18 – 19 to i items), the jump of MAPE in the asymmetric load case (c) brought the overall MAPE to a much higher value in Fig. 3.14. Such jump in MAPE is probably suggesting an overfitting has occurred under the asymmetric load case (c). On the other hand, the decrease of MAPE under the two symmetric load cases demonstrated that the performance of the LSE-biharmonic formulation did become better with longer expansion of formula. However, the limitation of expansion length of the inverse finite integral transform (Eq. 2.6) to sufficiently represent the real integral transform due to the limited amount of sensor nodes and the overfitting problem under asymmetric loading condition (more realistic for practice) stopped the LSE-biharmonic formulation from achieving higher accuracy. Based on Fig. 3.14, the biharmonic formulation has a relatively better accuracy when expanded to 6 terms in both directions under the setup condition in Fig. 3.13.

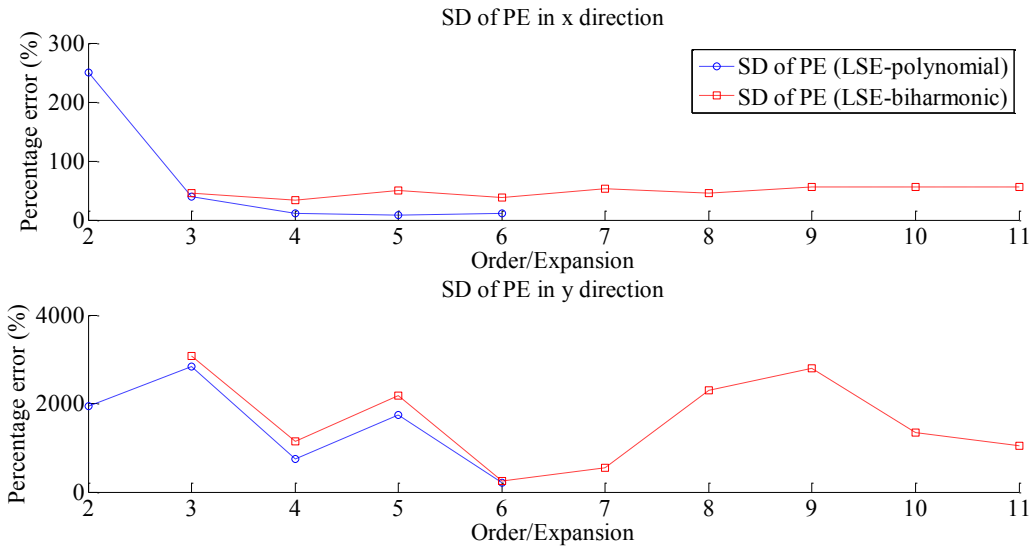

Figure 3.15: SD of PE variation in biaxial directions versus order of LSE-polynomial and expansion of LSE-biharmonic formulation

In addition, Figure 3.15 appears to suggest that both formulations behave relatively more stable with even instead of odd order/expansion for the given symmetric cantilever plate. Such pattern also can be seen when looking at each load case separately (Table 3.3 and 3.4) and it is more obvious for the biharmonic formulation. The reason of such phenomenon may be that the displacement variation over the symmetric plate surface fits the shape of the formulas with even order/expansion. Although the polynomial formulation with 5^{th} order showed the best accuracy under load case (b) (Table 3.3), 6^{th} order which is the highest order still showed the best estimation by considering all the load cases for the polynomial formulation.

Table 3.3: Performance of the LSE-polynomial algorithm with different orders of function

Load case	Evaluation item	Strain estimation direction	Order 2	Order 3	Order 4	Order 5	Order 6
(a)	MAPE (%)	x	264.61	69.42	4.72	6.86	6.39
		y	323.77	242.64	23.96	22.72	22.45
	SD of PE (%)	x	433.93	71.46	8.25	10.38	10.20
		y	435.22	217.88	40.50	21.26	34.13
(b)	MAPE (%)	x	56.56	11.89	5.36	3.66	6.03
		y	144.79	42.85	14.43	12.19	15.55
	SD of PE (%)	x	100.36	18.04	9.12	6.74	9.18
		y	197.84	52.78	21.15	14.84	21.16
(c)	MAPE (%)	x	103.33	18.84	8.47	5.61	6.93
		y	606.59	399.69	127.15	207.94	60.62
	SD of PE (%)	x	214.34	30.09	16.29	9.21	14.79
		y	5210.40	8225.00	2191.40	5212.30	586.86

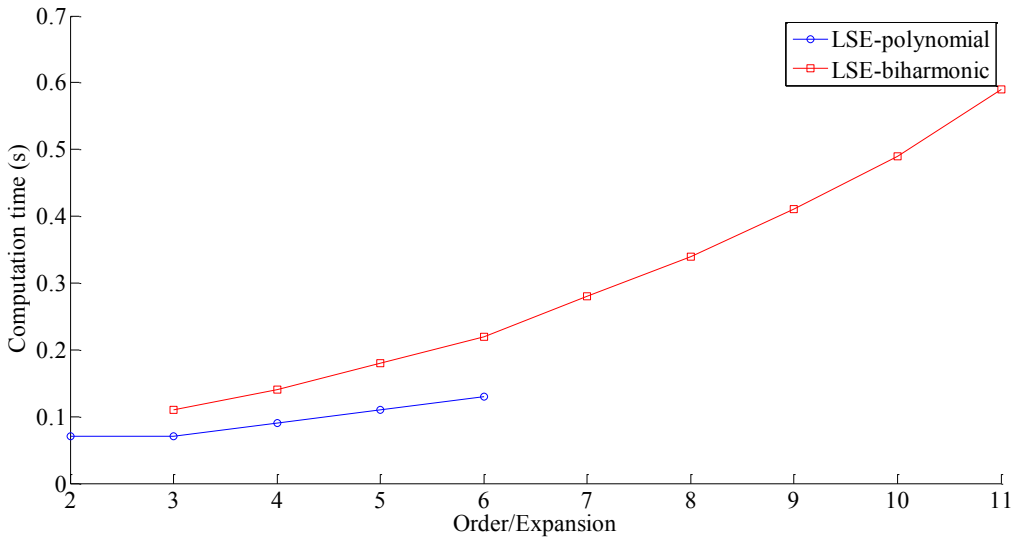

Figure 3.16: Computation time of LSE-polynomial and LSE-biharmonic formulation with different order/expansion

The computation time of both algorithm formulations is also of interest. Under the SEC configuration showing in Fig. 3.13, the computation time was investigated using

MATLAB R2012b on a computer with 2.50 GHz CPU. As it shows in Fig. 3.16, the LSE algorithm with the polynomial formulation is over 1.5 times faster than that with biharmonic formulation under the same order/expansion. The cause of such result could be the complexity of the inverse finite integral transform. Also, the execution time of the LSE-biharmonic formulation grows more rapidly when the formula becomes much more complex compared to that of the LSE-polynomial formulation. Overall, the LSE-polynomial requires around 0.13 s to process the data from the amount of SECs (168 SECs) set in Fig. 3.13 at the highest achievable accuracy. Therefore, the proposed algorithm is sufficient for real-time SHM, especially considering the amount of SEC could be less in practice by having a more efficient sensor placement strategy for specific geometry and expected loading condition.

Table 3.4: Performance of the LSE-biharmonic algorithm with different lengths of expansion of function

Load case	Evaluation item	Strain estimation direction	Expension 3	Expension 4	Expension 5	Expension 6	Expension 7	Expension 8	Expension 9	Expension 10	Expension 11
(a)	MAPE (%)	x	61.81	37.91	62.13	36.99	55.24	33.37	47.61	35.04	38.85
		y	116.37	111.87	124.09	107.56	119.10	94.93	108.25	86.35	63.17
	SD of PE (%)	x	68.57	47.49	82.89	49.28	89.90	49.59	89.29	52.58	72.29
		y	47.60	110.63	129.65	136.81	139.09	165.55	157.29	93.30	86.83
(b)	MAPE (%)	x	40.68	27.23	36.85	25.89	34.63	23.06	29.78	15.03	19.12
		y	108.98	104.57	109.74	97.34	102.53	78.48	83.76	41.39	38.01
	SD of PE (%)	x	34.76	22.51	35.32	23.15	35.93	24.11	35.32	21.30	29.18
		y	31.09	48.84	63.35	68.54	68.60	81.67	78.94	52.85	49.18
(c)	MAPE (%)	x	29.80	23.32	23.04	26.00	20.71	32.56	24.16	49.07	39.81
		y	458.44	279.26	399.32	187.61	238.36	367.80	440.39	1532.60	1211.40
	SD of PE (%)	x	32.22	29.06	31.38	40.60	33.59	61.31	42.44	92.72	68.26
		y	9164.20	3296.30	6325.60	557.65	1423.30	6669.50	8175.50	3898.30	2974.20

3.3 Evaluation of Algorithm Formulations under the Influence of Noise

In previous sections, the proposed algorithm was only tested with the input from analytical signals without any noise. This section will look into the influence of the noise in signal. To consider a realistic noise condition of signal in practice, 2%, 5% and 10% random noises were introduced to the analytical SEC signals under different load cases respectively. The order of the polynomial formulation was 6 and the biharmonic formulation was expanded to 6 items in each direction for investigation.

Table 3.5: Performance of the LSE-polynomial algorithm with different noise condition

Load case	Evaluation item	Strain estimation direction	Noise (0%)	Noise (2%)	Noise (5%)	Noise (10%)
(a)	MAPE (%)	x	6.39	6.72	7.34	10.54
		y	22.45	23.23	23.78	31.11
	SD of PE (%)	x	10.20	10.96	12.18	17.52
		y	34.13	36.80	42.06	57.22
(b)	MAPE (%)	x	6.03	6.17	7.03	8.82
		y	15.55	15.69	17.41	21.44
	SD of PE (%)	x	9.18	9.22	9.91	11.97
		y	21.16	21.66	25.30	32.22
(c)	MAPE (%)	x	6.93	6.89	7.68	10.03
		y	60.62	68.43	81.51	104.11
	SD of PE (%)	x	14.79	14.61	15.41	18.14
		y	586.86	756.68	780.34	991.68

The results of the LSE algorithm with both polynomial and biharmonic formulation are summarized in Table 3.5 and 3.6. It can be seen that the existence of noise affect the accuracy in the minor direction y and in load case (c) relatively more than in x direction and in other two load cases. It is probably because imperfection of BC enforcement is the largest in load case (c) due to the combination of corner singularity and stress concentration at the

corner where the load locates and the noise amplified such imperfection. Overall, except for the level of 10% noise, there is only a small influence on the performance of both formulations, which demonstrated the ability of the proposed algorithm to maintain a relatively stable performance under noisy condition up to 5 % noise.

Table 3.6: Performance of the LSE-biharmonic algorithm with different noise condition

Load case	Evaluation item	Strain estimation direction	Noise (0%)	Noise (2%)	Noise (5%)	Noise (10%)
(a)	MAPE (%)	x	36.99	37.06	37.25	38.10
		y	107.56	107.73	108.08	111.61
	SD of PE (%)	x	49.28	49.34	49.41	50.34
		y	136.81	137.21	139.30	154.72
(b)	MAPE (%)	x	25.89	25.90	25.95	26.18
		y	97.34	97.34	97.88	99.22
	SD of PE (%)	x	23.15	23.16	23.26	23.54
		y	68.54	68.80	70.14	76.60
(c)	MAPE (%)	x	26.00	26.01	26.24	26.85
		y	187.61	192.60	197.98	240.67
	SD of PE (%)	x	40.60	40.67	40.85	41.50
		y	557.65	732.52	807.81	1913.80

3.4 Conclusion

This section discussed the influence of the modeled BC enforcement, formula constitution and noise in SEC signal for the proposed LSE algorithm with polynomial and biharmonic formulation by looking at their MAPE, SD of PE and execution time. The LSE-polynomial formulation showed lower sensitivity to the imperfection of BC enforcement, higher accuracy with highest reachable order in formula and faster data process speed than the LSE-biharmonic. The conclusion can be drawn that the polynomial formulation is the better option for the proposed LSE algorithm.

CHAPTER 4

INVESTIGATION ON POTENTIAL APLICATION OF LSE-POLYNOMIAL ALGORITHM ON WIND TURBINE BLADE

It has been determined in Chapter 3 that the polynomial formulation performs best for the proposed LSE algorithm. In this chapter, the potential for wind turbine blade monitoring of the LSE-polynomial algorithm will be studied by simulating the algorithm on a cantilever plate with an irregular geometry and laminated sections with orthotropic materials resembling a wind turbine blade.

4.1 Simulation of Laminated Plate with Asymmetric Geometry

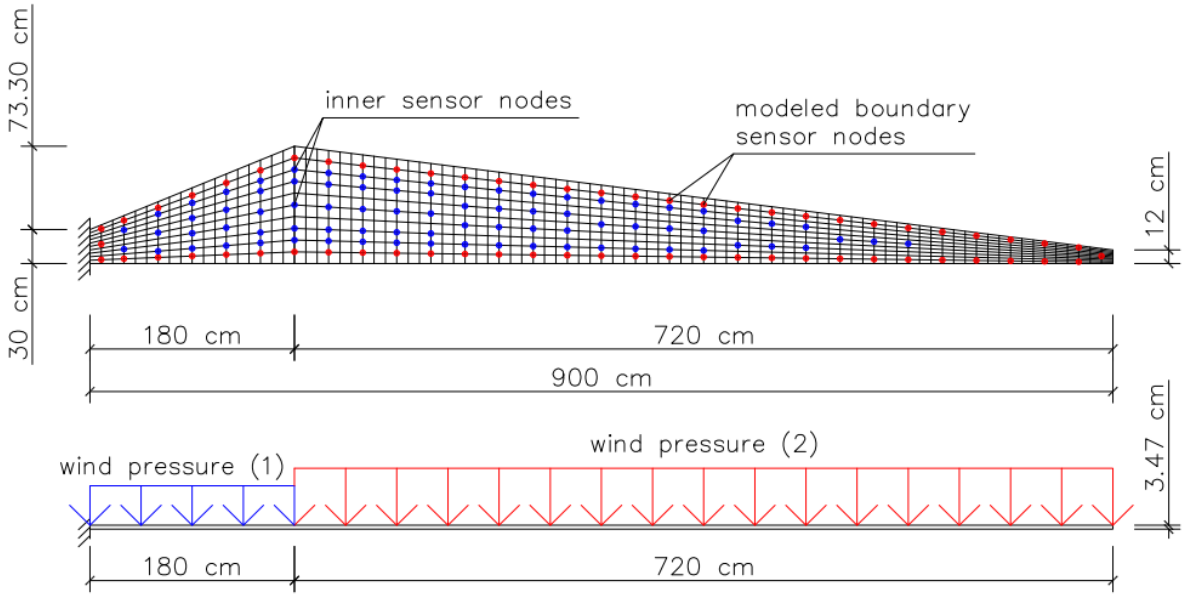

Figure 4.1: Blade resembling plate and SEC arranged in a network configuration

Based on the geometry and material of a 9-meter carbon-fiberglass prototype blade [34], a simplified blade resembling laminated plate with asymmetric geometry was designed with the root side fixed and the SEC arrangement (a network configuration) is shown in Fig.

4.1. The red nodes denoted as the modeled boundary sensor nodes were used for a practical BC enforcement and the blue nodes represents the inner sensor. Because of the limitation of geometry, only 3 and 1 SECs can be placed for the fixed root and free tip. Based on the 9-meter carbon-fiberglass prototype blade, the section of the plate was laminated and consisted of 11 layers of 7 different orthortropic materials stacked in various angles shown in Table 4.1. All the orthotropic materials were assumed to be transversely isotropic. For the finite element analysis, a four node shell element was used for the consideration of the bending dominated behavior of a real wind turbine blade and shear deformation ignored. The SEC signals were constructed using the finite element model and with 2% noise. To evaluate the performance of the LSE-polynomial algorithm under more realistic condition for a wind turbine blade, two sets of time varying wind pressure were simulated and applied on two different sections of the blade surface as shown in Fig. 4.1. The simulation of the wind pressure will be introduced in the following section.

Table 4.1: Materials and layers of the plate with asymmetric shape [34]

Layer No. (from 1 (bottom) to 11 (top))	Material	E_x (GPa)	E_y (GPa)	E_z (GPa)	G_{xy} (GPa)	G_{yz} (GPa)	G_{xz} (GPa)	ν_{xy}	ν_{yz}	ν_{xz}	Density (kg/m3)	Ply thickness (mm)
11	Gel coat	3.44	3.44	3.44	1.38	1.32	1.38	0.30	0.30	0.30	1230	0.26
10	Random mat	7.58	7.58	7.58	4.00	2.92	4.00	0.30	0.30	0.30	1687	0.76
9	End-grain balsa	0.12	0.12	0.12	0.02	0.05	0.02	0.30	0.30	0.30	230	12.80
7, 8	DBM1708(±45-deg fiberglass)	9.58	9.58	9.58	6.89	3.45	6.89	0.39	0.39	0.39	1814	0.89, 0.89
5, 6	DBM1208(±45-deg fiberglass)	9.58	9.58	9.58	6.89	3.45	6.89	0.39	0.39	0.39	1814	0.56, 0.56
4	C520 (0-deg fiberglass)	37.30	7.60	7.60	6.89	2.90	6.89	0.31	0.31	0.31	1874	9.20
3, 2, 1	Carbon-fiberglass triaxial fabric	84.10	8.76	8.76	4.38	3.62, 3.50, 3.62	4.38	0.21, 0.25, 0.21	0.21, 0.25, 0.21	0.21, 0.25, 0.21	3469	2.8, 3.2, 2.8

4.2 Wind Pressure Simulation [35]

A dual approach was selected for the wind load simulation. The simulated wind pressure was based on an input of real wind speed data sampled every 6 min at Station FTPC1 – 9414290 – San Francisco, CA. 18 hours of raw wind speed data were converted into one direction (northwest) and used as the input of the simulation (Fig. 4.2). The dual wind speed simulation can be divided into two major steps: (1) capturing the statistical characteristics of the real wind speed by smoothing the low frequency sampled raw wind speed time history data; (2) generating a high frequency turbulence spectrum to superimpose with the smoothed wind speed time history.

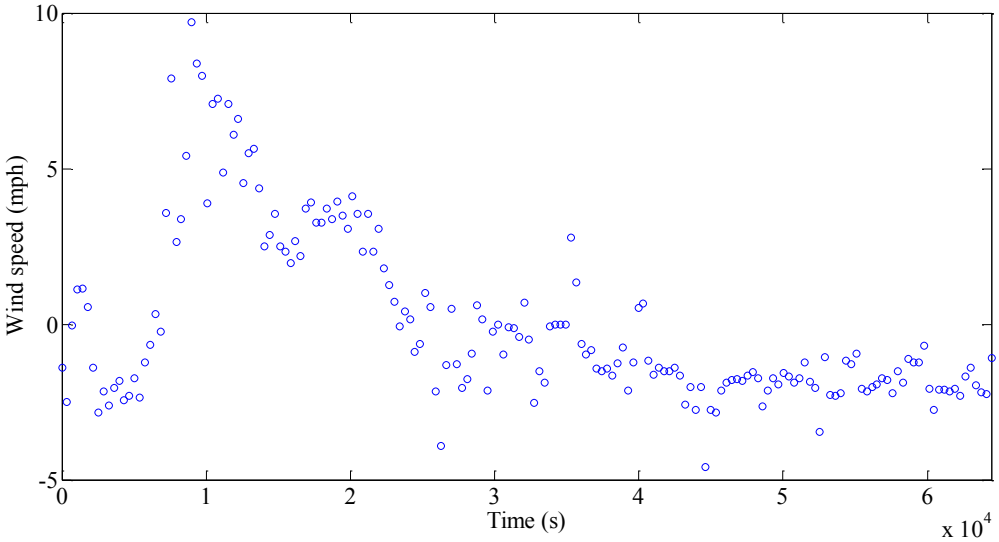

Figure 4.2: Real wind data sampled every 6 min [36]

For step (1): the hourly mean and variance were first taken from the raw wind speed data to extract its time varying statistical characteristics. Following, the hourly mean was resampled to the output frequency (10 Hz) based on the hourly mean value within each hour and a best fit line was fitted to the resampled data (Fig. 4.4). Based on the sampling theorem, only half of the input frequency can be resolved as the maximum frequency signal, which is

known as the Nyquist frequency [37]. Therefore, the resampling brought a set of frequencies higher than the Nyquist frequency which added noise to the wind time series. To rule out such high frequency noise introduced to the resampled wind speed time series, a third-order low-pass Butterworth filter was applied to the Fourier transform of the resampled wind time series in the frequency domain with a cutoff frequency of the Nyquist frequency. The wind time series was de-trended using the best fit line to avoid the wrap-around effects of the Fourier transform before transfer to the frequency domain. After the high frequency noise was filtered and filtered data was return from the frequency domain to the time domain using the inverse Fourier transform, the subtracted best fit line was added back to the filtered time series to produce a smoothed wind speed time series as shown in Fig 4.5.

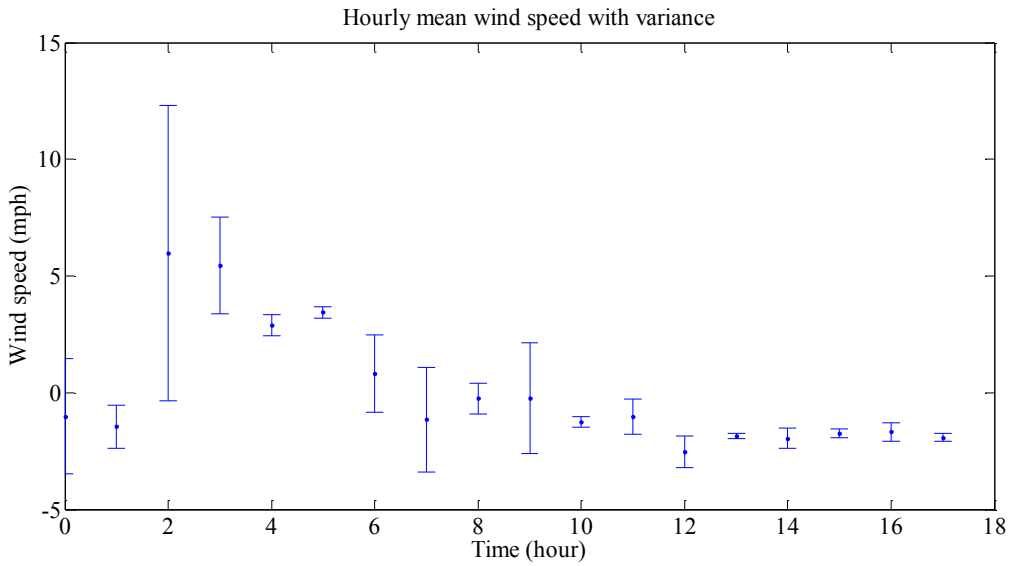

Figure 4.3: Hourly mean and variance of raw wind speed data

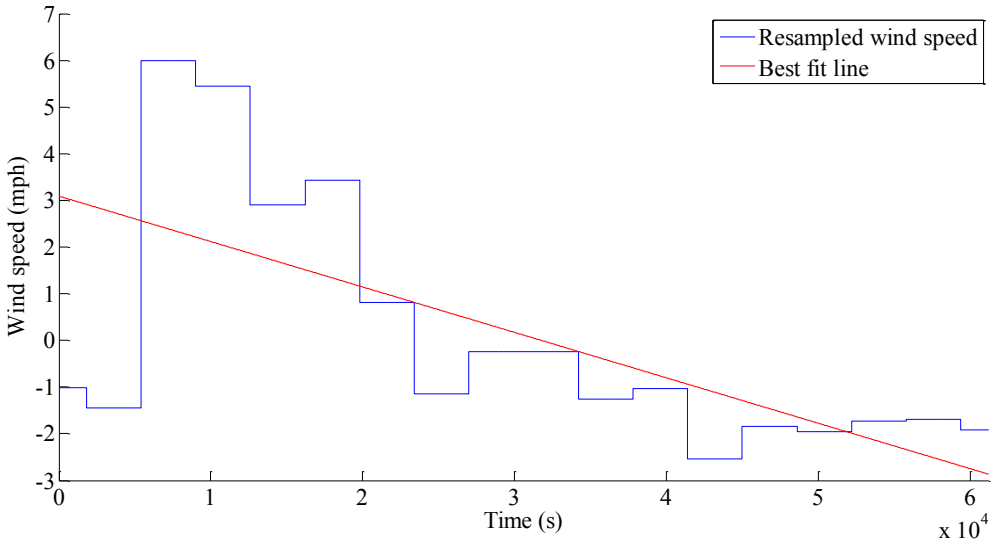

Figure 4.4: Resampled wind speed (10 Hz) and its best fit line

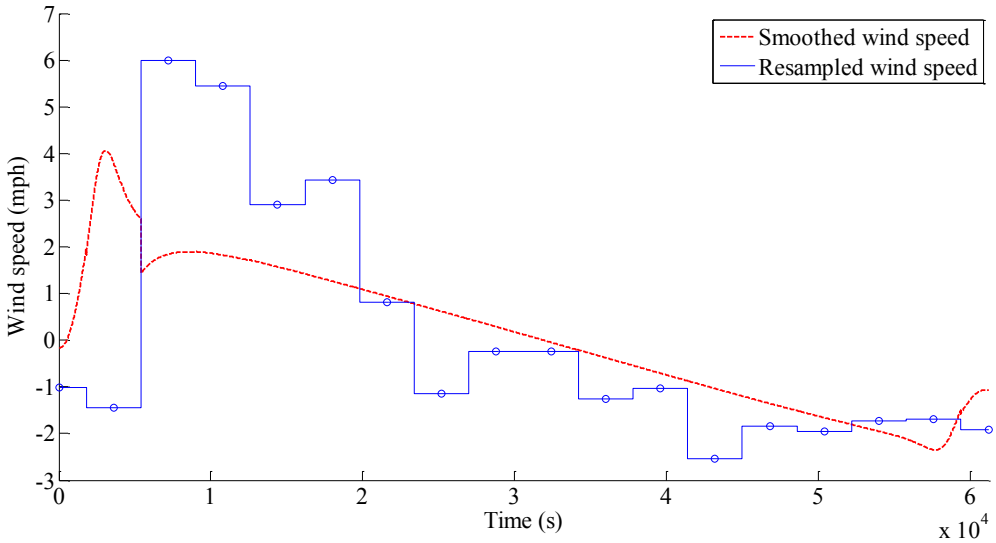

Figure 4.5: Resampled and Smoothed wind speed time series

For step (2): a zero-mean turbulence time series need to be introduced to the smoothed wind speed time series to reconstruct the non-stationary properties of real wind. A two-sided Kaimal spectrum at the height of 80 m was generated from the input of the hourly variance of the raw wind data following the IEC 61400-1 standard [38, 39] and based on the Shinozuka/Veers method [40, 41]. First, a one-side spectrum was defined as Eq. 4.1 (where

σ_u^2 is the hourly variance of the raw wind speed data, U_0 is the hourly mean of the raw wind speed data, L_i was taken as 340.2 for the turbulence at 80 m [35], f is the frequency input to the spectrum model) and then discretized to the output frequency f_{output} (10 Hz) for the whole duration T_{input} of the desired time series using Eq. 4.2 (where the discrete frequency is $f_m = m\Delta f$, $M = 1 + N/2$ and $N = 2T_{input}f_{output}$, note that M is an odd integer by definition so that N is an even integer, Δf was taken as one percent of the input frequency). By scaling and applying random phase angles to the discretized spectrum, a non-stationary one-sided spectrum was obtained with Eq. 4.3 (where the random phase angle was implemented by $e^{i\phi[m]}$ which is complex numbers, $\phi[m]$ was created by a uniform random distribution over the range [0, 2π] and the scaling factor η can be computed with Eq. 4.4 to compensate the loss of variance in the simulation). Then the two-sided spectrum can be generated using Eq. 4.5 (where $V^*[M-1], \dots, V^*[2]$ are the complex conjugate of $V[2], V[3], \dots, V[M-1]$ to represent the negative frequencies and $V_{2side}[1]$ is enforced to be zero to create a zero mean turbulence). At last, the turbulence time series can be obtained by applying the fast Fourier transform (FFT) to the two-sided spectrum (Eq. 4.6).

$$S(f) = \sigma_u^2 \frac{4\frac{L_i}{U_0}}{(1 + 6\frac{L_i}{U_0}f)^{\frac{5}{3}}} \tag{4.1}$$

$$S[m] = S(f_m)\Delta f, \qquad m = \{0, 1, \dots, M-1\} \tag{4.2}$$

$$V[m] = \sqrt{\frac{1}{2}\eta S[m]}e^{i\phi[m]} \tag{4.3}$$

$$\eta = \frac{1}{\sum_{m=1}^{M} S[m]} \tag{4.4}$$

$$V_{2side} = [0, V[2], V[3], \dots, V[M-1], |V[M]|, V^*[M-1], \dots, V^*[2]] \tag{4.5}$$

$$u = |FFT(V_{2side})| \tag{4.6}$$

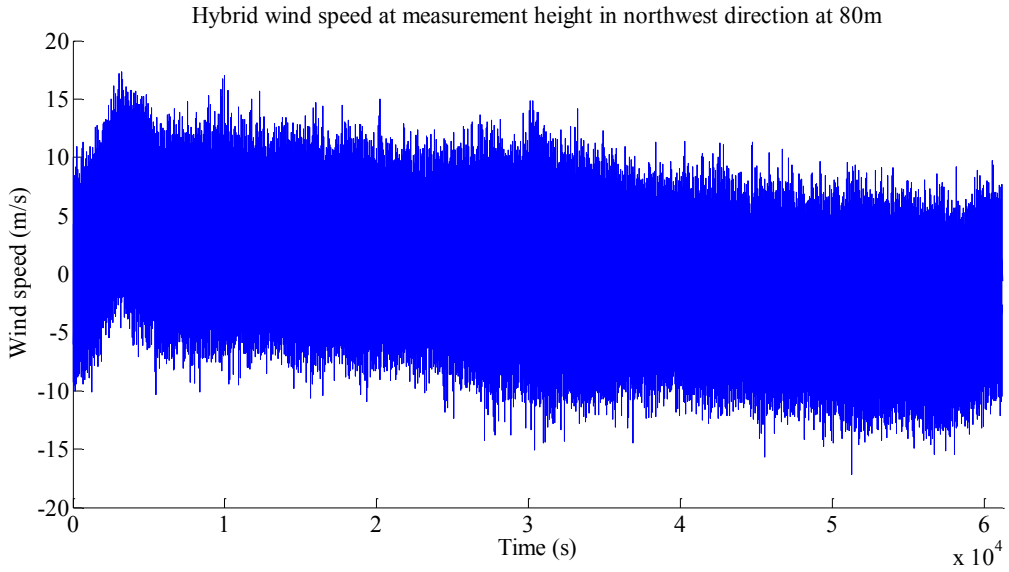

Figure 4.6: Simulated wind speed time series at 10 Hz

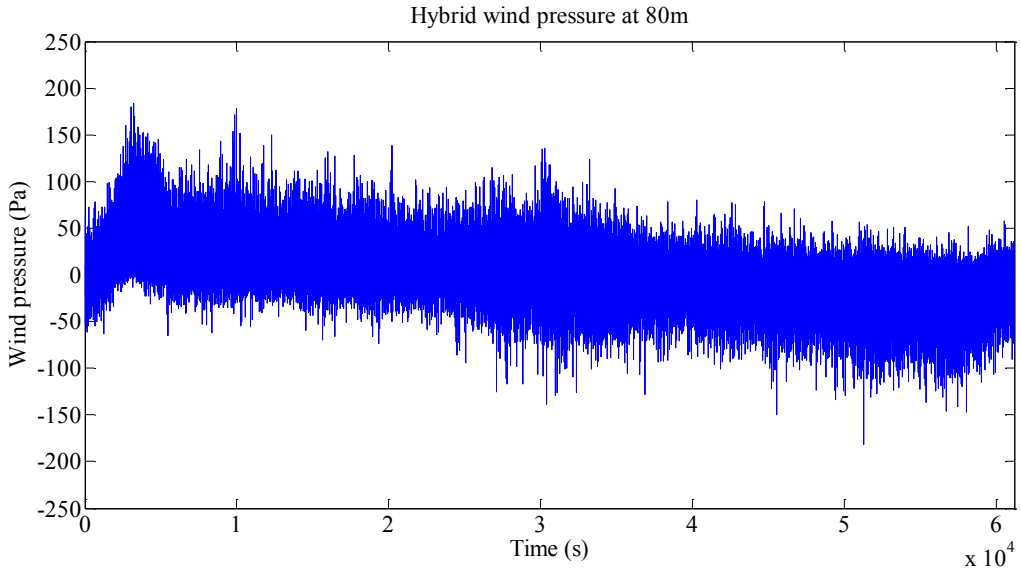

Figure 4.7: Simulated wind pressure time series at 10 Hz

After processing step (1) and (2), the dual wind speed can be generated by performing a superposition of the results from both steps (the smoothed wind speed time series and the simulated turbulence). Since the raw wind data is measured at 10 m above mean sea level

[36], the wind speed is relatively low. To obtain a general working wind speed for wind turbine between cut-in (typically between 3 – 4 m/s) and cut-out (usually around 25 m/s) wind speed, the generated wind speed was convert to that at a higher height (h = 80 m) using Eq. 4.7 (where v_{10} stands for the wind speed at 10 m, h_{10} is 10 m and a is the Hellman exponent which depends on the coastal location, shape of the terrain on ground and the stability of the air; a was taken as 0.6 for the assumption of stable air above human inhabited areas).

$$v_w(h) = v_{10} \cdot (\frac{h}{h_{10}})^a \tag{4.7}$$

$$P = 0.12257 {v_w}^2 \tag{4.8}$$

The resulting dual wind speed is given in Fig 4.6. According to Eq. 4.8, the wind pressure (in Pa) can then be constructed with the dual wind speed as shown in Fig. 4.8. The two sets of wind pressure time series (Fig. 4.8) of a duration of 10 s that are applied on the asymmetric plate (Fig. 4.1) were taken from two random parts of the simulated dual wind pressure and reduced from 10 Hz to 5 Hz for less load steps and computing time in the finite element analysis.

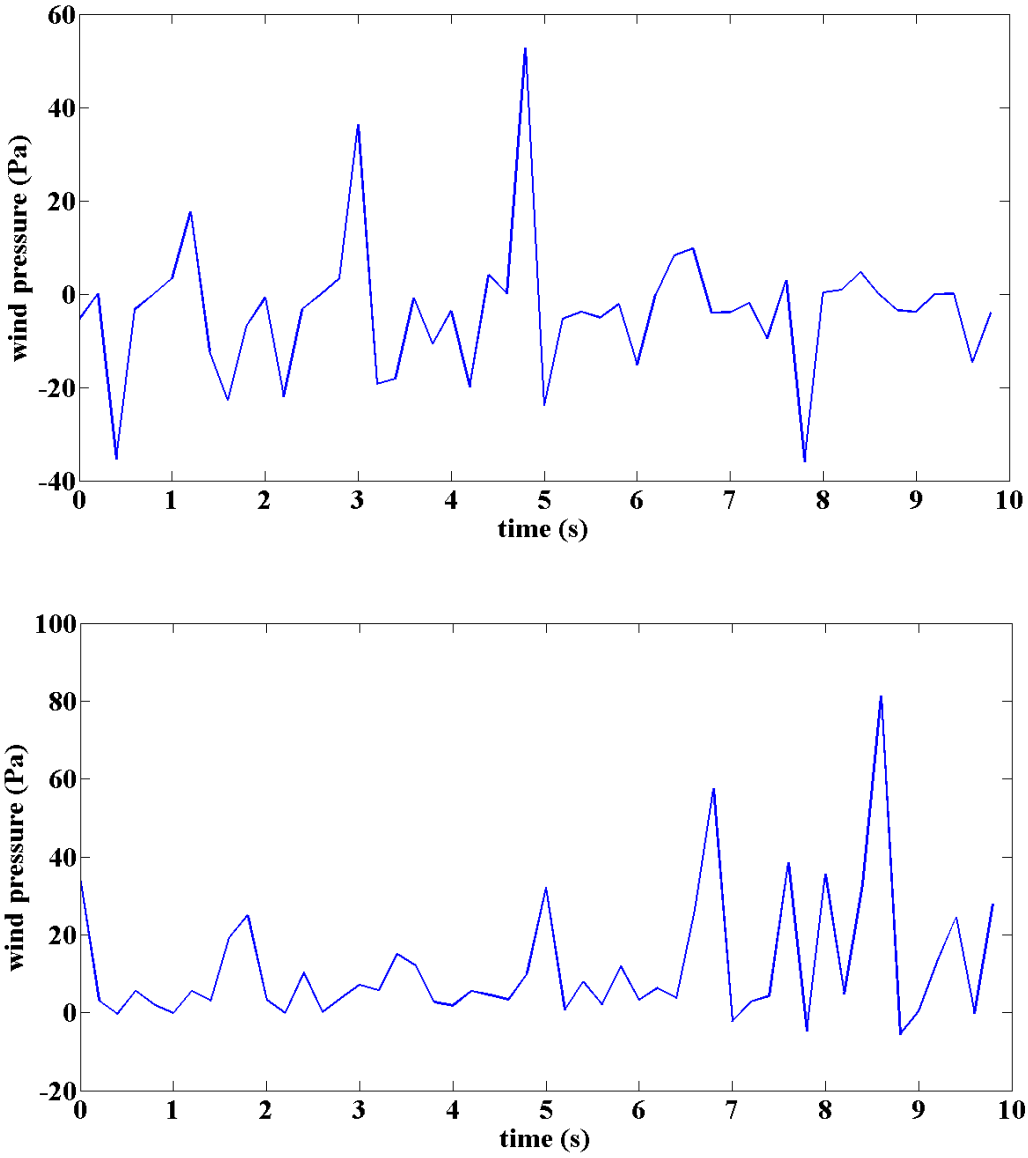

Figure 4.8: Two applied wind pressure sets at 5 Hz (top: set (1), bottom: set (2))

4.3 Evaluation of the LSE-polynomial Algorithm on Asymmetric Laminated Plate Surface

The performance of the LSE-polynomial algorithm is assessed. Results are shown in Figs. 4.9 – 4.12. Note that the BCs were not enforced for the two corner boundary sensor nodes close to the fixed root and the one sensor node close to the free tip considering the bending stress singularity effect at corner (the two free corners of the blade resembling plate are very close to each other geometrically so that the BC at the free side may be significantly disturbed by the corner bending stress singularities).

It can be seen from the time varying MAPE (Fig. 4.9) that the algorithm worked well for the majority of the time during the excitation of the two sets of wind pressure. The MAPE only becomes relatively larger when the wind load is close to zero which is similar to that of the symmetric rectangular plate. This could be explained by the same reason as mentioned in Chapter 2. For most part of the time series, the MAPE of the estimation is relatively constant at the value around 3% for strain x and 12% for strain y. A possible explanation could be that the estimation of strain y is more dependent on the BC assumptions, which contains imperfection for the enforcement on the modeled boundary sensor nodes.

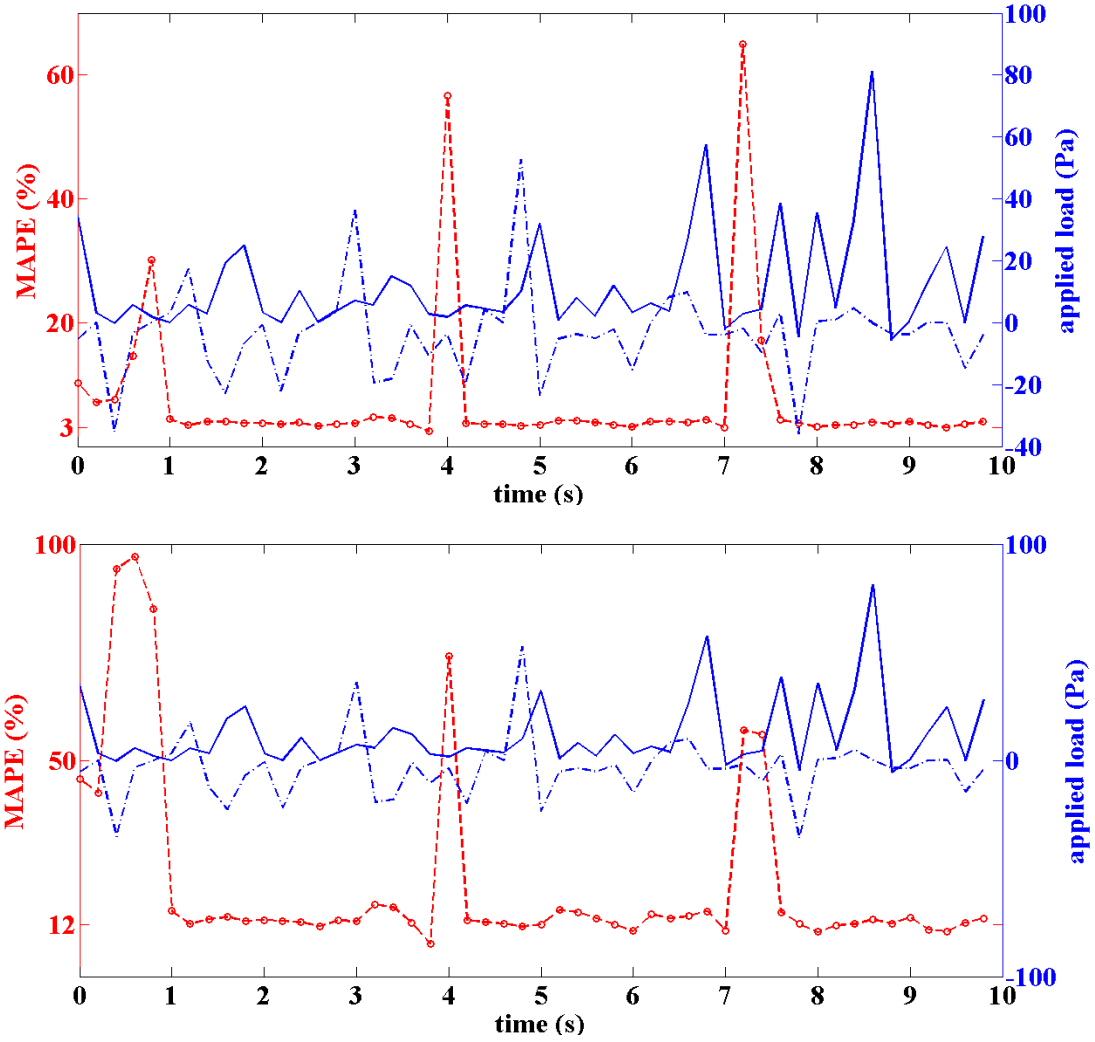

Figure 4.9: MAPE of the estimation for strain x (top) and strain y (bottom) versus time and load

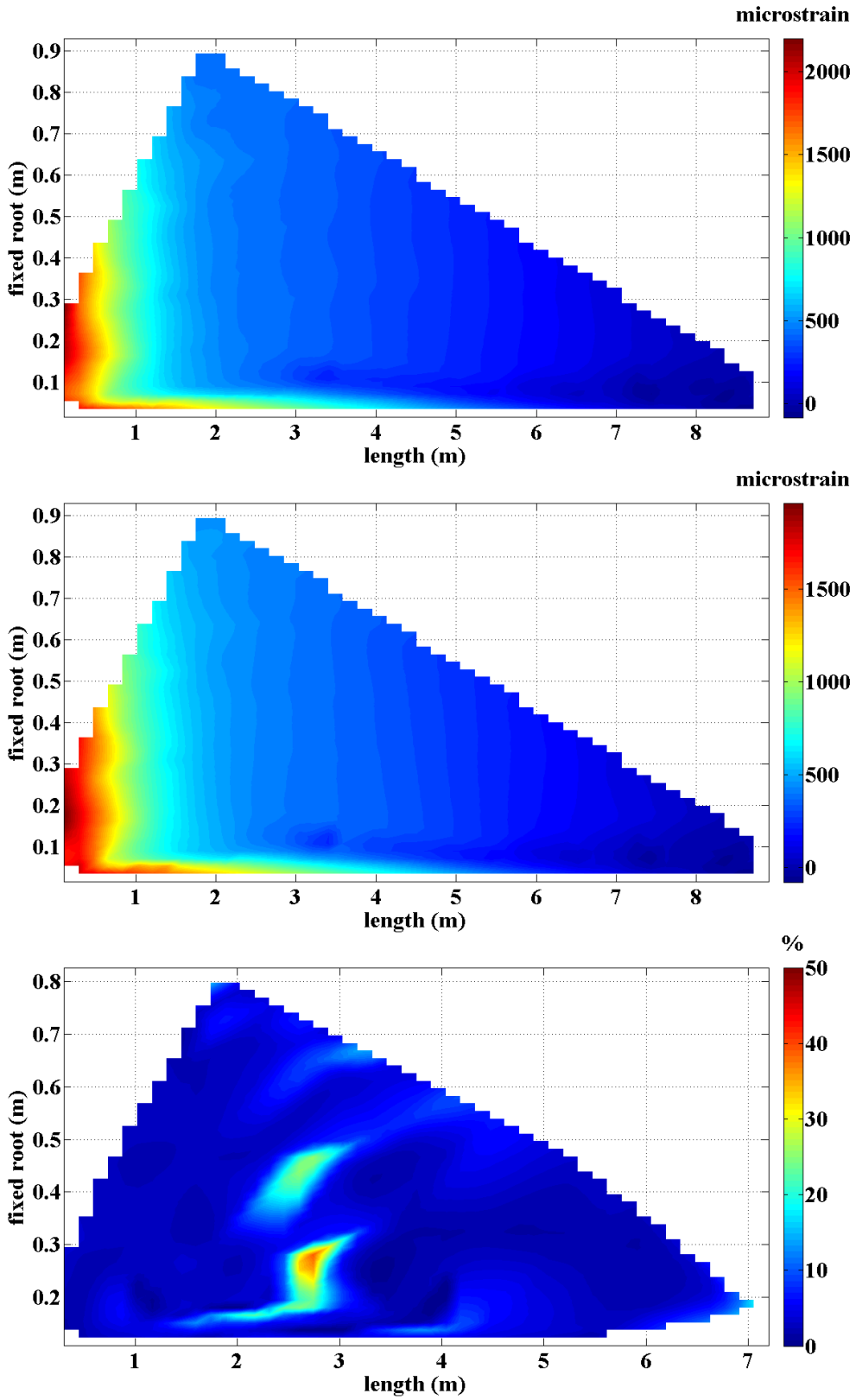

Figure 4.10: Contour plot of Strain x (top: analytical, middle: estimated) and MAPE contour of strain x estimation (bottom) at 5s

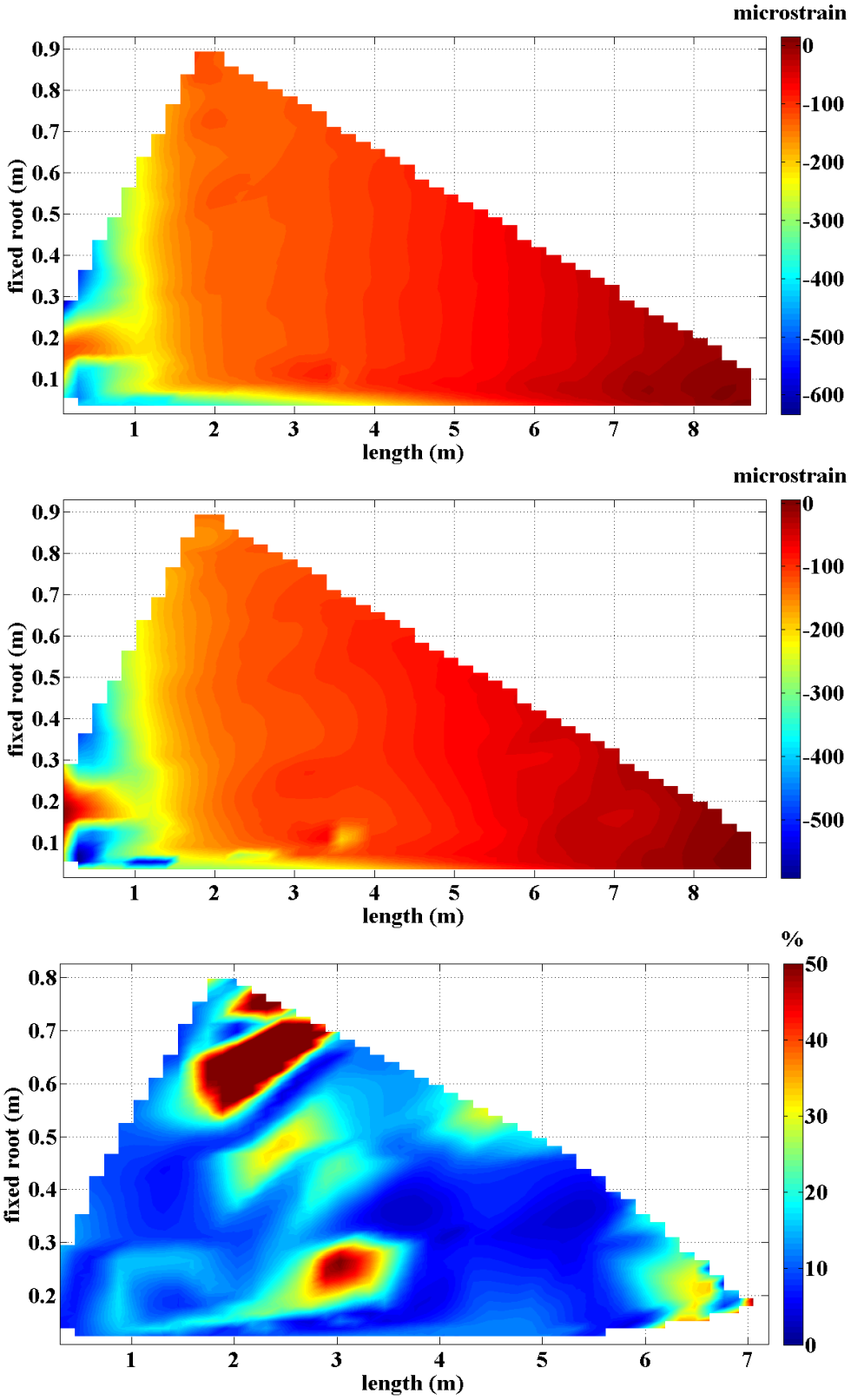

Figure 4.11: Contour plot of strain y (top: analytical, middle: estimated) and MAPE contour of strain y estimation (bottom) at 5s

In addition, the estimation results were compared with the analytical solution for a specific time point. Here, the result at 5 s when the MAPE is relatively constant was selected for the comparison. For the estimation of strain x, Fig. 4.10 shows a good agreement with the analytical solution in the strain contour plot and the MAPE remained under 10% on most of the plate surface. The area with relatively higher value in the MAPE contour is probably due to the imperfection of the BC enforcement of the adjacent boundary sensor nodes. Fig. 4.11 also suggests a good agreement in the strain contour plot between estimated and analytical strain in y direction, though the performance is not as good as that for the strain in x direction, which could also be explained by relatively higher sensitivity of the estimation for strain y to the imperfection of BC enforcement. The MAPE contour of strain y also tend to have higher values at the locations similar to that of strain x which reveals the location of boundary sensor nodes with less accurate BC is close to the top corner. This is probably because of bending stress singularity [31, 32] reducing the accuracy of the BC.

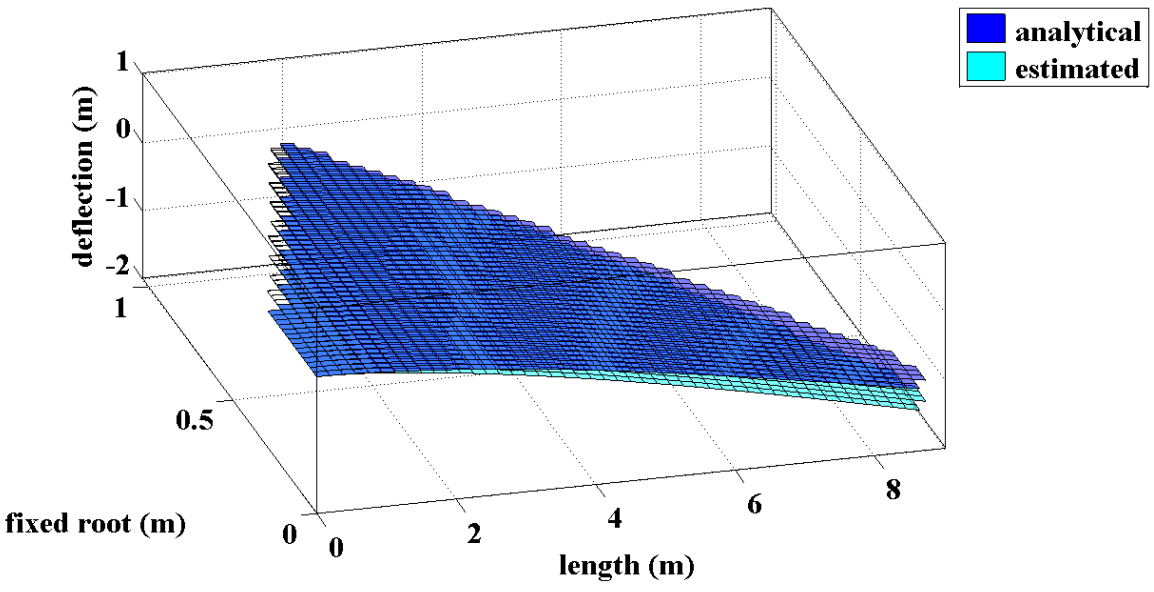

Figure 4.12: Deflection shape estimation at 5s compared with analytical result

After extracting the biaxial strain, the deflection shape can also be reconstructed with the proposed the algorithm. The estimated result compared with the analytical deflection shape is plotted in Fig. 4.12 showing a satisfactory agreement, which manifested the capability of the proposed algorithm to monitor the deformed shape of a thin plate structure.

Overall, the MAPE contour plots reveal that the performance of the proposed algorithm is relatively better on the rectangular plate which can be explained with the following reasons: (1) The irregular geometry of the asymmetric plate determined that only considerably small amount of SEC can be placed at the root (3 SECs) and the free tip (1 SEC), which lead to a loss in BC enforcement; (2) Although the BCs for corners and the free side were not applied in the algorithm for the asymmetric plate due to the concern on bending stress singularities, the accuracy of the rest of the BCs for the modeled boundary sensor nodes that are close to the corners and the free side may also be affected by it; (3) The amount of sensor versus the area of the surface is much smaller for the asymmetric plate compared to the rectangular plate. As a result, the resolution of the sensor mesh for mapping is probably less accurate for the asymmetric plate than the rectangular plate.

CHAPTER 5

CONCLUSION

5.1 Summary

This study is focused on extending the applicability of the SEC from structural surface with uniaxial strain field to that with biaxial strain fields. The limitations of the previous applications of the SEC were discussed and an algorithm was proposed as a potential solution. The algorithm was developed based on least-squares surface fitting technique and the classical plate theory to extract the biaxial strain from the SEC signal for the SEC sensor network installed on the surface of thin plate and shell structures. The potential application of the SEC sensor network for the strain state and deformation monitoring for wind turbine blades was also investigated. Two algorithm formulations (polynomial and biharmonic) were introduced and their capability of biaxial strain decomposition was verified on a symmetric rectangular cantilever thin plate.

Afterwards, the two algorithm formulations were evaluated on the same rectangular plate with two types of accuracy of BC enforcement (ideal and modeled BC enforcement), for various levels of order or expansion of the functions and under different noise levels. By accessing the accuracy, execution time and sensitivity to loss of accuracy of the BC, the polynomial formulation (LSE-polynomial) was shown to perform better than the biharmonic formulation.

At last, an application of the LSE-polynomial algorithm was conducted on a simplified asymmetric laminated cantilever plate resembling a wind turbine blade. To achieve a more realistic loading condition in the simulation, a dual wind pressure time series

was simulated based on real wind speed data sampled with a very low frequency. Although the algorithm performance is not as good as that on the symmetric rectangular cantilever plate due to the loss of accuracy in the BC introduced by the bending stress singularities at the corners with skewed angles, the algorithm still showed satisfactory accuracy on biaxial strain extraction and deflection shape reconstruction.

5.2 Discussion

Based upon the work summarized in this thesis, the following conclusions can be drawn:

1. The proposed algorithm based on least-squares surface fitting technique and the classic plate theory is capable of extracting biaxial strain from the SEC signals of an SEC sensor network and reconstructing deflection shape of thin plate and shell structures with sufficient accuracy.
2. The proposed algorithm with polynomial formulation (LSE-polynomial) performed better than that with biharmonic formulation in terms of higher accuracy, faster computing speed and lower sensitivity to the imperfection of BC enforcement.
3. The accuracy of the estimation of LSE-polynomial algorithm increases when the order of the polynomial formula grows, though the degree of the order is limited by the amount of the SECs in the sensor network.
4. The LSE-polynomial algorithm showed a fast computing speed which enables a real-time SHM.
5. The LSE-polynomial algorithm exhibited a relatively stable performance in estimation accuracy under noise level below 5%.

6. The LSE-polynomial algorithm achieved a satisfactory accuracy on the surface of an irregular laminated thin plate consisted of orthotropic materials which displayed the potential for the application on wind turbine blade, though there is a loss in accuracy compared with the algorithm performance on the rectangular plate due to the bending stress singularities at the corners with skewed angles.
7. The LSE-polynomial algorithm maintained a relatively stable accuracy during the excitation of varies loading condition, including non-stationary wind loads.

5.3 Limitations and Future work

The limitations of the proposed LSE-polynomial algorithm focused on the BC issues:

1. The performance of the algorithm depends considerably on the accuracy of the BC enforcement.
2. Since it is not feasible to install the SEC exactly on the boundaries, the BC cannot be applied on ideal boundary locations, which lowers the algorithm accuracy by bringing inaccurate information to the algorithm through the BC enforcement.
3. The BC can be disturbed by bending stress singularity due to irregular geometry at corners. This also makes the algorithm accuracy depending on the plate geometry.

Accordingly, future work can be conducted on two aspects:

1. The BC enforcement need to be strengthened. Possible solution could be using other matured sensor, such as strain gauges, for the boundary sensor nodes to provide a precise BC.

2. Another possible effort could be finding other mechanical based strain relations that are independent from the plate geometry and introducing that to the algorithm instead of the BC.

REFERENCES

[1] P. C. Chang, A. Flatau, and S. Liu, "Review paper: health monitoring of civil infrastructure," *Structural health monitoring*, vol. 2, pp. 257-267, 2003.

[2] C. R. Farrar and K. Worden, "An introduction to structural health monitoring," *Philosophical Transactions of the Royal Society A: Mathematical, Physical and Engineering Sciences*, vol. 365, pp. 303-315, 2007.

[3] S. Laflamme, M. Kollosche, J. Connor, and G. Kofod, "Soft capacitive sensor for structural health monitoring of large-scale systems," *Structural Control and Health Monitoring*, vol. 19, pp. 70-81, 2012.

[4] E. Udd, "Fiber optic smart structures," *Proceedings of the IEEE*, vol. 84, pp. 884-894, 1996.

[5] R. F. Gibson, "A review of recent research on mechanics of multifunctional composite materials and structures," *Composite structures*, vol. 92, pp. 2793-2810, 2010.

[6] G. Harsányi, "Polymer films in sensor applications: a review of present uses and future possibilities," *Sensor Review*, vol. 20, pp. 98-105, 2000.

[7] W. R. Habel and B. Hillemeier, "Results in monitoring and assessment of damages in large steel and concrete structures by means of fiber optic sensors," in *Smart Structures & Materials' 95*, 1995, pp. 25-36.

[8] W. R. Habel, M. Hoepcke, F. Basedau, and H. Polster, "Influence of concrete and alkaline solutions on different surfaces of optical fibres for sensors," in *Smart Structures and Materials: Second European Conference*, 1994, pp. 168-171.

[9] W. Li, C. Cheng, and Y. Lo, "Investigation of strain transmission of surface-bonded FBGs used as strain sensors," *Sensors and Actuators A: Physical*, vol. 149, pp. 201-207, 2009.

[10] B. Lin, V. Giurgiutiu, Z. Yuan, J. Liu, C. Chen, J. Jiang, *et al.*, "Ferroelectric thin-film active sensors for structural health monitoring," in *The 14th International Symposium on: Smart Structures and Materials & Nondestructive Evaluation and Health Monitoring*, 2007, pp. 65290I-65290I-8.

[11] S. Laflamme, M. Kollosche, J. Connor, and G. Kofod, "Large-scale capacitance sensor for health monitoring of civil structures," *Proc. of 5WCSCM*, 2010.

[12] S. Laflamme, M. Kollosche, V. D. Kollipara, H. S. Saleem, and G. Kofod, "Large-scale surface strain gauge for health monitoring of civil structures," in *SPIE Smart Structures and Materials+ Nondestructive Evaluation and Health Monitoring*, 2012, pp. 83471P-83471P-9.

[13] S. Laflamme, H. Saleem, C. Venkatesh, U. Vaidya, P. Sarkar, and H. Sauder, "Thin film sensor network for condition assessment of wind turbine blades," in *SPIE Smart Structures and Materials+ Nondestructive Evaluation and Health Monitoring*, 2014, pp. 906116-906116-8.

[14] S. Laflamme, H. S. Saleem, B. K. Vasan, R. L. Geiger, D. Chen, M. R. Kessler, *et al.*, "Soft Elastomeric Capacitor Network for Strain Sensing Over Large Surfaces," 2013.

[15] Y. Liu, S. Mohanty, and A. Chattopadhyay, "Condition based structural health monitoring and prognosis of composite structures under uniaxial and biaxial loading," *Journal of Nondestructive Evaluation*, vol. 29, pp. 181-188, 2010.

[16] D. Adams, J. White, M. Rumsey, and C. Farrar, "Structural health monitoring of wind turbines: method and application to a HAWT," *Wind Energy*, vol. 14, pp. 603-623, 2011.

[17] C. C. Ciang, J.-R. Lee, and H.-J. Bang, "Structural health monitoring for a wind turbine system: a review of damage detection methods," *Measurement Science and Technology*, vol. 19, p. 122001, 2008.

[18] P. K. Rastogi, "Photomechanics," Springer2000.

[19] B. Pan, K. Qian, H. Xie, and A. Asundi, "Two-dimensional digital image correlation for in-plane displacement and strain measurement: a review," *Measurement science and technology*, vol. 20, p. 062001, 2009.

[20] H. Goldrein, S. Palmer, and J. Huntley, "Automated fine grid technique for measurement of large-strain deformation maps," *Optics and Lasers in Engineering*, vol. 23, pp. 305-318, 1995.

[21] J. Sirkis and T. Lim, "Displacement and strain measurement with automated grid methods," *Experimental Mechanics*, vol. 31, pp. 382-388, 1991.

[22] A. Tessler and J. L. Spangler, *A variational principle for reconstruction of elastic deformations in shear deformable plates and shells*: National Aeronautics and Space Administration, Langley Research Center, 2003.

[23] A. Tessler and J. L. Spangler, "Inverse FEM for full-field reconstruction of elastic deformations in shear deformable plates and shells," in *Proceedings of Second European Workshop on Structural Health Monitoring*, 2004, pp. 83-90.

[24] A. Tessler and J. L. Spangler, "A least-squares variational method for full-field reconstruction of elastic deformations in shear-deformable plates and shells," *Computer methods in applied mechanics and engineering*, vol. 194, pp. 327-339, 2005.

[25] P. Lancaster and K. Salkauskas, "Curve and surface fitting. An introduction," *London: Academic Press, 1986*, vol. 1, 1986.

[26] R. Jones, D. Bellemore, T. Berkoff, J. Sirkis, M. Davis, M. Putnam, *et al.*, "Determination of cantilever plate shapes using wavelength division multiplexed fiber Bragg grating sensors and a least-squares strain-fitting algorithm," *Smart materials and structures,* vol. 7, p. 178, 1998.

[27] B. K. Bay, T. S. Smith, D. P. Fyhrie, and M. Saad, "Digital volume correlation: three-dimensional strain mapping using X-ray tomography," *Experimental Mechanics,* vol. 39, pp. 217-226, 1999.

[28] C. Rajalingham, R. Bhat, and G. Xistris, "Vibration of rectangular plates using plate characteristic functions as shape functions in the Rayleigh–Ritz method," *Journal of sound and vibration,* vol. 193, pp. 497-509, 1996.

[29] B. Tian, Y. Zhong, and R. Li, "Analytic bending solutions of rectangular cantilever thin plates," *Archives of Civil and Mechanical Engineering,* vol. 11, pp. 1043-1052, 2011.

[30] Y. Zhong, X.-F. Zhao, and R. Li, "Free vibration analysis of rectangular cantilever plates by finite integral transform method," *International Journal for Computational Methods in Engineering Science and Mechanics,* vol. 14, pp. 221-226, 2013.

[31] C. Huang, "Stress singularities at angular corners in first-order shear deformation plate theory," *International journal of mechanical sciences,* vol. 45, pp. 1-20, 2003.

[32] O. McGee, A. Leissa, and C. Huang, "Vibrations of cantilevered skewed trapezoidal and triangular plates with corner stress singularities," *International journal of mechanical sciences,* vol. 34, pp. 63-84, 1992.

[33] S. Laflamme, M. Kollosche, J. J. Connor, and G. Kofod, "Robust flexible capacitive surface sensor for structural health monitoring applications," *Journal of Engineering Mechanics,* vol. 139, pp. 879-885, 2012.

[34] D. Berry and T. Ashwill, "Design of 9-meter carbon-fiberglass prototype blades: CX-100 and TX-100," *SAND2007-0201, Sandia National Laboratories, Albuquerque, NM,* 2007.

[35] S. Rose and J. Apt, "Generating wind time series as a hybrid of measured and simulated data," *Wind Energy,* vol. 15, pp. 699-715, 2012.

[36] N. W. Service, "Physical Oceanographic Real-Time System (9414290 San Francisco, CA)," N. O. a. A. Administration, Ed., ed. Center for Operational Oceanographic Products and Services, 2014.

[37] W. H. Press, *Numerical recipes 3rd edition: The art of scientific computing*: Cambridge university press, 2007.

[38] J. Kaimal, J. Wyngaard, Y. Izumi, and O. Coté, "Spectral characteristics of surface-layer turbulence," *Quarterly Journal of the Royal Meteorological Society,* vol. 98, pp. 563-589, 1972.

[39] I. E. Commission, "IEC 61400-1," in *Wind turbines - part 1: design requirements* vol. 3rd ed., ed: International Electroctechnical Commission: Geneva, 2005.

[40] M. Shinozuka and C.-M. Jan, "Digital simulation of random processes and its applications," *Journal of sound and vibration*, vol. 25, pp. 111-128, 1972.

[41] P. S. Veers, *Modeling stochastic wind loads on vertical axis wind turbines*: Sandia National Laboratories, 1984.